Magnetic Properties of $3d$ and $4f$ Ferromagnets Studied by X-Ray Absorption Spectroscopy

im Fachbereich Physik
der Freien Universität Berlin
eingereichte Dissertation

von
Claudia Sorg

Oktober 2005

Sorg, Claudia:
Magnetic Properties of 3*d* and 4*f* Ferromagnets Studied by X-Ray Absorption Spectroscopy / Claudia Sorg. –
Als Ms. gedr.. – Berlin : dissertation.de – Verlag im Internet GmbH, 2006
Zugl.: Berlin, Freie Univ., Diss., 2005
ISBN 3-86624-097-X

Gutachter: 1. Prof. Dr. Klaus Baberschke
2. Prof. William Brewer, PhD

Tag der Einreichung: 14.10.2005
Tag der Disputation: 23.11.2005

Bibliografische Information der Deutschen Bibliothek

Die Deutsche Bibliothek verzeichnet diese Publikation in der Deutschen Nationalbibliografie; detaillierte bibliografische Daten sind im Internet über <http://dnb.ddb.de> abrufbar.

dissertation.de – Verlag im Internet GmbH 2006

Es wird ausschließlich chlorfrei gebleichtes
Papier (TCF) nach DIN-ISO 9706 verwendet.
Printed in Germany.

dissertation.de - Verlag im Internet GmbH
Pestalozzistraße 9
10625 Berlin

URL: http://www.dissertation.de

Abstract

In this thesis, the magnetism of ultrathin ferromagnetic films of Fe, Co, and Ni as well as the magnetism of single crystals of the rare earth elements Gd, Tb, and Dy have been studied by means of X-ray absorption spectroscopy. To support measurements even in an applied magnetic field, a new water-cooled coil system has been developed and installed in the UHV chamber.

The electronic structure of ultrathin ferromagnetic films of Fe, Co, and Ni has been investigated by near edge X-ray absorption fine structure (NEXAFS) spectra. Oxygen as surfactant has been used to tailor the structural properties of these ultrathin films. The obtained X-ray magnetic circular dichroism (XMCD) spectra at the O K edge show that the surfactant O acquires an induced orbital moment parallel to the spin and orbital moment of the ferromagnetic film. *Ab initio* calculations reproduce the experimental spectra and yield the size of spin and orbital moments. Thickness-dependent XMCD investigations at the $L_{2,3}$ edges have been carried out in the case of Ni grown with O as surfactant. These experiments show that the total magnetization of the thinnest Ni films is reduced on the Cu(100) surface compared to the bulk value. On the more open Cu(110) surface the magnetization is enhanced, mainly due to the orbital moment.

Two-dimensional spin fluctuations and the interlayer exchange coupling (IEC) have been studied on Co/Cu/Ni/Cu(100) trilayers. Using XMCD, the influence of the IEC on the element-specific Ni magnetization has been investigated as a function of temperature. The quasi-critical temperature $T^*_{\mathrm{C,Ni}}$ of Ni in the trilayer is increased by $\Delta T_{\mathrm{C,Ni}}$ compared to the Curie temperature $T_{\mathrm{C,Ni}}$ of the single Ni film. The experiments together with calculations show the shift $\Delta T_{\mathrm{C,Ni}}$ as a function of both the Ni thickness d_{Ni} and the Cu thickness d_{Cu}. A three-dimensional plot of the full dependence $\Delta T_{\mathrm{C,Ni}}/T_{\mathrm{C,Ni}}\,(d_{\mathrm{Ni}},\, d_{\mathrm{Cu}})$ results. Therefore, a relation between $\Delta T_{\mathrm{C,Ni}}/T_{\mathrm{C,Ni}}$ and the coupling strength J_{inter} has been derived with the help of a theoretical model including spin fluctuations. Calculations of $\Delta T_{\mathrm{C,Ni}}/T_{\mathrm{C,Ni}}\,(d_{\mathrm{Ni}},\, d_{\mathrm{Cu}})$ match the experimental findings.

Temperature-dependent XMCD spectra at the $L_{2,3}$ edges of the rare earth elements Gd, Tb, and Dy have been measured. In this work high purity single crystals have been used which do not include additional complex interactions as they occur in compounds. The obtained XMCD spectra contain contributions of dipole transitions (E1: $2p \rightarrow 5d$) and quadrupolar transitions (E2: $2p \rightarrow 4f$). Therefore, it is possible to investigate the magnetism of $5d$ and $4f$ states in a single experiment. In this thesis, it is demonstrated that the contributions of $5d$ and $4f$ to the total magnetization can be separated by calculating the spectra for $T = 0$ using the FEFF code. Furthermore, the experiments have revealed that the relative intensities of the different spectroscopic features of the XMCD change as a function of the temperature.

Kurzfassung

In dieser Arbeit wurde sowohl der Magnetismus ultradünner, ferromagnetischer Fe-, Co- und Ni-Filme als auch der Magnetismus von Einkristallen der Seltenen Erden Gd, Tb und Dy mittels Röntgenabsorptionsspektroskopie untersucht. Im Rahmen dessen wurde für die vorhandene UHV-Apparatur ein neues, wassergekühltes Spulensystem entwickelt, um Messungen auch im angelegten Magnetfeld zu ermöglichen.

Die elektronische Struktur der ultradünnen, ferromagnetischen Fe-, Co- und Ni-Filme wurde mit Röntgenabsorptionsspektren im Nahkantenbereich (NEXAFS) untersucht. Dabei wurde Sauerstoff als Surfactant eingesetzt, um die strukturellen Eigenschaften der Filme zu verbessern. Die mittels magnetischem Röntgenzirkulardichroismus (XMCD) gemessenen Spektren an der Sauerstoff-K-Kante zeigen, dass im Sauerstoff-Surfactant ein orbitales Moment parallel zu Spin- und Bahnmoment des jeweiligen ferromagnetischen Films induziert wird. Die Größen der Spin- und Bahnmomente ergeben sich aus *ab-initio*-Rechnungen, die die experimentellen Spektren sehr gut reproduzieren. Dickenabhängige XMCD-Untersuchungen an den $L_{2,3}$-Kanten wurden an Ni-Filmen durchgeführt, die mit O-Surfactant gewachsen wurden. Diese Experimente zeigen, dass die Gesamtmagnetisierung des dünnsten Ni-Films auf der Cu(100)-Oberfläche gegenüber der Magnetisierung von Ni im Volumen reduziert ist. Auf der offeneren Cu(110)-Oberfläche ist die Gesamtmagnetisierung des dünnsten Ni-Films erhöht. Aus der Analyse ergibt sich, dass das Bahnmoment einen erheblichen Anteil dieser Erhöhung trägt.

Zweidimensionale Spin-Fluktuationen und die Interlagenaustauschkopplung J_{inter} wurden an Co/Cu/Ni/Cu(100)-Dreifachlagen untersucht. Mit der XMCD-Methode wurde der Einfluss von J_{inter} auf die elementspezifische Ni-Magnetisierung temperaturabhängig bestimmt. Die quasi-kritische Temperatur $T^*_{\text{C,Ni}}$ des Ni in der Dreifachlage ist um $\Delta T_{\text{C,Ni}}$ höher als die Curie-Temperatur $T_{\text{C,Ni}}$ des einfachen Ni-Films. Die Experimente in Kombination mit Theorie zeigen die Verschiebung $\Delta T_{\text{C,Ni}}$ als Funktion der beiden Schichtdicken d_{Ni} und d_{Cu} der Ni- bzw. Cu-Schicht. Es ergibt sich ein dreidimensionaler Graph, der die vollständige Abhängigkeit $\Delta T_{\text{C,Ni}}/T_{\text{C,Ni}}\,(d_{\text{Ni}},\ d_{\text{Cu}})$ darstellt. Die dafür notwendige Beziehung zwischen $\Delta T_{\text{C,Ni}}/T_{\text{C,Ni}}$ und J_{inter} konnte im Rahmen eines theoretischen Modells bestimmt werden, das die erhöhten Spin-Fluktuationen in zweidimensionalen Systemen berücksichtigt. Rechnungen der Temperaturverschiebung $\Delta T_{\mathrm{C,Ni}}/T_{\mathrm{C,Ni}}\,(d_{\mathrm{Ni}},\ d_{\mathrm{Cu}})$ in diesem Modell stimmen mit den experimentellen Beobachtungen überein.

XMCD-Spektren an den $L_{2,3}$-Kanten der Seltenen Erden Gd, Tb und Dy wurden temperaturabhängig gemessen. In dieser Arbeit wurden für diese Messungen einelementare Einkristalle verwendet, die keine zusätzlichen Wechselwirkungen beinhalten, wie sie in komplexen Verbindungen auftreten. Die gemessenen XMCD-Spektren enthalten Beiträge sowohl von Dipol-Übergängen (E1: $2p \to 5d$) als auch von Quadrupol-Übergängen (E2: $2p \to 4f$). Deshalb kann der Magnetismus der $5d$- und der $4f$-Zustände im selben Experiment untersucht werden, die jedoch in der Analyse voneinander getrennt werden müssen. In dieser Arbeit wird gezeigt, dass durch die Berechnung der Spektren bei $T = 0$ mit Hilfe des FEFF-Codes die Trennung der magnetischen Beiträge der $5d$- und $4f$-Zustände möglich ist. Darüber hinaus haben die Experimente ergeben, dass sich die Linienform der XMCD-Spektren in Abhängigkeit von der Temperatur ändert.

Contents

Chapter 1

Introduction

Magnetic nanostructures are the heart of modern storage media. Miniaturization of devices leads to further reduction of structural dimensions. Systems which are dominated by interfaces rather than volume show new magnetic properties. However, many questions about the fundamental mechanisms leading to these properties remain unsolved. It is crucial to identify the contribution of each element contained in such materials and to determine the spin and orbital moments. This is possible with methods based on X-ray absorption spectroscopy (XAS). Furthermore, XAS can distinguish transitions of different character to excited states, e.g. dipolar and quadrupolar transitions, while many other well-established techniques, e.g. vibrating sample magnetometry (VSM), ferromagnetic resonance (FMR), magneto-optical Kerr effect (MOKE), and superconducting quantum interference device (SQUID) magnetometry determine an average of all magnetic contributions. X-ray absorption spectra provide element-specific and shell-selective information about the samples. Electronic properties may be investigated by near edge X-ray absorption fine structure (NEXAFS) spectra [1]. Magnetic properties are obtained from spin-dependent X-ray absorption spectra exploiting the X-ray magnetic circular dichroism (XMCD) [2, 3].

In this thesis, three main questions of magnetic nanostructures are addressed. (i) How does oxygen as a surfactant influence the electronic and magnetic properties of ultrathin ferromagnetic films? (ii) What happens in trilayer systems at the transition to two-dimensional layers where spin fluctuations become important? (iii) Can the $4f$ and $5d$ magnetism of rare earth elements systematically be separated and calculated quantitatively, also as a function of the temperature?

In the first part of the thesis, the influence of oxygen as a surfactant on the electronic and magnetic properties of Fe, Co, and Ni films on Cu single crystals is studied. The surfactant is adsorbed onto the clean substrate surfaces before the ferromagnetic

(FM) film is grown. If a material acts as a surfactant, it will "float" on the surface of the growing film, thereby reducing the surface free energy and improving the layer-by-layer growth [4–6]. By NEXAFS at the O K edge and the $L_{2,3}$ edges of the FMs, the electronic structure is elucidated. Do the ferromagnets form an oxide when grown with oxygen as surfactant? How does the electronic structure of the surfactant grown film compare to the one of the clean films? Does, for example, a charge transfer between O and $3d$ FM states occur? Concerning the magnetism, the relevant questions to be answered in this thesis are: Is there a difference in the magnetization of the surfactant grown films and the clean ones? Is this difference, if it occurs, mainly caused by the spin or the orbital contribution? Does the FM film induce a magnetic moment in the oxygen? If so, how large are the spin and the orbital moments?

The second topic concerns ultrathin films of Ni and Co combined in Co/Cu/Ni trilayers on a Cu(100) substrate. These trilayers serve as a prototype system to study the effect of the interlayer exchange coupling (IEC) which couples the two FM layers across the nonmagnetic (NM) Cu spacer [7–11]. The influence of the IEC on the FM layers is especially interesting in the two-dimensional (2D) limit of the FM film thickness with enhanced spin fluctuations. 2D effects do not only become important when miniaturizing technological devices down to the physical limits, but they are also interesting from a fundamental point of view. In this part of the study, special advantage is taken from the *in situ* preparation and measurement of the samples. First, the magnetization of a Cu-capped Ni film is investigated. Then, the IEC is "switched on" by depositing the Co film on top of the identical Cu/Ni/Cu(100) sample. This ensures that any change in the element-specific Ni magnetization may be addressed to the influence of the IEC. Indeed, in the trilayer the quasi-critical temperature of the Ni layer $T^{*}_{\mathrm{C,Ni}}$ is shifted by $\Delta T_{\mathrm{C,Ni}}$ to higher T compared to the Curie temperature $T_{\mathrm{C,Ni}}$ of the single Ni film [12, 13]. In the past, two effects in these trilayers have been studied and discussed separately: (i) the shift $\Delta T_{\mathrm{C,Ni}}/T_{\mathrm{C,Ni}}$ as a function of the Ni thickness d_{Ni} [14] and (ii) the coupling strength J_{inter} as a function of the spacer thickness d_{Cu} [7, 15]. However, one interesting question has not been answered yet: What will happen if both effects are considered simultaneously? Especially, when reducing both d_{Cu} *and* d_{Ni}, the two effects will compete in determining the magnetization of the Ni layer. What is the resulting Ni magnetization in this ultrathin limit? This means that experimental investigations in this thin thickness range as well as a relation between the coupling strength J_{inter} and the temperature shift $\Delta T_{\mathrm{C,Ni}}/T_{\mathrm{C,Ni}}$ are needed.

In the third part of this thesis, the focus is turned to XMCD studies of the rare earth elements Gd, Tb, and Dy. They are a good example of materials in which the magnetic moments of different shells and their interactions play an important role. The largest part of the magnetization is carried by the highly localized $4f$ moments. The ferromagnetic order among the $4f$ states is mediated by the delocalized $5d$ conduction electrons which carry an induced magnetic moment. Since XMCD is shell-selective it is in principle suitable to study the $5d$ magnetism separately from one of the $4f$ states. Unfortunately, complications occur because XMCD spectra at the $L_{2,3}$ edges of the rare earth elements contain contributions of dipolar (E1: $2p \rightarrow 5d$) and of quadrupolar (E2: $2p \rightarrow 4f$) transitions which partly overlap [16–18]. The goal of the present study is beyond the simple prove of existence of E2 transitions at the $L_{2,3}$ edges of rare earth elements. The questions are: How can the dipolar contributions be separated from the quadrupolar ones in measured spectra? To what extend is the calculation of E1 and E2 contributions possible? Single crystals of the single elements Gd, Tb, and Dy are used to investigate the systematics of the rare earth XMCD at the $L_{2,3}$ edges. Such single crystals do not include additional complex interactions of the different species contained in compounds as they were used to obtain most of the existing XMCD data of rare earth elements in literature.

The thesis is organized as follows: The next chapter introduces the basic principles of X-ray absorption spectroscopy and X-ray magnetic circular dichroism. The standard normalization procedure and analysis are presented there. In Chapter 3 details about the experimental setup inside the UHV chamber, the sample preparation, and the beamlines used at BESSY and the ESRF are given. Furthermore, it includes details about a new water-cooled coil system that has been designed and set into operation. Three chapters with the results follow. Chapter 4 explains the investigations of ultrathin films of Fe, Co, and Ni grown with O surfactant. Chapter 5 discusses the Co/Cu/Ni trilayers and the two-dimensional spin fluctuations. Chapter 6 presents the systematics of the temperature-dependent XMCD of Gd, Tb, and Dy. Finally, Chapter 7 summarizes the results of this work. The appendix contains a note on the use of units in this thesis and some additional information on the coil system that goes beyond the scope of Chapter 3.

Chapter 2

Ferromagnetism and X-Ray Absorption Spectroscopy

X-ray magnetic circular dichroism (XMCD) is a magneto-optical effect. Magneto-optical effects occur due to the influence of the magnetic properties of a system on its spectroscopic and optical properties, for a review see Ref. [19]. In the regime of visible light magneto-optical effects are known since Faraday and Kerr. They discovered that the polarization vector of light rotates upon transmission through or reflection at magnetic matter. The magneto-optical Kerr effect (MOKE) is nowadays commonly exploited in conventional magnetization measurements with linearly polarized laser light. The basic principle of MOKE is the different absorption of left and right circularly polarized light. Considering that a linear polarization state may be described by a linear combination of the two circular polarization states, the initially linearly polarized beam is elliptically polarized after reflection at the surface of the magnetic sample. The Kerr ellipticity is a direct measure of the magnetization of the sample. With low energy photons of a few electron volts the optical transitions of solids are always within the valence band. The information obtained is influenced by both initial and final state densities. Various groups tried to find similar magneto-optical effects in the X-ray regime since the beginning of the last century. However, experimental success suffered from the lack of an appropriate X-ray source. Erskine and Stern predicted by their calculations in 1975 that a magneto-optical effect in X-ray absorption of circularly polarized light, i.e. XMCD, at the $M_{2,3}$ edges of ferromagnetic Ni should exist [20]. With the availability of synchrotron radiation sources providing X-rays with tunable energy and polarization, the group of Schütz finally evidenced XMCD in an experiment at the K edge of a Fe foil in 1987 [21]. In the X-ray regime a well-defined core level may be chosen for the initial state – in contrast to the ones of experiments in the visible regime. The initial state is highly localized and described by the quantum numbers of the core level. The transitions occur into the valence band or the continuum whose density of states is scanned by the energy of the incoming photons. According to the selection rules, the possible types of final states are determined by the chosen initial state. Thus, methods based on X-ray absorption like XMCD provide shell-selective information. Moreover, they are also element-selective because the energy of the core levels is characteristic for the different elements. Therefore, XMCD has proven very useful for the understanding of complex magnetic structures where the contribution of each constituent can be probed individually.

2.1 Interaction of X-Rays with Matter

X-Ray Absorption

When electromagnetic radiation with photon energy E meets matter, its intensity I as a function of the penetration depth d is reduced due to the interaction between the photons and the material. The attenuation of the initial intensity $I_0(E,d)$ follows the Beer-Lambert law

$$I \;=\; I_0\,\mathrm{e}^{-\widetilde{\mu}(E)d}\,. \tag{2.1}$$

If the absorption is the dominant process compared to other processes like Compton scattering and inelastic scattering the absorption coefficient $\mu(E)$ will be in good approximation equal to the attenuation coefficient $\widetilde{\mu}(E)$. In the energy range of up to some tens of kilo-electron-volts, in which the experiments of the present work were carried out, this may be considered true [1]. The absorption coefficient is related to the absorption cross section $\sigma(E) = \mu(E)/n$ via the density of atoms n.

When a photon in the X-ray regime with energy $E = \hbar\omega$ is absorbed, an electron in a core shell of energy E_i is excited from its initial state $|i\rangle$ to a final state $|f\rangle$ with energy $E_f = E_i + E$ and density of the final states $\rho\,(E_f)$. The absorption cross section is given by the transition probability $\Gamma_{i\to f}$ and the photon flux I_{ph},

$$\sigma(E) \;=\; \frac{\Gamma_{i\to f}}{I_{ph}}\,. \tag{2.2}$$

Fermi's Golden Rule describes the transition probability per unit of time

$$\Gamma_{i\to f} \;=\; \frac{2\pi}{\hbar}\,|\langle f|\mathcal{H}_{int}|i\rangle|^2\,\rho\,(E_f)\;\;, \tag{2.3}$$

where $\mathcal{H}_{int}$ is the interaction operator reflecting a time-dependent perturbation of the Hamiltonian $\mathcal{H}_0$ of the atom. The Hamiltonian of an electron with charge e and mass m in an electromagnetic field described by the vector potential $\vec{A}\,(\vec{r},t)$ and the scalar potential $\varphi\,(\vec{r},t)$ is

$$\begin{aligned}\mathcal{H} \;=\; \mathcal{H}_0 + \mathcal{H}_{int} \;&=\; \frac{1}{2m}\left(\frac{\hbar}{i}\nabla - \frac{e}{c}\vec{A}\,(\vec{r},t)\right)^2 + \varphi\,(\vec{r},t) \\ &=\; \mathcal{H}_0 - \frac{e}{2mc}\vec{A}\,(\vec{r},t)\cdot\frac{\hbar}{i}\nabla + \frac{e^2}{2mc^2}\vec{A}\,(\vec{r},t)^2 \qquad (2.4)\end{aligned}$$

within the Coulomb gauge ($\nabla \cdot \vec{A} = 0$). Expressing the vector potential of the incoming photons by plane waves with amplitude A_0, wave vector $\vec{k}$, frequency ω and polarization vector $\vec{\varepsilon}$ the interaction operator becomes

$$\mathcal{H}_{int} = -\frac{e\hbar}{i2mc}A_0\,\vec{\varepsilon}\,\mathrm{e}^{i(\vec{k}\vec{r}-\omega t)}\cdot\nabla\ , \qquad (2.5)$$

where the last term of Eq. (2.4), which reflects two photon annihilation/excitation processes, is neglected. Expanding the exponential factor of Eq. (2.5) one obtains

$$A_0\,\varepsilon\,\mathrm{e}^{i(\vec{k}\vec{r}-\omega t)} = A_0\,\varepsilon\,\mathrm{e}^{-i\omega t}\left(1 - i\vec{k}\vec{r} + \frac{1}{2}(i\vec{k}\vec{r})^2 + \ldots\right)\ . \qquad (2.6)$$

In the dipole approximation the expansion is truncated after the first term. This corresponds to the electric dipole (E1) transitions. Considering further terms $\left(\vec{k}\vec{r}\right)^n$ means to include the electric 2^{n+1}-pole (E$n+1$) and magnetic 2^n-pole (Mn) transitions [22].

Characteristic jumps in the absorption spectra result from the consecutive excitation of the core levels. They occur at photon energies that correspond to the energy difference of the according level to the Fermi level. These edges will be labeled K, L_1, L_2, L_3, M_1, …, if the inital state is $|2s\rangle$, $|2p_{1/2}\rangle$, $|2p_{3/2}\rangle$, $|3s_{1/2}\rangle$, …, respectively.

In principle, the absorption coefficient will be characterized by the transition matrix element, if appropriate descriptions of the initial and final states exist. Due to their localization the initial core states have an atomic character with well defined quantum numbers. The description of the final states is in general more difficult. The excitation of an electron in an atom affects the other electrons which may interact among each other and with the created core hole [23, 24]. Weakly correlated systems may be treated within the independent particle model neglecting screening effects and the core hole. Then the final states are given by the ground state of the system.

The possible types of final states are determined by the atomic-like initial states of quantum numbers j, m, ℓ, and s according to the selection rules

(i) for electric dipole (E1) transitions

$$\Delta j = 0,\ \pm 1;\ \ \Delta s = 0;\ \ \Delta \ell = \pm 1;\ \ \Delta m = \begin{cases} +1 & \text{left circular} \\ 0 & \text{linear} \\ -1 & \text{right circular} \end{cases} \tag{2.7}$$

(ii) for electric quadrupole (E2) transitions

$$\Delta j = 0,\ \pm 1,\ \pm 2;\ \ \Delta s = 0;\ \ \Delta \ell = 0,\ \pm 2;\ \ \Delta m = 0,\ \pm 1,\ \pm 2; \tag{2.8}$$

However, if $\ell\left(|i\rangle\right) = 0$, then $\ell\left(|f\rangle\right) = 0$ is not allowed for E2 transitions.

Detection Methods

There are various possibilities to measure the X-ray absorption coefficient. Depending on the measuring conditions and especially the samples themselves one method may be more appropriate than the others [1]. A direct measurement of the absorption cross section is through the detection of the photon flux before and after the sample. Such kinds of transmission experiments are probably the most reliable [25], but they are rarely possible especially in the soft X-ray regime due to the strong absorption. Hardly any sample is transparent to a sufficient extent in the X-ray regime. However, some examples exist where the transmission has directly been determined, e.g. at the $L_{2,3}$ edges of thin Fe and Co films of $50 - 70$ Å on a 1μm thick semi-transparent parylene substrate [25]. A major advantage of such transmission experiments is that they are not sensitive to the surface only, but probe the entire sample. In most of the experiments secondary effects are exploited to determine the absorption coefficient. The excited states decay via X-ray fluorescence and the Auger effect. In both cases, the probability of emission (X-ray or electron) will be directly proportional to the absorption probability under certain conditions. Thus, detecting the fluorescence photons or the Auger electrons yields the absorption coefficient.

In a quantitative analysis of the total electron yield (TEY) it has been shown that the TEY will be proportional to the absorption coefficient, if the absorption length of the incoming photons is much larger than the average escape depth of the photoelectrons [26]. This proportionality has been tested and confirmed in various examples, e.g. [27, 28]. When measuring at grazing incidence, saturation effects have to be taken into account in the analysis of the spectra [27, 29, 30]. The probing depth of secondary electrons is around 20 Å [31], which makes the detection via TEY surface sensitive. One possibility to record TEY is by using a channeltron electron multiplier close to the sample. The drawback of this method is that channeltrons suffer from static magnetic fields. Therefore, they are only suitable for investigations in remanence. Another possibility is to record the sample drain current with the help of an electrometer in the range of picoampere. This method is chosen in the experimental setup for measurements at BESSY (Berliner Elektronenspeicherring-Gesellschaft für Synchrotronstrahlung m. b. H.), as described in Chapter 3. In this situation the sample must be highly electrically insulated which requests low level DC measurements. For measurements in applied magnetic fields the proper escape of the secondary electrons may be guaranteed by an extraction grid close to the sample [2]. Thus, it is possible to measure element-specific hysteresis loops by TEY detection [28, 32].

Besides TEY detection, fluorescence yield (FY) detection is another method of choice for the investigation of nontransparent samples. FY detection is used, for example, for absorption measurements at the ID12 beamline at the ESRF (European Synchrotron Radiation Facility, see Sec. 3.4). In comparison to Auger electrons, fluorescence photons are not sensitive to an external magnetic field when they escape from a sample. Furthermore, fluorescence detection has the advantage that it is also applicable to insulating materials [1]. Due to the larger escape depth of the fluorescence photons, in general, the probing depth is much larger than in TEY. Thus, by FY bulk properties of the sample may be investigated. If dilute samples or thin films are investigated, the FY signal will be directly proportional to the absorption coefficient. For concentrated bulk samples the FY signal can exhibit a strong nonlinearity [33, 34]. These self-absorption effects result from the attenuation of the penetrating and escaping X-ray radiation while propagating through the sample. It has been shown that these self-absorption effects in FY can fully be corrected [33]. FY decreases with decreasing atomic number and Auger transitions are the dominant decay channel [2]. Therefore, TEY detection is, in general, applied more commonly for absorption measurements of the lighter elements in the soft X-ray regime whereas FY is used for elements with larger atomic number in the hard X-ray regime.

2.2 Information in X-Ray Absorption Spectra

X-ray absorption spectra are typically divided into two regions. In their near edge region up to approximately 50 eV above the edge the near edge X-ray absorption fine-structure (NEXAFS), also referred to as XANES (X-ray absorption near edge structure), is determined. The extended X-ray absorption fine-structure (EXAFS) is measured in an energy range of up to several hundred eV above the edge. Though the two have the same physical origin and can be measured with the same experimental setup, this distinction is convenient for the interpretation. NEXAFS is strongly sensitive to the local bonding of the absorbing atom [1]. It changes, for example, with the oxidation state. EXAFS is used to determine the distances, coordination number, and species of the neighbors of the absorbing atom. It results from the backscattering of the photoelectron at neighboring atoms. Also the so-called embedded atom EXAFS (AXAFS) which stems from scattering at charge densities between the atoms was revealed in the extended energy range [35]. The weak scattering and short mean free path of the excited photoelectrons in the EXAFS regime allow an analysis by a single-scattering theory. The structural parameters are derived by Fourier transform techniques. In Ref. [36] a review is given. In the near edge regime strong scattering and a longer mean free path of the photoelectrons require the application of a multiple scattering theory. The magnetic EXAFS (MEXAFS) is the counter part of XMCD in the extended energy range [37–42]. They both yield magnetic information from the difference of the absorption spectra for the two relative orientations of photon spin and sample magnetization. The work presented in this thesis is mainly restricted to the near edge region.

NEXAFS

Experimental NEXAFS spectra provide a sensitive fingerprint of the local structure of the absorbing atom, in particular when recorded for different angles φ between the photon wave vector of the incoming X-rays and the surface of the sample [1, 43]. They have proven useful especially for atoms and molecules adsorbed on surfaces. With the help of full multiple scattering NEXAFS calculations different possible surface structures may be distinguished [43]. The absorption coefficient can be interpreted as a direct measure of the angular momentum projected density of unoccupied states (LDOS) [19, 44]. This may be easily understood from the simple picture that an electron can only be excited if it “finds” an empty final state. Thus, the more unoccupied final states there are the more electrons can be excited and the more photons are absorbed, which means larger X-ray absorption coefficient.

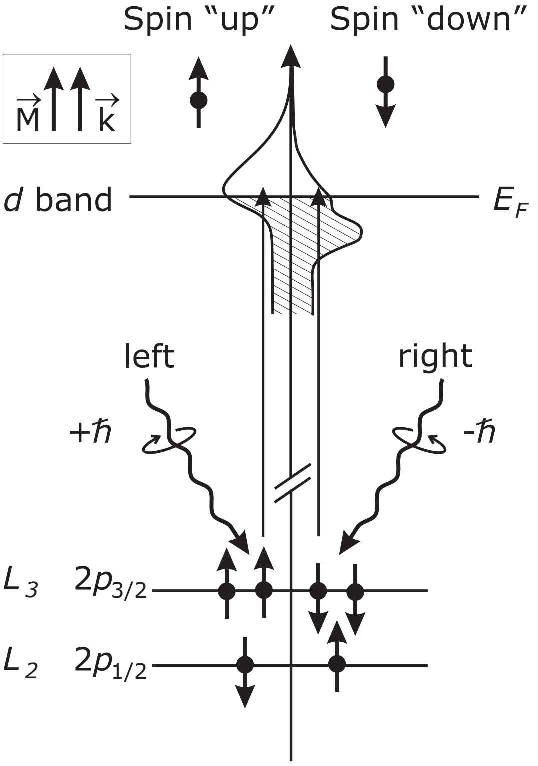

Figure 2.1: Illustration of the two step model for XMCD [2]. In the first step spin-polarized photo electrons are generated. In the second step they are "detected" by the spin-split final states.

XMCD

XMCD is a direct consequence of the dependence of the absorption cross section on the magnetic state. It is defined as the difference $\Delta\mu(E) = \mu^+(E) - \mu^-(E)$ of the absorption coefficients $\mu^+(E)$ and $\mu^-(E)$ for right and left circularly polarized X-rays. Changing the helicity of the incoming X-rays at a fixed magnetization direction of the sample is equivalent to fix the helicity and change the magnetization direction of the sample [2, 3, 19].

Two definitions of left and right are used in literature when describing circular polarization. Here, the convention of optics is used [45]. X-rays with positive ($+\hbar$) helicity (or photon spin) are called left-circularly polarized. Note that the helicity definition is unambiguous. X-rays emitted from a synchrotron source are left-circularly polarized when the electrons in the storage ring seem to turn left, i.e. counterclockwise, from the point of view of the sample. Particle physicist use in general the opposite definition of left and right.

The basic principle of XMCD is explained by a simple two step model [2]. The principle of the model is illustrated in Fig. 2.1. The evaluation of the transition matrix elements yields a spin polarization of the excited electrons due to the spin-orbit coupling ("Fano effect") [46]. Left (right) circularly polarized X-rays excite more spin-up (spin-down) electrons from the $2p_{3/2}$ level. The opposite is the case for the $2p_{1/2}$ level. This happens in the first step. In the second step, the final states determined by the selection rules act as a spin detector. The quantization axis of the detector is given by the magnetization direction. For maximum dichroic effect, the magnetization needs to be aligned parallel to the photon wave vector. If there is an angle ϑ between the two, the XMCD signal will be scaled by $\cos\vartheta$. Ignoring spin-orbit coupling for the final states, a ratio of 2:1 for the white line intensities of the L_3 edge and the L_2 edge is expected for unpolarized radiation, reflecting just the number of sublevels of the $2p_{3/2}$ and $2p_{1/2}$ shell. For the XMCD a ratio of $\Delta\mu_{L_3} : \Delta\mu_{L_2} = -1 : 1$ occurs in absence of spin-orbit coupling of the final states [19, 20].

Spin and orbital moments are related to the integrated areas of the XMCD and the isotropic XAS by the integral sum rules. In its form for general edges as developed by Thole and Carra the orbital sum rule is [47]

$$\frac{\int_{j^+ + j^-} dE(\mu^+ - \mu^-)}{\int_{j^+ + j^-} dE(\mu^+ + \mu^- + \mu^0)} = \frac{1}{2}\frac{\ell(\ell+1) + 2 - c(c+1)}{\ell(\ell+1)(4\ell+2-n)}\langle L_z \rangle \ , \tag{2.9}$$

and the spin sum rule is [48]

$$\begin{aligned} & \frac{\int_{j^+} dE(\mu^+ - \mu^-) - [(c+1)/c]\int_{j^-} dE(\mu^+ - \mu^-)}{\int_{j^+ + j^-} dE(\mu^+ + \mu^- + \mu^0)} \\ = & \frac{\ell(\ell+1) - 2 - c(c+1)}{3c(4\ell+2-n)}\langle S_z \rangle \\ + & \frac{\ell(\ell+1)[\ell(\ell+1) + 2c(c+1) + 4] - 3(c-1)^2(c+2)^2}{6lc(\ell+1)(4\ell+2-n)}\langle T_z \rangle \ , \end{aligned} \tag{2.10}$$

where c is the orbital quantum number of the initial state and ℓ the one of the final state, $\langle S_z \rangle$, $\langle L_z \rangle$, and $\langle T_z \rangle$ are the expectation values of the spin operator, orbital operator, and the magnetic dipole operator, respectively. For metallic systems the spin-orbit coupling is weak an its influence on $\langle T_z \rangle$ can be neglected. The number of unoccupied final states in the valence shell which contains n electrons is given by $(4\ell + 2 - n)$. The two spin-orbit split edges are denoted by j^+ and j^-, μ^+ and μ^- represent the measured helicity-dependent absorption coefficients. Eqs. (2.9) and (2.10) become much handier when considered for specific edges. This is shown in Sec. 2.3 for the cases of K and $L_{2,3}$ edges.

Deriving the sum rules Thole and Carra made several assumptions. For the $L_{2,3}$ edges the most important ones are, that only dipole transitions are included, p–s transitions, the exchange splitting of the core levels, and the energy dependence of the wave functions are not considered, and the asphericity of the core states and the difference of $d_{3/2}$ and $d_{5/2}$ are ignored. Therefore, it is important to verify the applicability of the sum rules in each case. For the $3d$ ferromagnets Fe, Co, and Ni they hold in good approximation. However, for the early $3d$ transition metals Ti, V, Cr, and Mn the limited validity of the sum rules is evident [23, 49, 50].

2.3 Analysis of XAS and XMCD Spectra

To obtain the spin-averaged XAS and the XMCD, the absorption is measured as a function of the photon energy both for parallel and antiparallel orientation of the photon spin and the magnetization of the sample. The analysis of the spectra is shown here using the absorption at the $L_{2,3}$ edges of the $3d$ ferromagnet Ni as an example. The other cases, i.e. the O K edge of $3d$ FMs grown with O surfactant discussed in Chapter 4 and the $L_{2,3}$ edges of the $4f$ elements discussed in Chapter 6, are analyzed likewise. Most of the analysis can be done with the help of the XMCD filemanager and the SATEFF code by A. Scherz [23]. The underlying principles are explained in the following.

The measured raw absorption spectra are normalized to the incoming photon flux. The remaining linear background is fitted by a linear function in the pre-edge region and removed by subtraction of this linear function. Thus, one obtains a pair of absorption spectra $\mu^+(E)$ and $\mu^-(E)$ for parallel and antiparallel orientation of photon spin and sample magnetization, respectively. The isotropic XAS, often also called the “white line”, is then given by

$$\mu(E) \quad = \quad \frac{1}{2}\left(\mu^+(E) + \mu^-(E)\right) \tag{2.11}$$

and the XMCD according to the definition above

$$\Delta\mu(E) \quad = \quad \mu^+(E) - \mu^-(E)\ . \tag{2.12}$$

The contribution of linearly polarized light μ^0 to the isotropic XAS can be neglected for the systems studied in this work because the linear dichroism of metals is by orders of magnitude smaller than the circular dichroism [51]. The spectra contain contributions of the dipole transitions $2p \rightarrow d$ (resonance-like peaks), $2p \rightarrow s$ and to the continuum (step-like increase). For the application of the sum rules the contributions of transitions into s and p states ($\sim 2\%$ for the $3d$ FMs) and into the

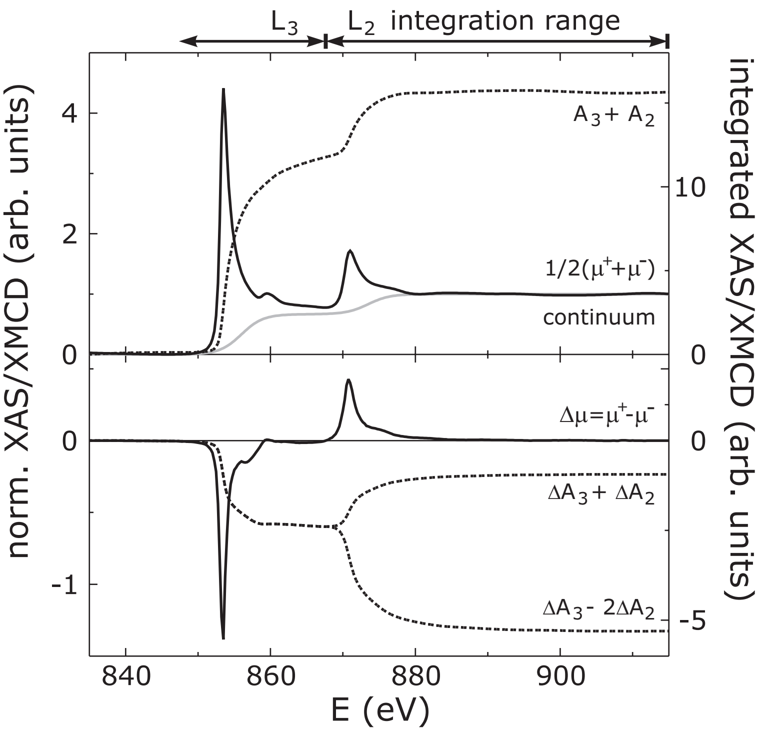

Figure 2.2: Illustration of the application of the sum rules. The case of bulk-like Ni is shown as an example. Top: Normalized isotropic XAS (solid line) together with the integration (dashed line) and the contribution of the continuum (gray line). Bottom: XMCD (solid line) and integrals needed for the sum rule analysis (dashed lines). The integration ranges are marked at the top of the graph.

continuum have to be removed. The continuum is approximated by an *ad hoc* step function [25] of the Fermi-type

$$\mu_{\text{step}} = h\left(1 - \frac{2}{3}\,\frac{1}{1+\mathrm{e}^{(E-E_{L_3}-\varepsilon)/\delta}} - \frac{1}{3}\,\frac{1}{1+\mathrm{e}^{(E-E_{L_2}-\varepsilon)/\delta}}\right)\,, \qquad (2.13)$$

where ε is the position of the step with respect to the position $E_{L_{2,3}}$ of the maxima of the XAS intensity at the $L_{2,3}$ edges, δ is the step width and h the total step height. For the $3d$ FMs, ε and δ are determined from a measured reference spectrum of a bulk-like film such that the application of the sum rules yields the values from literature for the magnetic moments. Finally, the spectra are normalized to unity, to obtain the absorption and the magnetic information on a per atom basis. When measured at grazing incidence ($3d$ FMs, Chapters 4 and 5) or by FY (rare earth elements, Chapter 6), the spectra are corrected for saturation effects [23, 29, 30, 52].

For the application of the sum rules to determine spin and orbital moments, the normalized XAS and XMCD spectra have to be integrated in the range of the considered edges. Therefore, the continuum contribution has to be subtracted from the isotropic spectrum. For the $L_{2,3}$ edges $c = 1$ and $\ell = 2$ enter in the sum rules in their general form of Eqs. (2.9) and (2.10). Defining the number of d holes $n_h = 4\ell + 2 - n$ and the integrated areas of the XAS and the XMCD

$$\Delta A_i = \int_{L_i} \Delta\mu \mathrm{d}E\,, \qquad A_i = \int_{L_i} \left(\frac{1}{2}\left(\mu^+ + \mu^-\right) - \mu_{\text{step}} \right) \mathrm{d}E\,, \qquad i = 2, 3 \tag{2.14}$$

the orbital sum rule recasts to

$$\langle S_z \rangle \;=\; \frac{1}{2}\frac{n_h}{P_c \cos\vartheta}\frac{\Delta A_3 - 2\Delta A_2}{A_3 + A_2} - \frac{7}{2}\langle T_z \rangle\,. \tag{2.15}$$

The spin sum rule becomes

$$\langle L_z \rangle \;=\; \frac{2}{3}\frac{n_h}{P_c \cos\vartheta}\frac{\Delta A_3 + \Delta A_2}{A_3 + A_2}\,. \tag{2.16}$$

The factor $1/(P_c \cos\vartheta)$ accounts for the fact that the XMCD signal scales with the degree P_c of circular polarization and the angle ϑ between the X-ray beam and the magnetization of the sample. An example for the application of the sum rules is given in Fig. 2.2 for the specific case of bulk-like Ni. The upper panel shows the normalized XAS (solid black line), the step-function (gray line) and the integral over the XAS of which the step-function has been subtracted (dashed line). The lower panel shows the normalized XMCD (solid line) and the two integrals of it as they enter into the sum rules of Eqs. (2.16) and (2.15) (dashed lines). Note that the respective scale for the integrals is given on the right hand side.

If the initial state level is not spin-orbit split, as for example at K edges, the XMCD will yield only information about the orbital moment. In the orbital sum rule the integrals are taken only over the single edge j with the areas A of the XAS and ΔA of XMCD. The spin sum rule is no longer properly defined because the initial states are not spin-orbit split. This situation occurs at K edges where $c = 0$ and $\ell = 1$. One obtains

$$\langle L_z \rangle \;=\; \frac{n_h}{P_c \cos\vartheta}\frac{\Delta A}{A} \tag{2.17}$$

for the orbital sum rule.

The magnetization M of the sample is obtained from the spin magnetic moment m_S, the orbital magnetic moment m_L, and the atom density n

$$M = n\,(m_S + m_L) = -n\,(2\,\langle S_z \rangle + \langle L_z \rangle)\,\mu_B\,. \tag{2.18}$$

If only the total magnetization is to be examined without separation into spin and orbital moments, it is sufficient to evaluate the asymmetry of the XMCD $\Delta A_3/A_3$. Assuming that the ratio of orbital to spin magnetic moment does not change, this asymmetry is in good approximation proportional to the magnetization and can thus be used to determine the temperature-dependence of the magnetization. To obtain the magnetization in absolute units, the XAS and XMCD of a bulk-like film with known magnetization are measured. From the ratio $\Delta A_3/A_3$ of this bulk-like film and its known magnetization the scaling factor can be determined.

A further quantity which is often evaluated is the ratio of orbital to spin moment, e.g. [53, 54]. It is given by the relation:

$$\frac{m_L}{m_S} = \frac{2}{3}\frac{\Delta A_3 + \Delta A_2}{\Delta A_3 - 2\Delta A_2} \tag{2.19}$$

In this ratio, uncertainties of the number of holes and the degree of circular polarization cancel out.

2.4 Magnetic Coupling in Ultrathin Films

For the description of magnetic ordering phenomena, mainly two general models are applied: the Hubbard model based on a band structure description and in general applied to itinerant magnetic systems, and the Heisenberg model assuming localized spins and therefore in general used for localized systems. For the magnetism of the $3d$ transition metals, that represent an intermediate case between localized and fully itinerant systems, theoretical models of both types were applied and could successfully describe experimental findings. An example are the coupled Co/Cu/Ni trilayers. Both the calculations within a Hubbard model of Ref. [55] and within a Heisenberg model of Ref. [14] compare well with experimental findings.

In the present thesis, the model proposed by P. Jensen to describe the magnetic coupling in coupled trilayers is applied [14, 58, 59]. The model is based on a Heisenberg Hamiltonian considering the isotropic exchange, the Zeeman term, and the dipole interaction [14, 59],

$$\begin{aligned}\mathcal{H} &= -\frac{1}{2}\sum_{\langle i,j\rangle} J_{ij}\,\vec{S}_i\vec{S}_j - \mu_0\,\vec{H}\sum_i \vec{m}_i \\ &\quad +\frac{\mu_0}{2}\sum_{\substack{i,j\\ i\neq j}} \frac{1}{r_{ij}^5}\left[\vec{m}_i\vec{m}_j r_{ij}^2 - 3(\vec{r}_{ij}\vec{m}_i)(\vec{r}_{ij}\vec{m}_j)\right] .\end{aligned} \tag{2.20}$$

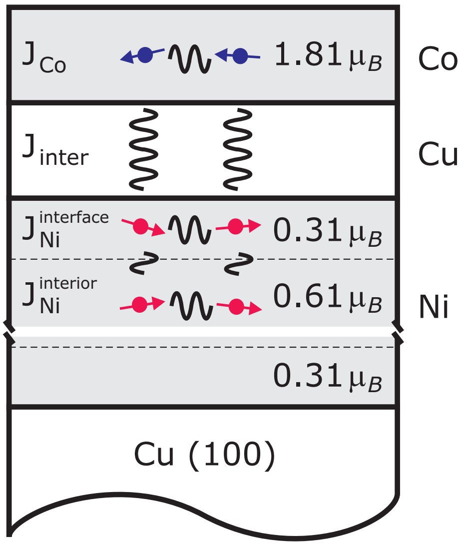

Figure 2.3:
Sketch of the investigated Co/Cu/Ni/Cu(100) trilayers and the underlying assumptions for the theoretical model. For the Ni film the exchange of the interface ($J_{\mathrm{Ni}}^{\mathrm{interface}}$) and the interior film layers ($J_{\mathrm{Ni}}^{\mathrm{interior}}$) are distinguished, whereas for the Co layer a constant exchange J_{Co} is assumed. The Ni and Co spins next to the spacer layer are coupled by the interlayer exchange J_{inter}. Magnetic moments are taken from experiments [56, 57].

In Chapter 5 the specific case of Co/Cu/Ni/Cu(100) trilayers is considered. An fcc(100) thin film system with thickness $d = d_{\mathrm{Ni}} + d_{\mathrm{Co}}$ is assumed. $\vec{S}_i$ denotes a localized quantum spin with spin number $S = 1$ on lattice site i. The magnetic moment of the spin $\vec{S}_i$ is set to the layer-dependent values $\vec{m}_i = m_i \vec{S}_i / S$ determined in experiments and given in Fig. 2.3 [56, 57]. According to the situation in the real samples, an in-plane magnetization $\langle \vec{S}_i \rangle = \vec{M}_i(T)$ parallel to the external magnetic field $\vec{H}$ is assumed. The distance between sites i and j is given by $|\vec{r}_{ij}| = r_{ij}$, μ_0 is the vacuum permeability. The wave vector-dependent lattice sums are determined by the so-called “Ewald summation technique” [60]. Due to competing lattice anisotropies and dipole interaction, the single Ni/Cu(100) thin film system exhibits a spin reorientation behavior with increasing thickness and temperature [61, 62]. The surface anisotropy and the dipole coupling prefer an in-plane magnetization, the strain-induced lattice anisotropy of the interior film layers prefers a perpendicular one. The considered thicknesses in Chapter 5 are always chosen such that an in-plane magnetization of the Ni film occurs. As long as an in-plane magnetization exists, considering explicitly a lattice anisotropy as discussed in detail in Ref. [63] will not vary the results significantly. The reason is that for a 2D ferromagnet the Curie temperature depends only logarithmically on the actual values of the anisotropies [64]. Thus, for simplicity no additional lattice anisotropy is taken into account here. The isotropic exchange interaction J_{ij} couples nearest neighbor spins in the same layer and between adjacent layers (Fig. 2.3). To account for the hybridization effects in particular at the Ni/Cu interfaces where the magnetic moment of Ni is considerably reduced [56, 65], different exchange couplings are assumed for the interface $J_{\mathrm{Ni}}^{\mathrm{interface}}$ and the interior film layers $J_{\mathrm{Ni}}^{\mathrm{interior}}$. For the Co layer an averaged value J_{Co} is used for all Co spin pairs since (i) in Co the effect is less pronounced than in Ni, (ii) the reduction of the Co moment at the Co/Cu interface is approximately canceled out by the enhancement of the moment in the topmost layer facing vacuum [57]. Finally, (iii) assuming layer-resolved values for Co will hardly change the results obtained for the Ni magnetization. The Ni and Co layers are coupled by J_{inter} across the Cu spacer layer, where for simplicity a single Ni spin at the Ni/Cu-interface is coupled to a single Co spin at the Co/Cu-interface. A dispersion of the IEC is not considered.

Since for layered magnets it is important to take collective magnetic excitations (spin waves) into account [14, 58], a many-body Green's function approach is applied for the calculation of the layer-dependent magnetizations [64, 66]. When considering the spin-spin correlation function $\partial/\partial t \langle\langle S_i^+ S_j^- \rangle\rangle$ it is not sufficient to include only the first term, which is the mean field contribution, of the expansion

$$S_i^z S_j^+ \rightarrow \langle S_i^z \rangle S_j^+ - \langle S_i^- S_i^+ \rangle S_j^+ - \langle S_i^- S_j^+ \rangle S_i^+ + \ldots \tag{2.21}$$

The second term is equally important and included in the so-called random phase approximation (RPA).

In detail, the following Green's functions in energy space are used,

$$G_{ij}^{+-(n)}(\omega, \vec{k}_\parallel) = \langle\langle S_i^+ ; (S_j^z)^n S_j^- \rangle\rangle_{\omega, \vec{k}_\parallel} \, , \tag{2.22}$$

where the operator $(S_j^z)^n S_j^- = C_j^{(n)}$ is introduced to consider arbitrary spin quantum numbers ($0 \leq n \leq 2S-1$) [66]. A Fourier transformation into the 2D momentum space with wave vector $\vec{k}_\parallel$ has been performed, the labels i and j in Eq. (2.22) refer to the layer index. Higher-order Green's functions appearing in the equations of motion are approximated by the Tyablikov decoupling [67] ($\widehat{=}$RPA) of the exchange and dipole interaction terms ($i \neq k$),

$$\langle\langle S_i^z S_k^+ ; C_j^{(n)} \rangle\rangle \approx \langle S_i^z \rangle \langle\langle S_k^+ ; C_j^{(n)} \rangle\rangle = M_i(T)\, G_{kj}^{+-(n)} \, . \tag{2.23}$$

The expectation values $M_i(T)$ are determined from the spectral theorem [64]. This approximation allows to calculate the magnetization not only at low temperatures, but also at elevated temperatures, because the interaction between magnons is partly taken into account.

Chapter 3

Experimental Details

The experiments of the present work were carried out at modern third generation synchrotron sources. This chapter describes details of the experiments. The first section concerns the measurements at the $L_{2,3}$ edges of the classical ferromagnets Ni, Co, and Fe, as well as at the O K edge in the energy range of 500 eV $\lesssim E \lesssim$ 1000 eV. Ultrathin films of Fe, Co, and Ni combined in Co/Cu/Ni trilayers or grown with O as a surfactant were prepared in UHV and measured *in situ*. Besides a summary of the characteristic features of the beamline, details of the UHV chamber and the sample preparation are given. The second section of this chapter describes details about the new water-cooled *in situ* coil system which has been constructed and set into operation in the existing UHV chamber during the work for the present thesis. Finally, the last section is about the beamline and the experimental chamber provided at the ESRF which were used to investigate single crystals of the rare earth metals Gd, Tb, and Dy at their $L_{2,3}$ edges (7 keV $\lesssim E \lesssim$ 9 keV).

3.1 General Remarks on Synchrotron Radiation Sources

Synchrotron radiation is very popular for scientific applications because it is available in a large photon energy range from the far infrared ($E < 0.5$ eV) to the very hard X-ray regime ($E \approx 10^6$ eV), see e.g. Refs. [69, 70]. At the beginning, this radiation was only an undesirable side effect at accelerators used by the particle physicists. When electrons (or other particles) travel on an orbit, they emit electromagnetic radiation and loose kinetic energy. Since the idea that the emitted radiation of these particle accelerators may be exploited as well [71], great development has taken place until with today's synchrotrons of the third generation bright light sources with a

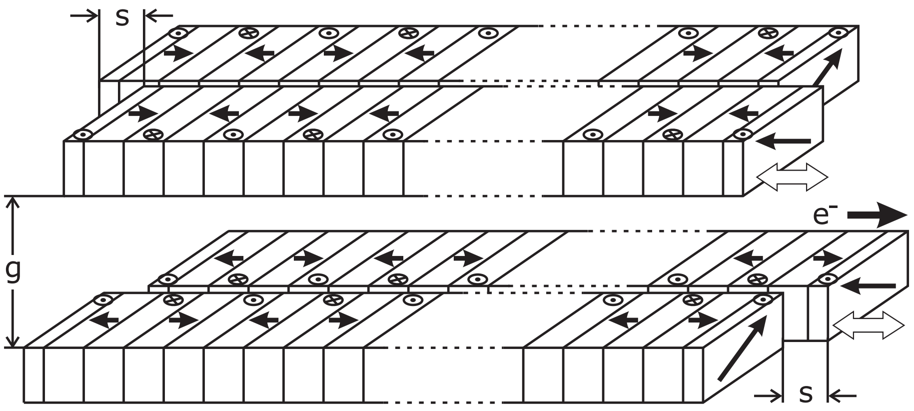

Figure 3.1: Schematic view of a helical undulator for the generation of X-rays with variable polarization by Sasaki [68].

very high spectral resolution are available. They serve now exclusively as light sources. The characteristic parts of such a third generation synchrotron are the insertion devices (IDs) installed in straight sections of the storage ring. One type of IDs are the undulators. Sasaki *et al.* proposed the idea for the design of today's undulators to generate variably polarized radiation, in the meantime also known as the APPLE (Advanced Planar Polarized Light Emitter) devices [68, 72]. Such a helical undulator consists of two pairs of planar magnet arrays above and below the electron beam. Figure 3.1 shows a helical undulator schematically. The energy of the emitted radiation is adjusted by the vertical gap g between the magnet arrays. The polarization state depends on the position shift distance s (phase shift) between the right and the left magnetic array in each pair. The undulator forces the electron beam to execute a helical trajectory to emit elliptically polarized radiation. In the first harmonic a circular polarization degree of up to 100 % is possible. At zero shift, linearly polarized light is emitted. In contrast to the emission spectrum of a simple bending magnet, the spectrum of an undulator is rather narrow in energy due to constructive interference of the radiation emitted by the electrons at each point of their deflection. However, an undulator provides by orders of magnitude more photon flux and brilliance. The gap scan mode drives the undulator and the monochromator simultaneously such that the maximum of the undulator peak and the energy selected by the monochromator coincide. In this mode undulator beamlines provide the radiation with high photon flux and constant and high degree of circular polarization [73].

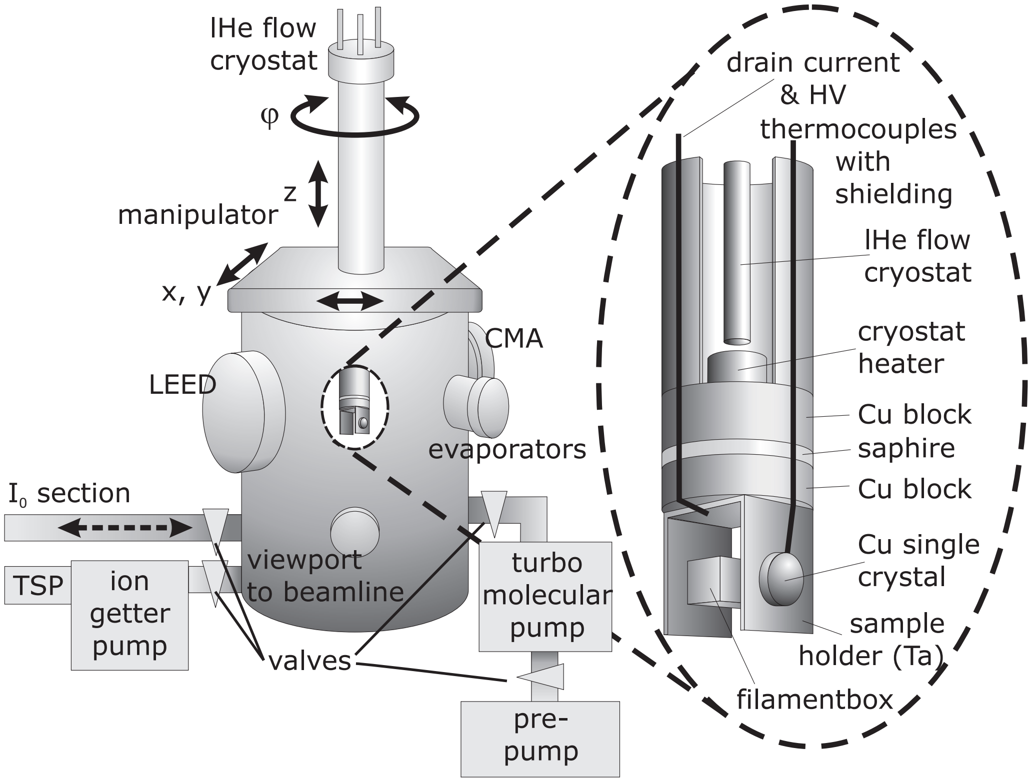

Figure 3.2: Sketch of the UHV chamber used for the XAS and XMCD measurements in the soft X-ray regime at BESSY. The magnification shows the sample holder in detail.

3.2 Measurements in the Soft X-Ray Regime at BESSY

Investigations by XAS and XMCD at the $L_{2,3}$ edges of $3d$ ferromagnets and at the O K edge were carried out at BESSY (Berliner Elektronenspeicherring-Gesellschaft für Synchrotronstrahlung m. b. H.) in Berlin-Adlershof (electron energy 1.7 GeV) [74]. In this case the need of soft X-rays requires a UHV chamber with the equipment for the sample preparation that can be directly attached to the vacuum of the beamline. In this section details of the UHV chamber which was used for the experiments in the soft X-ray regime, the sample holder, the preparation of the samples, the beamlines, and the general data acquisition procedure are described.

The UHV Chamber

The experimental station for the measurements in the soft X-ray regime at BESSY is a cylinder-like UHV chamber made of stainless steel [75] as illustrated in Fig. 3.2. In the upper part it contains commercial standard equipment for the preparation of ultrathin films and their characterization: a sputter gun, a leak valve for O_2 dosage, and evaporators, a rear view system for low energy electron diffraction (LEED) and a cylindrical mirror analyzer (CMA) for Auger electron spectroscopy (AES). The chamber is attached to the beamline such that in the lower part the X-ray absorption can be measured. The coil system for generating a magnetic field is mounted there. Details of the coil system are described in Sec. 3.3. Furthermore, the chamber contains standard components for creating and controlling the vacuum itself. This includes a turbo molecular pump with a pre-pump, an ion getter pump with a titanium sublimation pump (TSP), an ion gauge, and a quadrupole mass analyzer. Additionally, a cold cathode provides a live pressure signal required by the BESSY interlock system for the safety of the machine. The base pressure of the chamber is typically in the low 1×10^{-10} mbar range.

The sample holder is a u-shaped bended tantalum plate mounted at the cooling tip of a ℓHe-flow cryostat (see Fig. 3.2). It has been designed to combine the requirements of a delicate experiment with those of a robust system, reliable and easy to handle at a research facility where only strictly limited beamtime is available. The compact design helps to reduce vibrations of the sample holder due to the ℓHe-flow while cooling. Two crystals are mounted back to back of each other on the Ta plate. A chromel/alumel thermocouple is plugged to the side of each crystal. The thermocouple wires are insulated with macor tubes and electrically shielded with aluminum foil. The electric shielding is necessary to keep the induced noise on the sample current low. A commercial feedback heating system stabilizes the temperature of the samples in the range $25\text{ K} \leq T_{\text{sample}} \leq 300\text{ K}$ within 1 K during the measurements. The vacuum of the chamber itself serves at the same time as the insulation vacuum for the cryostat. For the low-level drain current measurements the samples have to be highly insulated from ground ($R_{\text{sample}} > 200\text{ G}\Omega$). Therefore, a sapphire plate is used which at the same time guarantees a good thermal contact to the cooling tip of the cryostat. Especially the feedthroughs of the cables are sources of trouble. They are located close to the entry point of the transfer tube for the liquid helium at the top of the cryostat. During the cooling they tend to become cold and attract the water vapor from the air. This reduces the resistance of the sample and hinders high quality measurements. Therefore, a thin heating wire is winded around the flanges that contain the relevant feedthroughs. To bring the sample to the different positions for preparation and measurement all three room directions x, y, z, and the polar angle φ can be adjusted via a manipulator with a differentially pumped rotary feedthrough.

In principle, the chamber itself provides the possibility to measure a signal proportional to the intensity I_0 of the incident light: the photocurrent of a gold grid. This I_0 section was used together with the former pulse coil for remanent measurements [23]. Due to the geometric constraint it cannot be used together with the new coil system. Anyway, even if it still fitted in its old position, it would not be suitable for measurements in an applied magnetic field because its position close to the coil leads to a dramatic influence of this field on the photocurrent and thereby hinders the measurement of a proper I_0-signal. At the concerned beamlines at BESSY this problem is easily circumvented by taking the photocurrent of either the last refocusing mirror or a gold grid (90 % transmission) in the beamline. The gold grid can be moved into the beam just before the last mirror via a linear motion. In each beamtime one of the two possibilities was chosen depending on which of them showed less noise.

Sample Preparation

Ultrathin films of the classical ferromagnets Fe, Co, and Ni on Cu single crystals were prepared and measured *in situ* in the UHV chamber described above. The Cu substrates, Cu(100) and Cu(110), were cleaned in a conventional way by repeated cycles of Ar^+ sputtering at 45 degrees incidence and subsequent annealing to $T \approx 800$ K by electron bombardment at the back side of the sample. The accelerating voltage of the Ar ions was 3 kV in the first cycle for the Cu(100) crystal. In all following cycles 1 kV was used. The Cu(110) crystal was only sputtered at 1 kV. This procedure cleaned the surface of the crystals (also from old films on them) and healed it from imperfections [76]. Characterizing experiments by STM have shown that a mean terrace size of at least 100 nm can be achieved on the crystals used in the present experiments [77]. The films of Fe, Co, and Ni were evaporated from high-purity rods in a commercial electron beam evaporator. Cu was evaporated by the same procedure from high-purity material in a Mo crucible. Special care was taken not to deposit any metallic material onto the side of the insulating sapphire plate. The pressure inside the chamber stayed below $p < 4 \times 10^{-10}$ mbar during evaporation. The film thickness was calibrated with AES and MEED. Where suitable, the $L_{2,3}$

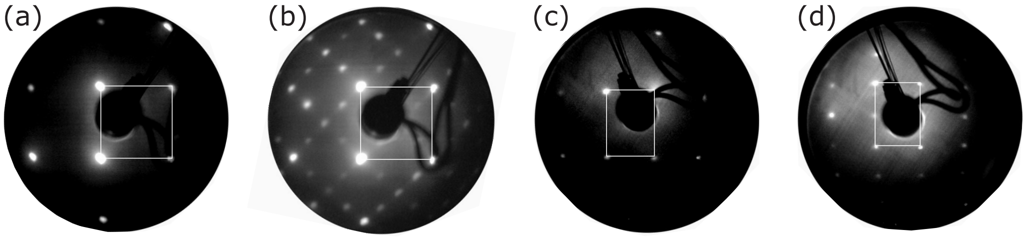

Figure 3.3: LEED patterns of the Cu substrates showing the characteristic superstructure spots of the O reconstructed surfaces: (a) clean Cu(100), (b) $\mathrm{O}(\sqrt{2} \times 2\sqrt{2})\mathrm{R}45^\circ$ Cu(100), (c) clean Cu(110), and (d) $\mathrm{O}(2 \times 1)$ Cu(110). The patterns (a) and (b) were taken at an electron energy of 217 eV, the patterns (c) and (d) at 230 eV. The white rectangles highlight the elementary cell of the pattern of the clean Cu crystals thus revealing the extra spots which appear due to the O adsorption and the reconstruction of the Cu surface. The patterns are rotated such that their orientation corresponds to the orientation of the crystals during the measurements of the XAS and the XMCD.

edge jumps were used for a crosscheck [78]. The accuracy of the thickness calibration, typically given in monolayer (ML) equivalents, is estimated to be 5 %. The evaporation rates were controlled by a flux monitor installed on the evaporator and by the drain current of the sample. They were kept constant during the film growth and typically in the range of 0.1 ML per minute to 0.6 ML per minute.

To grow ferromagnetic films of Fe, Co, and Ni with O as a surfactant, the following procedures were applied [77]: First, O was adsorbed onto the cleaned Cu crystals. On the Cu(100) surface an $\mathrm{O}(\sqrt{2} \times 2\sqrt{2})\mathrm{R}45^\circ$ reconstruction was prepared by dosing 1200 L (2 min at $p = 1 \times 10^{-5}$ mbar) of oxygen into the chamber at a temperature of the Cu crystal of about 500 K. Dosing 12 L (2 min at $p = 1 \times 10^{-7}$ mbar) of oxygen at room temperature and annealing the substrate to $T \approx 400$ K led to the $\mathrm{O}(2 \times 1)$ reconstruction of the Cu(110) surface. The O coverage corresponds to 0.5 ML. In both cases the reconstruction was verified by LEED revealing the characteristic superstructure spots. Figure 3.3 shows exemplary LEED patterns of the clean and the O reconstructed Cu surfaces taken in the laboratory. The LEED patterns are rotated such that their orientation corresponds to the orientation of the crystals during the measurements at the synchrotron. The nonperfectness of the spots (symmetry, brightness etc.) is due to the nonperfect alignment of the sample with respect to the LEED screen because of geometrical constraints by other equipment inside the UHV chamber. Although the LEED system is not perfectly accessible because it is not the key component of the chamber, it is very valuable to crosscheck the properties of the specific samples that are measured at the synchrotron. The ferromagnetic films of Fe, Co, and Ni were finally evaporated in the usual way onto the O reconstructed Cu surface.

Data Acquisition

The absorption of the samples was detected via the TEY by measuring the sample current. As explained in Sec. 2.1, the absorption will be proportional to the sample current if certain conditions are fulfilled. For a simultaneous determination of the incoming photon flux I_0, either the photocurrent of a gold grid in the incident beam or of the last mirror of the beamline (see above) was recorded. The measured XAS were divided by the I_0 signal, corrected for a linear background at the pre-edge and normalized to the edge jump. The XMCD spectra were obtained by either reversing the magnetization of the films or the helicity of the incident X-rays and taking the difference between the X-ray absorption coefficients for the two directions. By this cross-check an artificial magnetic background in the magnetic dichroism could be ruled out. In many cases, artificial magnetic background signals are reversed when the helicity of the incident light is reversed. Therefore, these background signals can often be removed from the XMCD signal by averaging an equal number of spectra taken with each helicity. Such backgrounds are typically below one percent of the XMCD, if they occurred at all. Since XMCD always probes the projection of the magnetization onto the direction of the incident X-rays, samples with an out-of-plane magnetization were measured at an angle $\varphi = 90°$ between the surface of the sample and the photon wave vector, whereas samples with an in-plane magnetization were measured at grazing incidence of $\varphi = 20°$. The spectra were analyzed according to the details described in Sec. 2.3. This has either been done with the help of the XMCD filemanager and the SATEFF code by A. Scherz [23] or with the commercially available software Origin 7 by OriginLab Corporation. The data recording itself was done with the EMP/2 software developed at BESSY. This software together with the data acquisition computer from BESSY enables the users to record their signals by TTL-counter, voltage or current measurement. At the user's choice these signals are written to a data file along with the current of the storage ring, monochromator position, and lifetime. This data file is a simple ASCII-file and can be processed later in almost every standard data analysis software like e.g. Origin or any home-made analysis programs. Via the EMP/2 program the monochromator and the undulator are remote controlled. Thus, it is possible to scan the energy of the incoming photons with a user-defined density of points, lately even with the so-

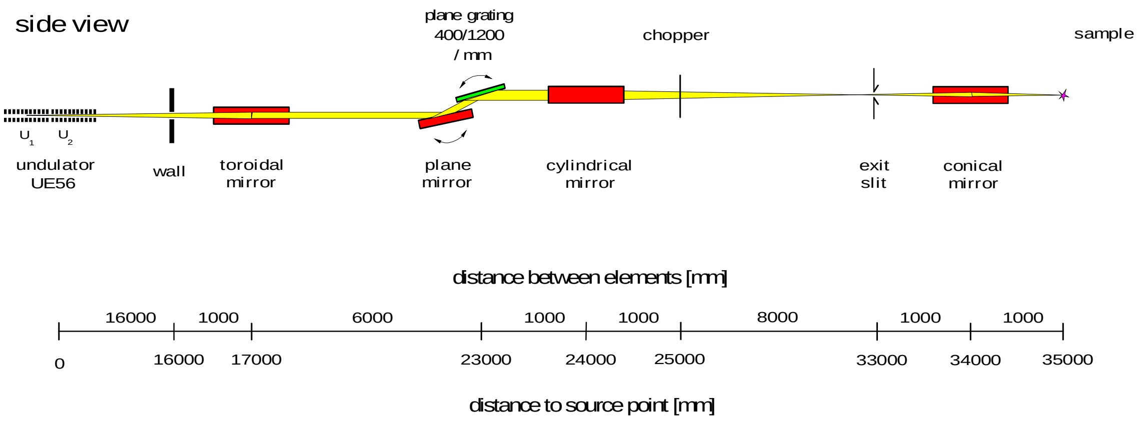

Figure 3.4: Schematic layout of the UE56-PGM beamlines at BESSY [79].

called regions, i.e. different density of points in different energy ranges within the same scan. To record $M(T)$ the timescan mode was used. In this mode, the photon energy is set to a constant value and the various signals are recorded as a function of time at user-defined time intervals. A number of other modes of operation are available in the EMP/2 software, but they were not used for the present work.

The UE56-PGM Beamlines

The source of the UE56-PGM beamlines is a Sasaki type elliptical undulator [68, 72] with high remanent NdFeB permanent magnets. The emission of these undulators in the third harmonics provide the X-rays in the energy range needed for the XAS and XMCD experiments in the range of the $L_{2,3}$ edges of the $3d$ ferromagnets and the O K edge. The beamlines are equipped with a collimated plane grating monochromator (PGM) [80] and refocusing mirrors. Figure 3.4 shows schematically the layout of the UE56-PGM beamlines. Three beamlines of this type have been built up and commissioned at BESSY [81]: The first one is UE56/1-PGM maintained by BESSY staff members. Currently it is modified for slicing experiments and tests with regard to time-resolved experiments. The two other beamlines of this type, UE56/2-PGM1 and UE56/2-PGM2, are maintained by the Max-Planck-society. During the work for this thesis all three beamlines have been used (UE56/1 only before its modification). As they are absolutely equivalent they will just be referred to as the UE56-PGM beamlines. They are designed to preserve the high degree of circular polarization P_c emitted by the undulator, ($P_c > 0.8$ for most of the energy range), to have spectral purity with low higher-order content, and to provide high photon flux at high resolution. The tables used to control the undulator have been optimized such that

Table 3.1: Our standard settings of the UE56-PGM beamlines.

setting	value
undulator	downstream
harmonic	3^{rd}
gap ($500\text{ eV} \lesssim E \lesssim 1000\text{ eV}$)	~ 28 mm to ~ 40 mm for linear polarization ~ 25 mm to ~ 35 mm for elliptical polarization automatically controlled by EMP/2
grating	1200 lines/mm
cff	2.25
apertures	$1 \times 1\text{ mm}^2$ to $2 \times 2\text{ mm}^2$
exit slit	$\sim 170\ \mu$m

a maximum and constant degree of circular polarization is obtained at each energy. Table 3.1 gives the typical settings of various beamline parameters for the present measurements. Actually, the straight section of UE56/2 (and before its modification also UE56/1) contains two undulators at a slight angle with a modulator in between. This allows for a two beam operation where one beam is set to positive helicity and the other to negative helicity. A chopper switches then between the two beams. In principle, it is also possible to couple the two undulators such that they provide one common beam with enhanced flux. This requires the proper adjustment of the modulator to ensure positive interference of the two beams. Since more difficulties result and the higher flux was not necessary, only the undulator which is located closer to the beamline – the so-called downstream ID – was used for the experiments of the present thesis.

3.3 Design and Characterization of a Water-Cooled Coil System for UHV

In the course of this work, XAS and XMCD measurements in an applied magnetic field have finally been established in the existing UHV chamber. Therefore, a new *in situ*, i.e. UHV-compliant, water-cooled coil system has been developed and set into operation. In earlier experiments the magnetization of the sample was reversed by an *in situ* electric pulse driven coil [23, 82]. The samples were then investigated

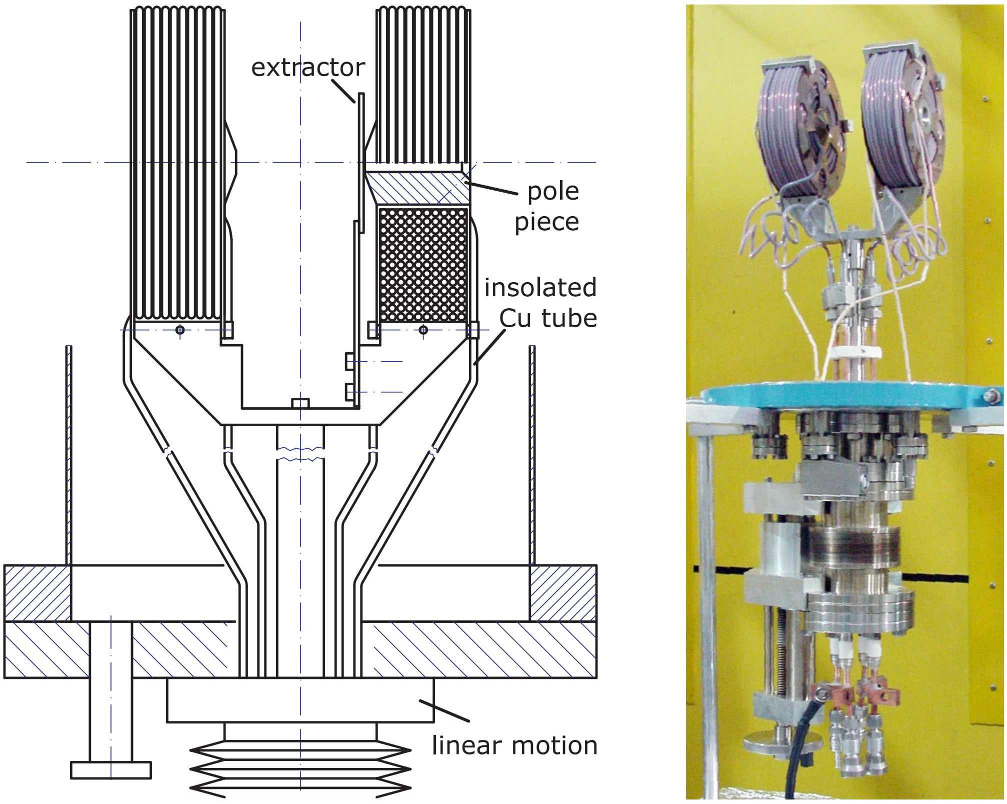

Figure 3.5: Part of the technical drawing of the new water-cooled coil system showing the overall assembly (left) and photograph before final installation on the UHV chamber (right). For the complete drawings see [78].

in remanence. In principle, measurements in small static magnetic fields H were possible but only up to $\mu_0 H \approx 4$ mT to prevent the coil from overheating.

Construction

The basic idea for the design of the new coil system is based on the setup of an existing coil system which is installed on the XMCD chamber at the beamline D1011 at MAX-lab in Lund (Sweden) [83]. The main feature is to make the windings out of Cu tubes which on the one hand carry the current and on the other hand allow for a steady water flow inside of them. A Teflon (PTFE) shrink tube insulates the windings from each other. It is suitable for UHV since it does not degas even during bakeout of the chamber and it can more or less easily be applied to the Cu tubes. The main goal of the new design was to obtain a maximum magnetic field at the position of the sample. As a part of his diploma thesis, M. Bernien calculated the resulting magnetic field as a function of the parameters of the coil system, i.e. geometry of the bobbins, the Cu tubes etc. Thus the parameters could be optimized for the given edge conditions [78]. Figure 3.5 reproduces a part of the technical drawing of the new coil system showing the overall assembly (left) and a photograph before the final installation on the UHV chamber (right). The sample position is in the middle between the coils. The direction of the incident X-rays is along the symmetry axis of the system. Pole pieces of soft iron can be mounted to the bobbins to enhance the magnetic induction at the measuring position of the sample. To ensure a proper measurement of the sample current in applied magnetic fields, an aluminum plate (*"extractor"*) is mounted on an insulating ceramic holder in the direction of the escaping secondary electrons. A hole of 12 mm diameter is drilled into this plate to enable the X-rays to irradiate the sample. The whole coil system is mounted on a linear motion to be able to move it out of the experimental area inside the chamber. This is useful, for instance, when adjusting the chamber to the beamline because the beam is more easily seen on the fluorescence window opposite the beamline flange, or during LEED experiments when the LEED screen is influenced by the stray field of the pole pieces. Four commercial ceramic insulated water-cooled power feedthroughs (1 pin, 5 kV, copper) are welded into the bottom flange. The feedthroughs and the winded Cu tubes are connected inside the UHV by Swagelok VCR Metal Gasket Face Seal Fittings [84]. Water and electric current are separated outside the UHV, simply by screwing the cables to the Cu connections installed on the tubes and using a nonconducting water hose. The electric connection is such that the two coils of the system are in series, whereas the water connection is in parallel. By connecting the water in parallel the temperature of the two coils is kept on the same level. If they were in series, the water would be already warmed up by the first coil when entering the second one.

Characterization of the Magnetic Field

After the coil system had finally been built, the generated magnetic field was characterized with a Hall probe. Figure 3.6 (a) shows the measured strength of the magnetic induction B in the center of the coil system as a function of the applied current I. With the pole pieces (solid circles) the $\vec{B}$ field is by a factor of 1.8 stronger as compared to the case without pole pieces (open circles). With the pole pieces the field increases linearly with the current as $B = (1.74 \pm 0.01)\ \mathrm{mT/A} \cdot I$. This meets M. Bernien's prediction almost perfectly (less than 2 % discrepancy). The dependence of the magnetic field on the geometric position has also been investi-

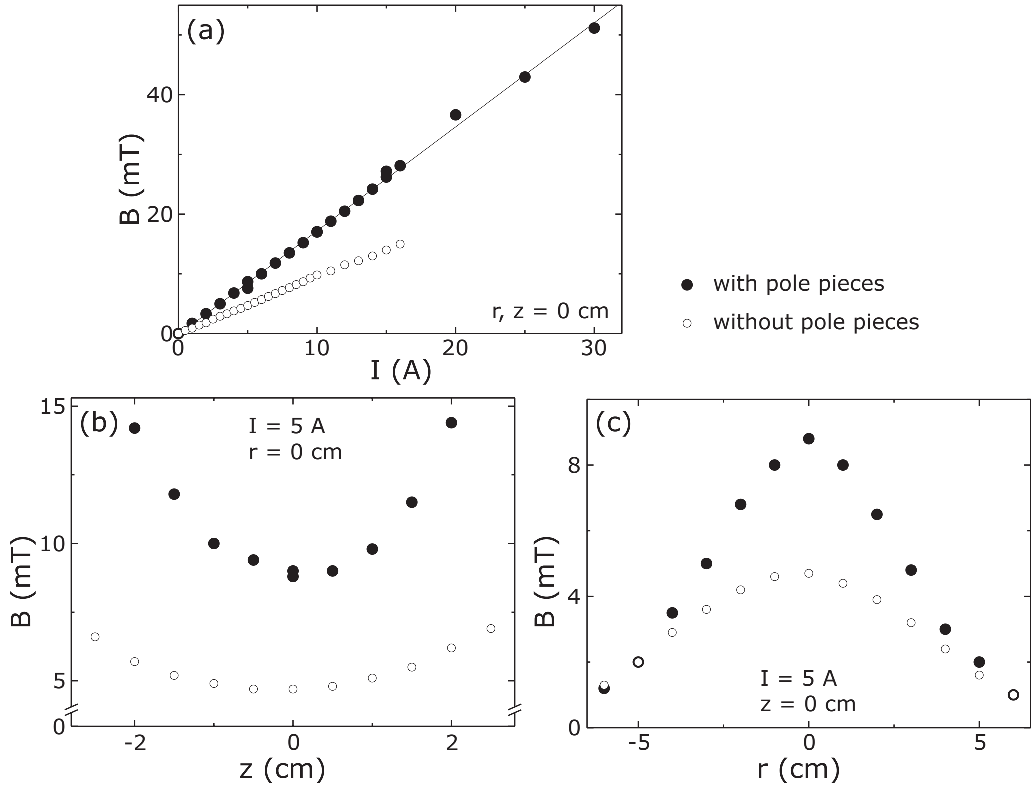

Figure 3.6: Magnetic induction B of the new coil system with (solid circles) and without (open circles) pole pieces (in mT, 1mT$\hat{=}$10 G), (a) in the center between the coils, as a function of the applied current I, (b) along the symmetry axis, as a function of the distance z from the center at I = 5 A, (c) perpendicular to the symmetry axis in the middle between the coils, as a function of the distance r from the center at I = 5 A [78].

gated. In Fig. 3.6 (b) $B(I = 5\text{ A})$ is plotted as a function of the position z on the symmetry axis of the coil system; $z = 0$ cm means the middle between the two coils. Figure 3.6 (c) gives $B(I = 5\text{ A})$ as a function of the distance r from the symmetry axis of the coil system at $z = 0$ cm. The ohmic resistance of the coil system R_{coil} has been determined from a conventional measurement $U(I)$ of the voltage as a function of the applied current. If both coils are in series $R_{\text{coil}} = (0.208 \pm 0.006)\ \Omega$. The inductance L (both coils in series) is $L = (305 \pm 15)\ \mu$H, determined with the help of an L-meter.

3.4 Measurements in the Hard X-Ray Regime at the ESRF

Single crystals of Gd, Tb, and Dy were investigated at the ID12 Circular Polarization Beamline at the ESRF (European Synchrotron Radiation Facility) in Grenoble, France (electron energy 6.03 GeV) [85]. The samples were provided by the group of T. A. Lograsso at Ames Laboratory, Iowa State University. The elements were cleaned and arc melted under an argon atmosphere and the elements drop cast into a copper chill cast mold. The single crystals were then grown from the drop cast ingots by the strain anneal method and cut crystallographically oriented to disks of approximately 10 mm diameter and 2 mm thickness. For the investigations of these elements at their $L_{2,3}$ edges hard X-rays and a large magnetic field ($\mu_0 H$ up to 7 T) to overcome the shape anisotropy of the samples are necessary.

The ID12 beamline is a window-less beamline that provides X-rays in the hard X-ray regime with variable polarization [86]. Historically, it was called ID12A and shared its source with a second beamline ID12B also providing X-rays with variable polarization, but in the soft X-ray regime. However, the interaction of the two beamlines was at some point no longer acceptable also due to the growing demand by users for more beamtime. The ID12B branch has been moved to a different straight section and is now known as the “Dragon Beamline” ID08.

Figure 3.7 shows the layout of the ID12 beamline schematically [87]. The straight section of ID 12 contains three helical undulators: ElectroMagnet/Permanent magnet Hybrid Undulator (EMPHU), HELIOS-II, and APPLE-II. They complement each other to cover the energy range from 2 keV up to 20 keV. According to the required energy range one of the undulators was used in each experiment following the advice of the beamline scientists. If possible, the EMPHU was preferred because this novel undulator allows for fast switching of the polarization state with a helicity reversal time of $\sim$ 160 ms [88]. Thus, the helicity of the incident light can be switched at each energy point, taking the complete XMCD spectra in one single energy scan. Therefore, the XMCD spectra do not suffer from long term drifts of the beam e.g. due to instabilities of the electron beam in the storage ring.

A UHV-compatible double-crystal monochromator with fixed exit is the essential part of the beamline. The pair of Si$\langle 111 \rangle$ crystals is kept at 130 K by cooled He gas. The main drawback of the monochromator is its polarization transfer which depends strongly on the angle of the incident light. XMCD measurements in the lower energy range of the beamline are hindered by the fact that the degree of

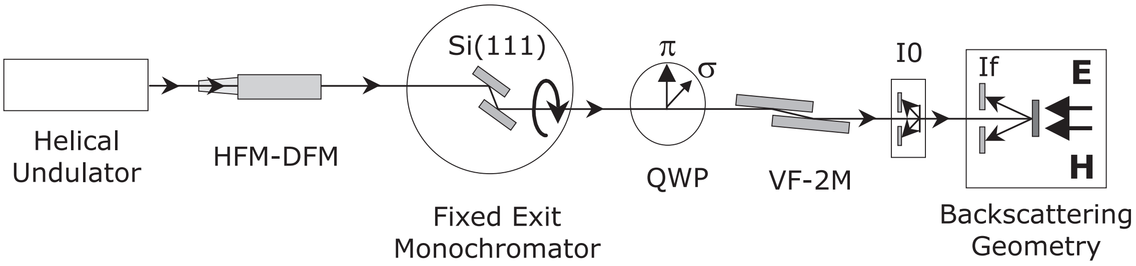

Figure 3.7: Schematic layout of the ID12 beamline at the ESRF. Abbreviations: HFMDFM = horizontally focusing and deflecting mirrors; QWP = quarter-wave plate assembly; VF-2M = vertically focusing double mirror; I0 = photodiode intensity monitor; If = photodiodes to detect the fluorescence yield [87].

circular polarization drops to almost zero between 2.5 keV and 3 keV. In this energy range the monochromator crystal has to be operated close to the Brewster angle of Si$\langle 111 \rangle$ and thus acts as a linear polarizer. Throughout the beamline the X-rays travel various pin holes, slits, and focusing units that serve to prepare the beam properly. The design of the beamline offers the possibility to measure a large variety of dichroic effects in the X-ray regime. Many of these effects have been established in experiments at ID12 [87].

A superconducting magnet in the chamber installed on the beamline provides a magnetic field $\vec{H}$ with $\mu_0 H \leq 7$ T. The chamber possesses a load lock that enables the users to change the sample without breaking the vacuum of the chamber itself. The sample is clamped to the sample holder by a strong metal plate. This plate has a hole in its middle so that the X-rays reach the surface of the sample. With the help of a ℓHe-flow cryostat the sample temperature can be controlled and stabilized down to $T \approx 2$ K. The fluorescence yield is detected by four PNN$^+$ Si photodiodes together with a digital lock-in technique [89]. Using photodiodes as a detector has several advantages: Apart from being fully UHV-compatible they are hardly influenced by magnetic fields which is essential for XMCD measurements. Moreover, they are highly efficient and linear in the X-ray range and provide a fast response time. The measurements are computer-controlled via the SPECS software. The same system records the data and writes them to ASCII-files. In the same manner as for the measurements at BESSY, the data are analyzed with the help of the analysis programs by A. Scherz [23] and Origin 7.

Chapter 4

The Role of Oxygen as a Surfactant for the Magnetism of Fe, Co, and Ni Films

Modern technological devices and nanostructures consist not only of materials in their natural phases. More and more artificial structures with custom-made properties are designed and incorporated in these devices. It is clear that magnetic materials are of special interest for the development of any magnetic devices like today's storage media. Their magnetic properties may dramatically be influenced by minimal structural changes. If the nearest neighbor distance varies by (0.03 – 0.05) Å only, the magnetic anisotropy energy may change by a factor of 100 or 1000 [61, 90]. One well established method to fabricate such artificial structures is nowadays the surfactant assisted growth. It was shown that using oxygen as a surfactant improves the layer-wise and pseudomorphic growth of ultrathin films of Fe, Co, and Ni on Cu substrates. Surfactants may help adsorbates to wet the substrate [5, 6, 91, 92]. They float on top of the deposited layers and thereby reduce the surface free energy [93]. In this chapter the magnetic properties of ferromagnetic films of Fe, Co, and Ni which were grown with oxygen as a surfactant are presented. It is shown how the surfactant influences the magnetism of the ferromagnets themselves. Moreover, the basic physical effect of induced magnetism at the surfactant site, which is the oxygen in the present case, is discussed in detail.

After a short summary of the status of research prior to this work in Sec. 4.1, growth and structure of the samples as they were used in the present XAS and XMCD experiments are described in Sec. 4.2. As the first part of the study, the case of Ni grown on Cu(100) and Cu(110) with O as surfactant is investigated thickness-dependently in comparison to the case without surfactant. Taking advantage of

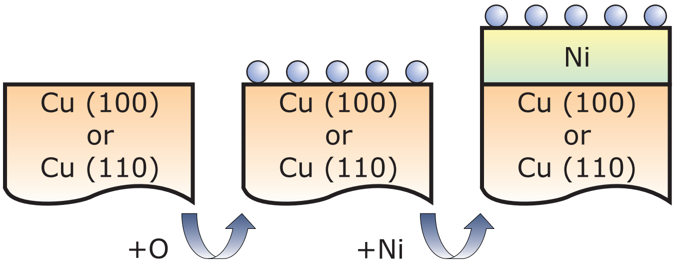

Figure 4.1: Schematic illustration of Ni grown on Cu(100) or Cu(110) with the help of oxygen as an example of surfactant assisted growth. First the surfactant material (O) is adsorbed onto the clean substrate (Cu). The surfactant detaches from the substrate and floats on top when the ferromagnetic film (Ni) is deposited.

the element-specificity of XAS and XMCD the three constituents of each sample, i.e. the O surfactant, the $3d$ FM film, and the Cu substrate, can be investigated individually. In the following Sections 4.3 and 4.4 the results obtained by XAS and XMCD are finally presented, giving information about the electronic structure and the magnetic properties including element-specific spin and orbital moments of the $3d$ FMs. NEXAFS results at the $L_{2,3}$ edges of the $3d$ FMs and the O K edge exclude the formation of bulk-like oxides of Fe, Co, and Ni in the surfactant grown samples. Angular-dependent NEXAFS at the O K edge gives final evidence that the O atoms float on top during the growth of the films. The influence of the O surfactant on the magnetism of the Ni layers is determined from XMCD spectra. A classical standard analysis with the help of the popular sum rules by Thole and Carra *et al.* [47, 48] has been applied and is presented in detail. Due to the sensitivity of the methods at modern synchrotron sources even the magnetic signal of 0.5 ML O can unambiguously be determined. As a second part, the study has been extended to Fe and Co with selected thickness. In this part the focus is turned to the induced magnetism which is observed at the O site. The systematics of the measured XMCD at the O K edge in surfactant grown $3d$ FMs is presented in Sec. 4.5 and finally discussed in comparison to theoretical results in Sec. 4.6.

4.1 Summary of Previous Research

The basic idea of surfactant activity is sketched in Fig. 4.1. The surfactant material, e.g. O, is adsorbed onto the clean substrate, e.g. Cu(100) or Cu(110) prior to deposition of the film, e.g. Ni. The surfactant detaches from the substrate surface and

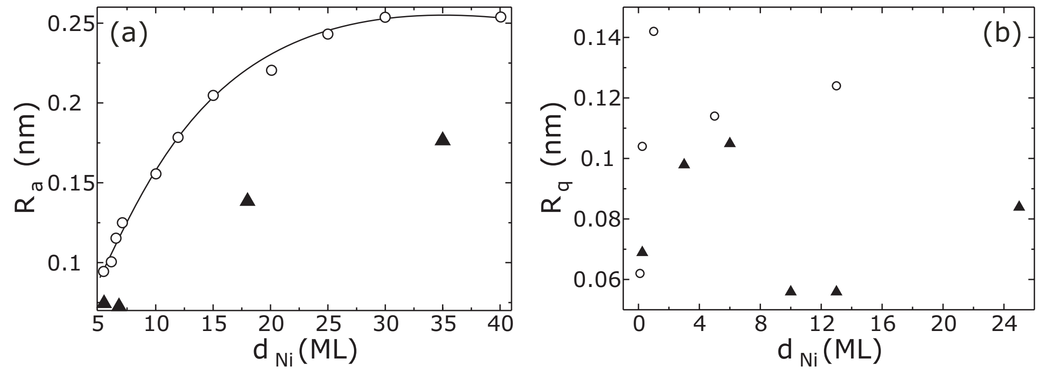

Figure 4.2: (a) Arithmetic mean roughness of Ni films grown on Cu(100) with (triangles) and without (circles) O surfactant. The line serves as a guide to the eye [5, 77]. (b) Mean squared roughness of Ni films grown on Cu(110) with (triangles) and without (circles) O surfactant [77].

floats on top of the growing film. Thus, it can keep its activity as growth proceeds. At the same time no impurities must be introduced in the growing layers. Numerous combinations of substrate, film, and surfactant materials exist where the structure of the ultrathin film has been improved due to the surfactant assisted growth. Examples are lead as a surfactant for Co on Cu(111) [94], arsenic as a surfactant for Ge on Si(100) [93], oxygen as a surfactant for Co on Cu(110) [92], for Co on Fe(100) [95], for Fe on Cu(100) [91], for Fe on single crystalline Fe(100)/MgO(100) [96, 97], and for Ni on Cu(100) [4–6, 98–101].

One of the most popular metallic substrates for ferromagnetic films is the Cu(100) surface. Both structure and magnetism of Fe, Co, and Ni on this surface have been discussed in numerous publications, e.g. [61, 102–105]. Recently, it has been shown that in Ni/Cu(100) oxygen acts efficiently as a surfactant material [4–6]. The layer-by-layer growth mode is extended to a much larger thickness with the help of O as a surfactant. Calculations have shown that the reason is the reduction of the long-range electrostatic (Madelung) energy, when the O atoms float on top of the Ni film [5]. Auger electron spectra suggest that the O stays on top of the growing films. No reduction of the O signal has been observed in the Ni films on O/Cu(100) while the Cu signal is damped away rapidly when Ni is evaporated. The surface of the Ni films, was characterized in detail by LEED and scanning tunneling microscope (STM) experiments [5, 77].

One important result of the STM experiments is the thickness-dependent surface roughness of the films. Fig. 4.2 (a) reproduces the arithmetic mean roughness R_a

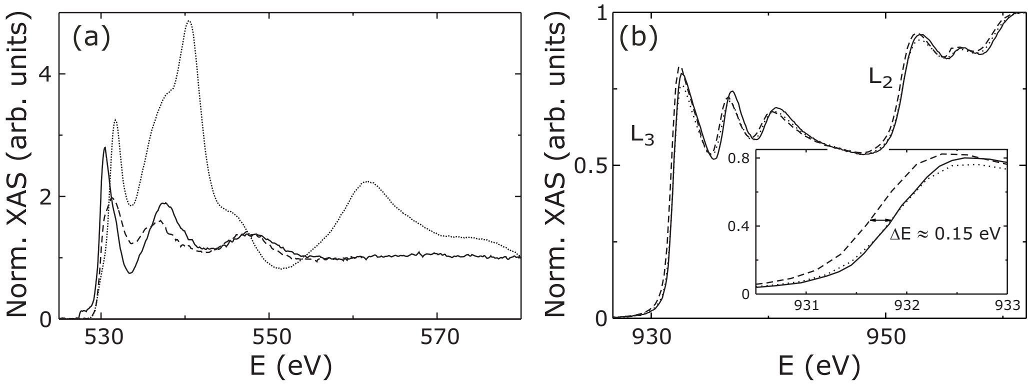

Figure 4.3: (a) Consecutively measured NEXAFS at the O *K* edge of the reconstructed O/Cu(100) surface before (dashed line) and after the deposition of a 4.5 ML Ni film (solid line). For comparison a NEXAFS spectrum of NiO at the O *K* edge is also included (dotted line) [5]. (b) Consecutively measured NEXAFS at the Cu $L_{2,3}$ edges of the clean Cu(100) surface (dotted line), the reconstructed O/Cu(100) surface before (dashed line) and after the deposition of a 4.5 ML Ni film (solid line). The magnification at the L_3 edge points out the chemical shift of the reconstructed O/Cu(100) surface (inset) [5].

of Ni on clean Cu(100) and on O/Cu(100) from Refs. [5, 77]. The roughness of Ni on Cu(100) is effectively reduced in the entire thickness range by O surfactant. Part (b) of Fig. 4.2 shows the roughness of Ni grown on the less symmetric, more open Cu(110) surface which is discussed below.

X-ray absorption experiments on ferromagnetic films grown with O surfactant where first carried out in the Ni case [5]. The electronic structure of these samples was studied individually for each constituent element by the element-specific NEXAFS at the O *K* edge and the $L_{2,3}$ edges of Ni and Cu. In Fig. 4.3 (a) the NEXAFS at the O *K* edge is shown for three cases: (i) the reconstructed Cu(100) covered with 0.5 ML O (solid line), (ii) a 4.5 ML Ni film grown on the O-reconstructed Cu(100) surface (dashed line), and (iii) NiO/Cu(100) (dotted line) [5]. NEXAFS provides a sensitive fingerprint of the chemical bond and the local structure of the surface [43]. Therefore, it is concluded from the line shape of the spectra presented in Fig. 4.3 (a) that the Ni–O bond type in the surfactant grown samples is similar to the Cu–O bond type of the O-covered Cu crystal. The nature of this bond is clearly different from the one of NiO which explains the clearly different line shape. The edge jump ratio J_R is a sensitive measure of the number of atoms probed. It stays constant $J_R \approx 4$ % after 4.5 ML Ni have been evaporated onto the reconstructed O/Cu(100) surface, i.e. the O absorption is not damped by the

Ni. This is, besides the AES results, a further indication, that the O floats on top of the growing Ni film. Additional theoretical investigations in Ref. [5] support this hypothesis. Final evidence is given by angular-dependent NEXAFS measurements as they are discussed in the present thesis in Sec. 4.3. A reversible chemical shift at the Cu $L_{2,3}$ edges shown in Fig. 4.3 (b) proves that the O atoms detach from the Cu surface upon Ni deposition. A small shift in energy of $\Delta E \approx 0.15$ eV is observed comparing the $L_{2,3}$ edges of the clean Cu(100) crystal (dotted line) to the one reconstructed by O (dashed line). This shift disappears when Ni is evaporated on top (solid line). The reversing of the modifications induced by the O indicates that the Cu–O bonds break when Ni is deposited. The fact that no bulk-like NiO is formed becomes also clear from the line shape of the XAS at the Ni $L_{2,3}$ edges. Furthermore, a charge transfer from Ni to O is determined from an increase in the intensity at the Ni L_3 edge. This will be discussed in detail in Sec. 4.3 in comparison with the new results on Ni grown on the Cu(110) surface.

Surfactant activity of oxygen has also been studied on Ni on the more anisotropic Cu(110) surfaces [98]. On the more open and more reactive Cu(110) surface a three-dimensional (3D) growth of ferromagnetic Ni is observed by STM throughout the whole thickness range [98]. It has been suggested that, like on the Cu(100), also on the Cu(110) surface O acts as a surfactant and stays always on top when Ni is deposited. The symmetry of the LEED pattern taken after the Ni deposition does not change with respect to the (2×1) O/Cu(110) surface. This indicates that the unit cell on top of the Ni film still results from added Ni–O rows and the O is located at the surface. Hence, in the case of the open (110) surface the Ni metal surface keeps the O-induced reconstruction of the Cu substrate – unlike in the case of the more symmetric (100) surface.

The investigations of Ni on Cu(110) and the idea of using O as a surfactant in this case were inspired by the results for Co on this Cu(110) surface published before [106, 107]. It has been reported that O works excellent as a surfactant for Co on Cu(110). Without surfactant it always shows a 3D growth. Using O as a surfactant Co grows layer-by-layer with a flat surface [106, 107].

Structure and magnetism of Co on Cu(100) without surfactant is, like in the case of Ni/Cu(100), well studied, see e.g. [61, 102]. No reports in literature exist about Co on Cu(100) grown with O surfactant. This is most likely due to the fact that Co grows already quite flat and layer-by-layer on the Cu(100) surface [108]. Therefore, no advantage is expected from a structural point of view when using O as a surfactant.

However, the O surfactant may be used to tailor the magnetization by changing the surface anisotropy energy in the same manner as for Ni [6].

Finally, Fe/Cu(100) is the most complicated case of a 3d FM on Cu(100). Due to its lattice parameters Fe grows less well on Cu(100) than Ni or Co. In the first 4 layers it adapts the fcc structure of the Cu substrate and grows pseudomorphically in a tetragonally distorted layer structure. In the thickness range $4 - 10$ ML it undergoes a structural transition and relaxes to its own bulk crystal structure which is bcc [109, 110].

Talking about magnetism in ultrathin films one of the first investigated properties is often any type of thickness-dependent spin reorientation transition (SRT). Table 4.1 summarizes the direction of the easy axis of magnetization of various ferromagnetic systems on Cu substrates, with and without O surfactant at room temperature. In general, the SRT in ultrathin 3d FM films from in-plane to out-of-plane magnetization will occur at a lower thickness, if O is used as a surfactant. In some cases, e.g. Ni on Cu(110) the SRT has only been observed in presence of O surfactant [77, 113]. This change is attributed to a reduction of the magnetic surface anisotropy energy by the surfactant [4, 6]. Furthermore, for Ni/Cu(100) also a temperature-dependent change of the thickness at which the SRT occurs has been observed [62]. Even if Cu is evaporated on top of a surfactant-grown Ni film, the oxygen will keep its surfactant activity and float on top of the Cu cap. If the Ni film is covered with Cu, the SRT will happen at $d_{\mathrm{Ni}} = 6.5$ ML, no matter whether it has been grown with or without O surfactant [101]. With the knowledge of the easy axis, the magnetization of the films can easily been aligned parallel to the photon wave vector and the magnetic field in XMCD measurements. For all three elements Fe, Co, and Ni XAS and XMCD are well known in the clean case [23, 52, 120]. Bulk-like samples of them were grown on Cu(100) and investigated systematically at the UE56-PGM beamlines at BESSY [23]. Thus, they serve as references for the present investigations that are discussed in the following sections. Induced magnetism on light elements in contact with ferromagnets has been observed by XMCD for atomic oxygen on Co films [121] and molecular CO on Ni [122] and Co [123] films. In these cases the oxygen and CO, respectively, were adsorbed onto the surfaces after the FM films had been grown. Also at the carbon K edge of Fe/C multilayers [124] magnetic dichroism has been observed in reflectance. All these experiments show that XMCD technique provides the sensitivity to detect these small induced magnetic signals of small amounts of light elements.

Table 4.1: Overview of ultrathin $3d$ ferromagnets and their easy axes of magnetization with and without O surfactant. The direction of the easy magnetization axis at room temperature is given in the various ranges of the thickness d_{FM} of the ferromagnetic film as it is reported in the literature.

sample	d_{FM} (ML)	easy axis	references
Ni/Cu(100)	below $7 - 11$	in-plane parallel $\langle 110 \rangle$	[4, 101, 111, 112]
	$\gtrsim 7$	out-of-plane	[111, 112]
	$\gtrsim 9$	out-of-plane	[101]
	$\gtrsim 11$	out-of-plane	[4]
Ni/O/Cu(100)	$\lesssim 5$	in-plane	[4, 6]
	$\gtrsim 5$	out-of-plane	[4, 6]
Ni/Cu(110)	$10 - 30$	in-plane parallel $\langle 111 \rangle$	[113]
Ni/O/Cu(110)	$\lesssim 5$	in-plane parallel $\langle 110 \rangle$	this work *
	$7 - 35$	out-of-plane	[77, 114]
	≥ 35	slowly tilting back in-plane	[114]
Co/Cu(100)	$1.5 - 20$	in-plane parallel $\langle 110 \rangle$	[115, 116]
Co/O/Cu(100)		in-plane parallel $\langle 110 \rangle$	this work +
Co/Cu(110)	$11 - 30$	in-plane parallel $\langle 001 \rangle$	[117]
Co/O/Cu(110)	$\lesssim 30$	in-plane parallel $\langle 001 \rangle$	[117]
Fe/Cu(100)	< 4	out-of-plane	[109]
	$4 - 11$	helical	[118, 119]
	> 11	in-plane	[109]
Fe/O/Cu(100)	$\lesssim 4$	out-of-plane	this work ++

[*] The experiments of the present work suggest this easy axis: 4.5 ML show an XMCD signal in-plane parallel $\langle 110 \rangle$ smaller than the bulk one. No XMCD was observed in the $\langle 100 \rangle$ and the out-of-plane direction. A final prove, i.e. measurement of the full angular dependence, is missing.

[+] The results of the present work suggest that like in the case of Co/O/Cu(110) the easy axis is not changed by the O surfactant.

[++] At 5 ML no XMCD was observed out-of-plane or in-plane parallel $\langle 110 \rangle$. The vanishing magnetization in the entire thickness range of Fe on O/Cu(100) reported in [91] is due to the sample treatment (Cu-capping and *ex situ* measurements).

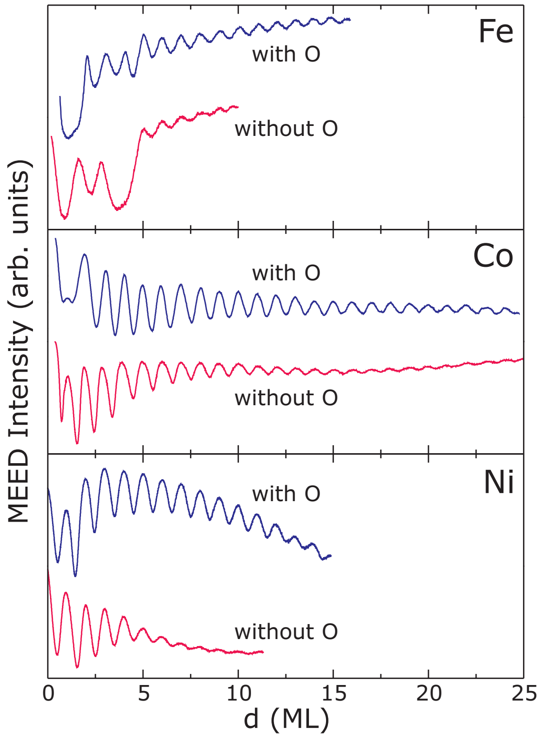

Figure 4.4: MEED oscillations of the $3d$ FMs Fe, Co, and Ni grown on Cu/(100) with and without O as a surfactant [125].

4.2 On the Growth and Structure

In principle, the growth and the structure of the $3d$ FMs Fe, Co, and Ni on Cu(100) single crystals can be considered known, as it is discussed in the previous section. Also the possibility of improving the growth mode toward a more layer-by-layer one by using O as a surfactant is established, except for Co/Cu(100) which grows layer-by-layer in a wide thickness range also without surfactant. However, in the present study MEED and LEED experiments were carried out to confirm the results reported in the literature for all investigated cases. Due to the *in situ* preparation of all the samples directly at the beamline, their growth could be monitored on-line by MEED. The MEED oscillations were as exemplarily shown in Fig. 4.4 for Fe, Co, and Ni, both with and without O surfactant. In each case the MEED of the thickest sample is given. The oscillations are quite pronounced when growing the films with the O surfactant up to a thickness of 15 ML in the case of Fe and Ni, and up to 25 ML in the case of Co. Growing the films without the surfactant, the MEED oscillations fade away at lower thickness, i.e. about 7 ML for Fe and Ni and about 17 ML for Co. The MEED intensity and the oscillatory amplitude disappear in the case of Fe/Cu(100) above 10 ML without surfactant when the films relax from the pseudomorphic fct structure to the natural bulk Fe structure which is bcc. Using O as a surfactant, this behavior is not found. This indicates that the surfactant helps Fe to stay in an fct structure above 10 ML [91, 126, 127]. In the clean films a

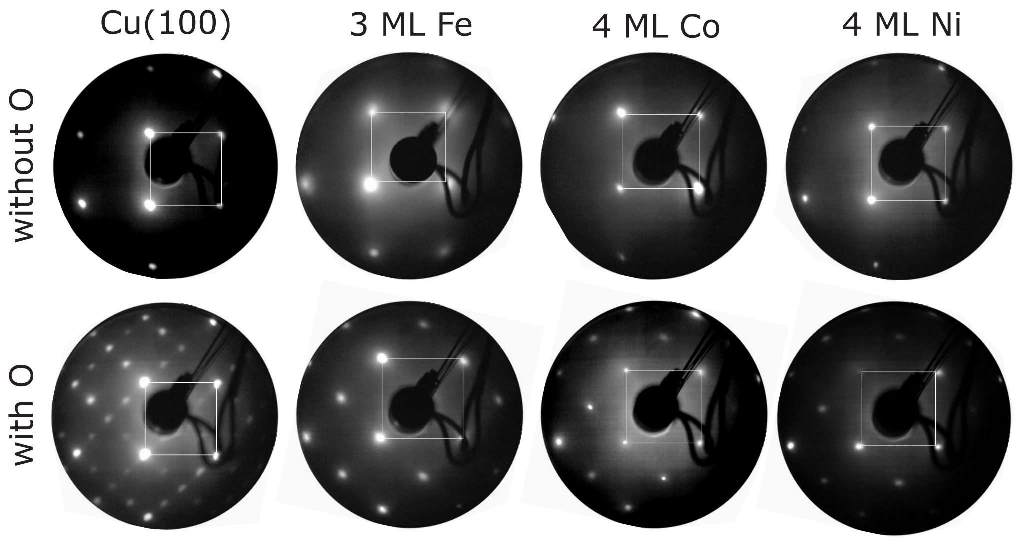

Figure 4.5: LEED patterns of $3d$ FMs with (lower row) and without (upper row) O as a surfactant. The white rectangles highlight the elementary cell of the pattern of the clean Cu crystal [125].

transition from fct to bcc occurs in the thickness range of $\sim 5 - 11$ ML [109, 110]. The MEED oscillations of clean Fe on Cu(100) only start to be regular above 4 ML which reflects the complex growth and structure of Fe below this limit reported in the literature [109, 110, 126, 127]. Various materials have proven to serve as surfactants and promote regular MEED oscillations from the beginning [126, 127]. In the case of Co a layer-by-layer growth on Cu(100) accompanied by regular MEED oscillations is known for a long time [108]. The growth of Co on Cu(100) with O surfactant has not been reported yet. The MEED oscillations in Fig. 4.4 suggest that also in this case the layer-by-layer growth starts from the second ML. Only the growth of Co on the more anisotropic Cu(110) surface where the O surfactant works highly efficient has been studied [106]. The results of the present MEED experiment of Ni/Cu(100) with and without O are identical to the earlier results [4].

The characterization of the samples by LEED is shown in Fig. 4.5. The white squares highlight the unit cell of the LEED pattern of the clean Cu(100) surface which is given on the left hand side of the top in Fig. 4.5. The upper row shows the LEED patterns of the $3d$ FM films Fe, Co, and Ni grown on the clean Cu(100) surface without O surfactant. The crystal is oriented such that the easy axes of the films is in the synchrotron plane for the measurements of the XAS and the XMCD. The LEED spots of 3 ML Fe, 4 ML Co, and 4 ML Ni appear at the same position as the ones of the clean Cu(100) crystal in a simple p(1×1) structure. Thus, they indicate that

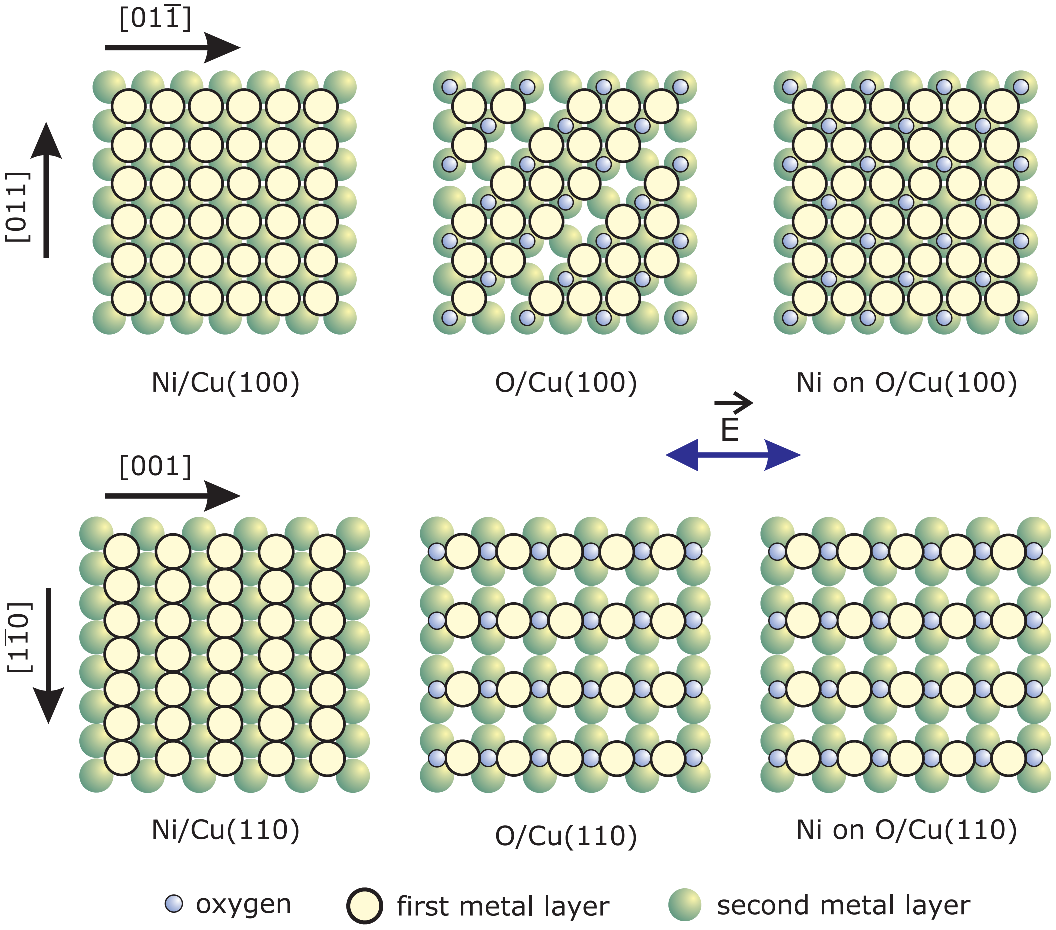

Figure 4.6: Schematic representation of the surfaces of the various samples: Ni/Cu(100) (top left), O/Cu(100) (top middle), Ni on O/Cu(100) (top right), Ni/Cu(110) (bottom left), O/Cu(110) (bottom middle), and Ni on O/Cu(110) (bottom right). The surfaces of the clean Cu(100) and Cu(110) crystals have the same structure as Ni/Cu(100) and Ni/Cu(110), respectively. The (2×1) reconstruction of O/Cu(100) exists in two domains, the missing rows appearing along the two equivalent directions rotated by 90° relative to each other. The sketch shows only one domain.
Small shaded circles: oxygen atoms, large open circles: atoms of the first metal layer, i.e. Ni and Cu, respectively, full circles: atoms of the second metal layer. The directions of the crystals and the electric field vector $\vec{E}$ are given according to the measuring geometry of the XAS and the XMCD.

all three elements grow pseudomorphically thereby adapting the fcc surface of the substrate crystal. In the upper row of Fig. 4.6 the corresponding hard sphere models in the case of Ni on the Cu(100) surface are shown. The directions of the crystals and the electric field vector $\vec{E}$ are given according to the measuring geometry of the XAS and the XMCD. In the lower row of LEED patterns in Fig. 4.5 on the left hand side, the pattern of the Cu(100) crystal after dosing 1200 L of O is shown. Various extra spots appear due to the O adsorption and the $\left(\sqrt{2} \times 2\sqrt{2}\right)$R45° reconstruction of the Cu surface. Besides, in the lower row in Fig. 4.5 the LEED patterns of the three elements Fe, Co, and Ni grown with O surfactant on Cu(100) are reproduced. They exhibit a c(2×2) superstructure. In accordance with the observations in the case of Ni [5] this indicates that the oxygen atoms are located in a fourfold hollow site with c(2×2) symmetry, as also illustrated in Fig. 4.6. Unlike on the surface of the Cu crystal after O adsorption, a reconstruction of the metal film surface does not occur when the O surfactant floats on top. Earlier works, e.g. by Thomassen *et al.* [109], report a (4×1) and (5×1) structures in the LEED patterns of Fe/Cu(100) in the thickness range below 5 ML. In the LEED pattern of clean Fe/Cu(100) in Fig. 4.5 these superstructures are not visible. This may be due to reasons given in a recent work by Bernhard *et al.* [128] who found that the reconstruction is not necessarily visible on very flat and clean substrates. As discussed in Chapter 3, the crystals used in the present experiment exhibit a mean terrace size of at least 100 nm. Hence, the crystal can be considered extremely flat within the probing area of the LEED. The lower row of hard sphere models in Fig. 4.6 represents the surfaces when Ni is grown on the anisotropic Cu(110) surface. In the clean case without O surfactant Ni adapts also here the fcc structure of the Cu substrate. There is no difference in the LEED patterns between the clean Cu(110) substrate and the Ni/Cu(110) film without O surfactant. When adsorbing O onto the Cu(110) surface a "missing row" reconstruction of the metal surface is formed which – unlike in the case of Cu(100) – does not disappear when the Ni is deposited. Thus, in this case the LEED spots of the Ni film grown with O surfactant appear at the same positions as for the O-covered Cu(110) crystal. (For the LEED patterns of the Cu(110) and the O/Cu(110) surfaces see Fig. 3.3.)

To determine the nearest neighbor distance R_{nn} of the O atoms to the Ni atoms of the topmost layer the surface extended X-ray absorption fine structure (SEXAFS) at the O K edge of 15 ML Ni grown with O surfactant on Cu(100) has been analyzed. The SEXAFS oscillations $k\chi(k)$ at room temperature and normal incidence of the X-rays are plotted in Fig. 4.7 (a). The SEXAFS is mainly determined by a single frequency corresponding to R_{nn}, which becomes clear from the Fourier transform $|\mathrm{FT}\,[k \cdot \chi(k)]|$

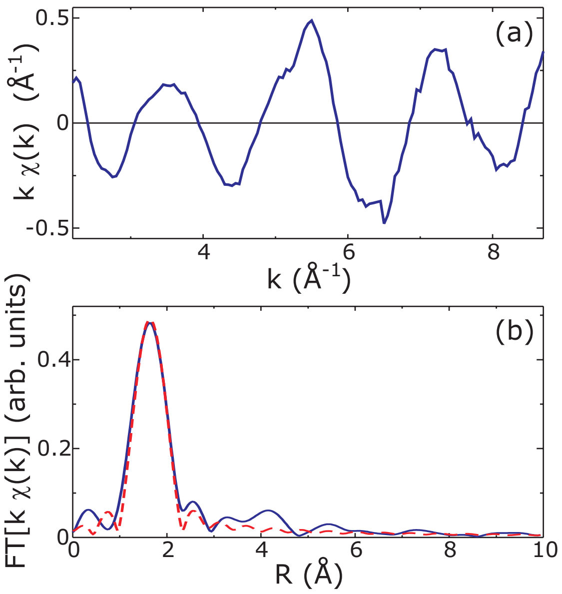

Figure 4.7:
(a) SEXAFS oscillations $k\chi(k)$ at room temperature and normal X-ray incidence and (b) the corresponding Fourier transform $|\mathrm{FT}\,[k\chi(k)]|$ of a 15 ML Ni film grown with O surfactant on Cu(100) as obtained from the experiment (solid line) and the fitting results of the nearest neighbor scattering shell (dashed line) [125].

of the experimental SEXAFS wiggles (solid line in Fig. 4.7 (b)). The nearest neighbor distance is determined by fitting the data (FEFFIT [129]) with a theoretical standard calculated with the FEFF8 code [130]. The dashed line in Fig. 4.7 (b) represents the FEFFIT result for the nearest neighbor scattering shell. From this fitting procedure a nearest neighbor O–Cu distance of $R_{nn} = (1.85 \pm 0.03)$ Å results. Assuming that the tetragonally distorted Ni film adopts the Cu in-plane lattice constant $a_{Cu} = 3.61$ Å, a height of $h = 0.41$ Å of the oxygen atoms above the first Ni layer follows from R_{nn}. These results agree well with the theoretically determined values of Ref. [5] and the ones recently calculated by R. Q. Wu [125]. The determination of the height of the oxygen atoms is crucial because it turns out that the calculated size of the magnetic moments of the Ni atoms on the surface as well as the one of the induced moment in the surfactant oxygen sensitively depend on h (see Sec. 4.6).

4.3 On the Electronic Structure

NEXAFS spectra were recorded at the O K edge and the $L_{2,3}$ edges of Fe, Co, and Ni, respectively to study the electronic structure of the surfactant grown samples. The angular dependence of the XAS at the O K edge provides clear evidence that the oxygen floats at the surface of the Ni film. Figure 4.8 shows this angular-dependent XAS of a bulk-like Ni film grown on the O/Cu(110) surface. These spectra were recorded with linearly polarized light ($\vec{E}$ vector perpendicular to the $[1\bar{1}0]$ direction, i.e. “along the Ni–O rows”) at an angle $\varphi = 90°$ (normal incidence, solid line) and $\varphi = 20°$ (grazing incidence, dashed line) between the incident X-rays and the surface

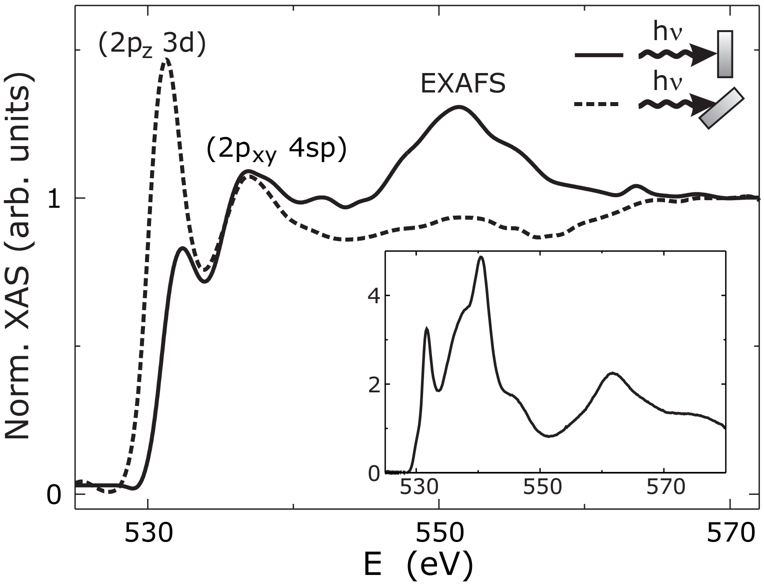

Figure 4.8: Angular-dependent XAS at the O K edge of a bulk-like Ni film on O/Cu(110) measured at an angle $\varphi = 90°$ (solid line) and $\varphi = 20°$, (dashed line) between the incident X-rays and the surface of the sample. The fine structures can be attributed to transitions into hybridized states as indicated. For comparison, the spectrum of NiO at the O K edge is included in the inset [99].

of the sample. Both spectra are normalized to the absorption spectra of a clean bulk-like Ni film measured at $\varphi = 90°$ and $\varphi = 20°$, respectively, to cancel out the background signal which arises due to O contamination of the various beamline components. Only if the O atoms are located at the surface and not embedded in the bulk of the sample, the XAS will show a strong angular dependence. If they were incorporated in the film, the angular dependence would be negligible because of the high symmetry.

As in the first studied case of Ni grown on O/Cu(100) discussed in Sec. 4.1 also in the case of Ni on the anisotropic O/Cu(110) surface the edge jump ratio at the O K edge stays constant when the film is deposited. This means that also in this case the oxygen coverage stays constant upon Ni deposition. The line shape of the XAS at the O K edge, as a fingerprint of the surface structure [43], reveals that the O surfactant and the topmost Ni layer on O/Cu(110) do not form bulk-like NiO. For comparison, a spectrum of NiO at the O K edge is included in the inset of Fig. 4.8. Experimental results together with theory have shown that atomic O $2p$ orbitals form hybrid orbitals with the Ni $3d$ and $4sp$ bands when atomic oxygen is adsorbed onto Ni single crystals [131–133]. The transitions from the initial O $1s$ states occur into hybridized (O $2p$–Ni $3d$) and (O $2p$–Ni $4sp$) final states [134]. NEXAFS probes the unoccupied density of states along the direction in which the $\vec{E}$ vector oscillates. The first feature located directly above the edge at ~ 530 eV is attributed to transitions into a hybridized state of O $2p_z$ and Ni $3d$ states. It is clearly pronounced in the grazing spectrum but rather weak in the spectrum recorded at normal incidence. This means that at the first peak of the O K edge spectrum is caused by unoccupied p states that are perpendicularly to the surface, i.e. O $2p_z$ states. The second feature of the O K edge spectrum has been assigned to transitions into (O $2p_{xy}$–Ni $4sp$) hybridized states [134]. Latest calculations of the band structure of Ni grown on Cu(100) with O surfactant by R. Q. Wu confirm that the second peak, located ~ 8 eV above the edge, is due to O p_{xy} states. It is strong only in the normal incidence geometry where $\Delta m = \pm 1$. For p_z states $m = 0$ and hence the p_z state does not respond to normal incident light with circular polarization. Details of the theoretical investigations are presented in Sec. 4.6. The third wiggle can be understood as a result from backscattering processes of the photoelectron. Measuring at normal incidence, the $\vec{E}$ vector is aligned parallel to the [001] direction, which is parallel to the O–Ni bond of the first layer. A large contribution of the backscattered photoelectron occurs in that direction. At grazing incidence the $\vec{E}$ vector is almost perpendicular to the film surface and the O–Ni

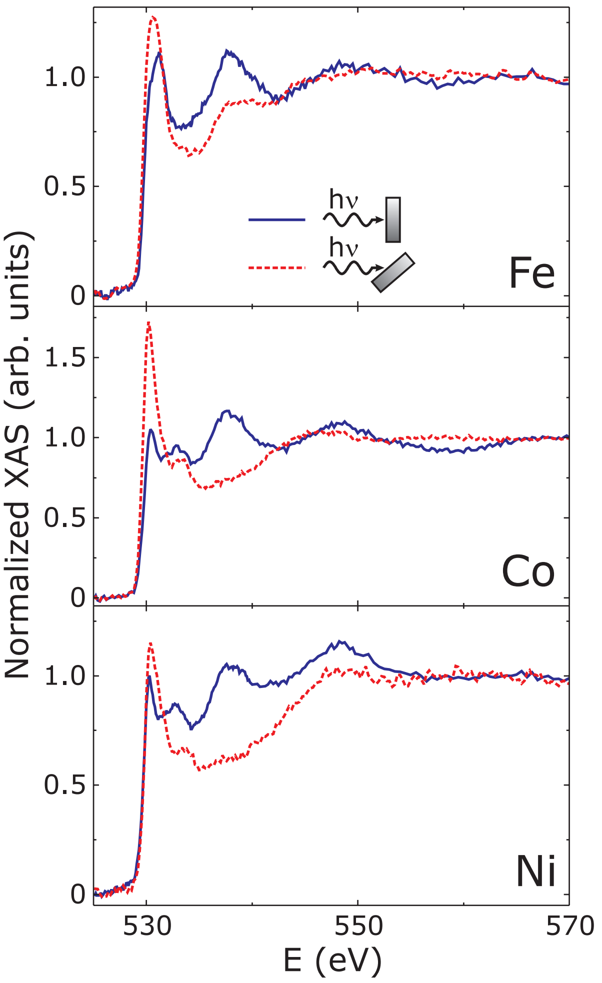

Figure 4.9: NEXAFS at the O K edge of the $3d$ ferromagnets grown on Cu(100) with oxygen as a surfactant at normal ($\varphi = 90°$, solid line) and grazing ($\varphi = 20°$, dashed line) incidence of the X-rays [125].

rows of the first layer. In that case, the effective coordination number is smaller and hardly any response from the scattered photoelectron is visible.

The systematic trends in the electronic structure across the series of the $3d$ FMs are evident from the angular-dependent NEXAFS of 3 ML Fe, 4 ML Co, and 15 ML Ni grown on Cu(100) with O surfactant (Fig. 4.9). The spectra are measured at normal ($\varphi = 90°$, solid line) and grazing ($\varphi = 20°$, dashed line) incidence of the X-rays. The NEXAFS of Co was recorded with linearly polarized X-rays, the $\vec{E}$ vector aligned perpendicular to the [011] direction. In the case of Ni and Fe the isotropic XAS which is the average of the XAS recorded with circular polarized light of the two helicities is shown. All spectra in Fig. 4.9 are normalized to the absorption of the clean Cu(100) substrate measured at $\varphi = 90°$ and $\varphi = 20°$, respectively. Their edge jumps are normalized to unity. The edge jump ratio is constant within the experimental error bar and amounts $J_R \approx 6$ %. The clear angular dependence of the spectra occurs for all the $3d$ films. Thus, the conclusions drawn therefrom in the case of Ni are valid also in the case of Fe and Co. (i) The oxygen atoms detach

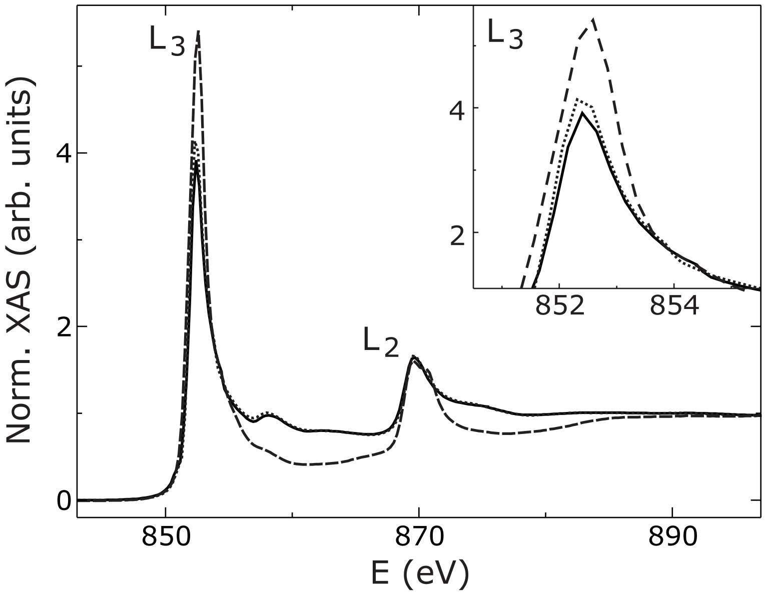

Figure 4.10: Normalized XAS at the Ni $L_{2,3}$ edges of 18 ML Ni/Cu(110) (solid line) and 6.5 ML (dotted line) Ni on O/Cu(110). For comparison, a spectrum of NiO is also included (dashed line). The inset shows the variation of the intensity of the spectra at the L_3 edge due to the charge transfer from Ni to O [99].

from the substrate crystal and float to the top of the film. (ii) No bulk-like oxide with the ferromagnet is formed since this would mean to incorporate the O into the film which would reduce the angular dependence. (iii) The spectral features and their angular dependence in the NEXAFS at the O K edge are very similar for all three FMs. Thus, the local structure and the local bonding of the surfactant oxygen atoms to the $3d$ FM atom are alike. The differences in the line shape between the spectra of the films on the two Cu surfaces especially at the second and third peak reflect the differences in the local structure of the O atoms on the two surfaces. This becomes clear from the hard sphere models of Fig. 4.6. On the Cu(110) surface the Ni–O bond is exactly parallel to the $\vec{E}$ vector whereas for the Cu(100) surface there is an angle of 45° between the $\vec{E}$ vector and the bond of the O and its nearest neighbor Ni atom.

Before turning to the magnetic properties of the surfactant grown $3d$ FMs in the next section, the properties of the electronic structure at the $L_{2,3}$ edges are to be discussed now. Figure 4.10 shows the normalized XAS of 6.5 ML epitaxially grown Ni on the (2×1) O/Cu(110) surface (dotted line) and 18 ML Ni on clean Cu(110) (solid line) in the energy range of the Ni $L_{2,3}$ edges. Additionally, a spectrum of NiO is included (dashed line). The intensity of the XAS at the Ni $L_{2,3}$ edges is increased in both the NiO and the Ni film grown on O/Cu(110). The inset shows this enhancement enlarged at the L_3 edge. The enhanced XAS intensity is caused by a charge transfer from Ni to O states, which results in an increase of the number of Ni d holes n_h ($n_h = 1.45$ per atom for Ni bulk [135]), because the transitions from initial $2p$ states at the Ni $L_{2,3}$ edges occur into unoccupied $3d$ states which NEXAFS probes. Two effects influence the white line intensity of the Ni XAS spectra of the surfactant grown films. (i) A charge transfer from Cu to Ni at the Ni/Cu interface leads to reduction of the XAS intensity of Ni on Cu substrates [135]. (ii) As discussed, an additional charge transfer occurs from the Ni film to the O surfactant. Since an increase of the white line intensity is observed, the charge transfer from Ni to O is larger than the one from Cu to Ni. Comparing the clean Ni films to the ones grown on the O-reconstructed Cu surface, the difference is to be attributed to the influence of the oxygen. The number of d holes per Ni atom n_h averaged over the entire Ni film is in good approximation proportional to the integral over the XAS [53, 135]. The the proportionality factor is obtained from the integral of the XAS of a bulk-like sample with known number of d holes. Integrating yields $n_h = 1.50(6)$ per atom for the 6.5 ML Ni film grown on O/Cu(110). The charge transfer from Ni to O is similar to the one observed in Ni films on O/Cu(100) where $n_h = 1.52(6)$ per atom for 4.5 ML Ni on O/Cu(100) was determined [5]. Furthermore, like at the O K edge, the line shape excludes the formation of bulk-like NiO. The intensity at the maxima of the Ni $L_{2,3}$ edges is significantly enhanced compared to the cases of clean and surfactant grown Ni films on Cu because in NiO the largest charge transfer from Ni to O occurs. In between the edges the absorption decreases down to the continuum background. The reason for this may be that the Ni d band is narrower in NiO than in Ni metal as it may be expected for the more localized $3d$ states of the ionic Ni–O bond in NiO.

4.4 On the Magnetism

Talking about magnetism of the surfactant grown Fe, Co, and Ni films on Cu(100) it is most evident to study the magnetism of the FMs themselves first. The present section deals with this topic. However, similar to O adsorbed onto a Co film [121] the oxygen atoms on the surfactant grown films may acquire an induced magnetic moment. The advantage in this case is that the $L_{2,3}$ edges of the $3d$ FMs as well as the O K edge are located in the soft X-ray regime. Hence, both the induced magnetism in the surfactant and the magnetic properties of the FM films can be probed in the same experiment as shown in Fig. 4.11 for the case of Co. The

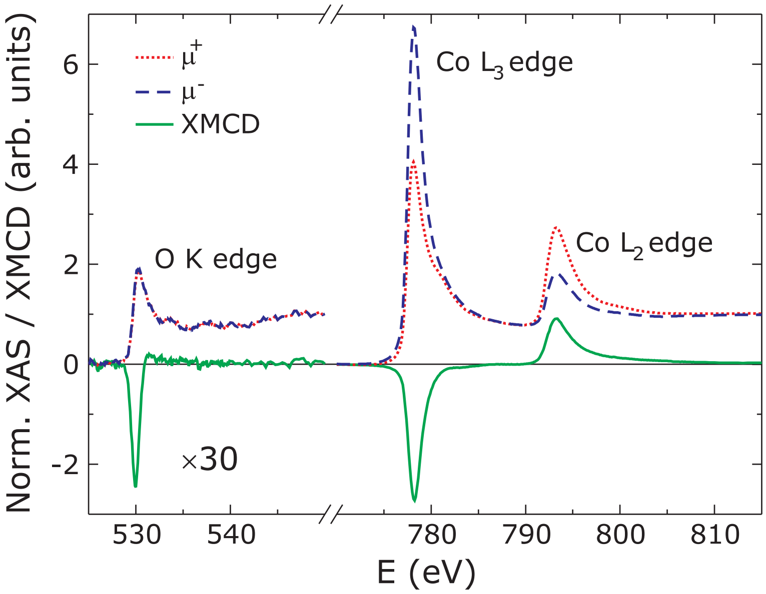

Figure 4.11: Normalized X-ray absorption coefficient and XMCD at the O K edge and Co $L_{2,3}$ edges of the surfactant grown Co film. The XMCD at the O K edge has been scaled by a factor of 30 for clear visibility [99].

absorption coefficient for left and right circular polarized light (dashed and dotted lines) and the XMCD (solid lines) at the O K edge and the Co $L_{2,3}$ edges are plotted. The XAS are normalized to unity at each edge. A clear XMCD signal is observed at the Co $L_{2,3}$ edges. At the O K edge a difference between the absorption coefficient for left and right circular polarized light can hardly be made out by eye. However, due to the sensitivity at the UE56-PGM beamlines also a tiny XMCD signal at the O K edge can be revealed after their subtraction (note the scaling factor for the O K edge XMCD). The appearance of this signal shows that indeed the Co film induces a magnetic moment in the surfactant oxygen. This induced magnetism at the O site is discussed in detail in the subsequent Sec. 4.5.

First, the case of Ni shall be discussed in detail as a function of the thickness of the films. The results obtained on the two surfaces, i.e. the highly symmetric Cu(100) and the more anisotropic and open Cu(110) surface are compared. The investigations are mainly restricted to a thickness range where the easy magnetization direction of Ni is perpendicular to the surface of the sample. The measurements were therefore carried out at normal incidence, because XMCD probes the projection of the magnetization onto the direction of the $\vec{k}$ vector of the incoming photons. In the rarely studied case of Ni on the Cu(110) surface the question of in-plane easy axis has not

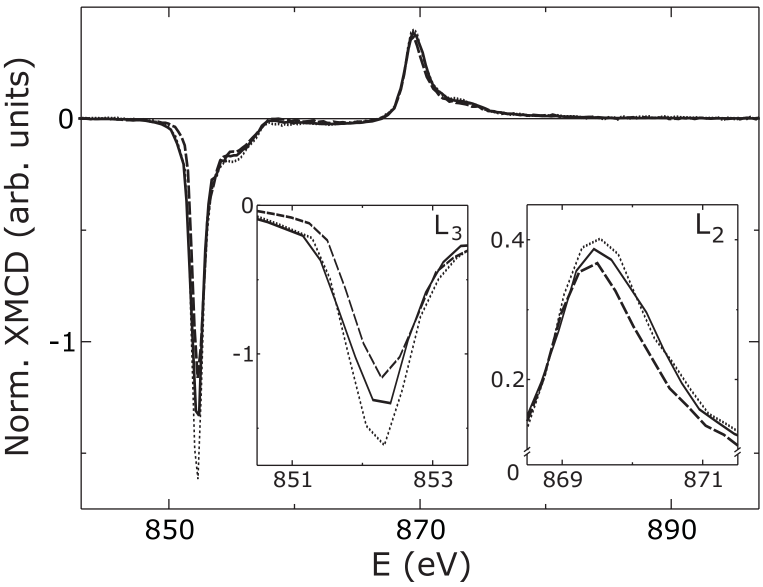

Figure 4.12: Normalized XMCD spectra at the Ni $L_{2,3}$ edges of 18 ML Ni/Cu(110) (solid line), 6.5 ML Ni on O/Cu(110) (dotted line), and 5.5 ML Ni on O/Cu(100) (dashed line) at $T = 30$ K. The inset shows the variation of the intensity of the spectra at the L_3 edge [99].

yet been finally clarified. Therefore, magnetic moments cannot be reliably deduced from XMCD measurements for in-plane magnetized samples.

In Fig. 4.12 the XMCD of thin Ni films grown with O surfactant slightly above the SRT, i.e. with easy axis perpendicular to the surface of the samples, are compared to clean bulk-like Ni (solid line). The most striking observation is the difference between the Ni films of the two different Cu substrate surfaces. The inset shows the variation of the intensity of the spectra at the L_3 edge. The XMCD signal of 5.5 ML Ni on O/Cu(100) (dashed line) is reduced compared to the thick Ni film. In contrast, on O/Cu(110) 6.5 ML Ni (dotted line) show an enhanced XMCD signal. 18 ML Ni/Cu(110) have been chosen as the example with bulk-like XMCD. The other investigated thick Ni films with and without O surfactant on the two Cu surfaces (12 ML clean Ni/Cu(100), 18 ML clean Ni/Cu(110), and 18 ML Ni on O/Cu(110) – not included in Fig. 4.12) do not show any significant differences in their XMCD spectra within 5 %. Hysteresis loops of perpendicularly magnetized Ni films grown with O surfactant taken by polar MOKE at room temperature show square-like shapes on both the Cu(110) surface (shown in Fig. 4.13) [77, 99] and the Cu(100) surface [4, 77]. The magnetic signal at remanence is the same as in saturation ensuring

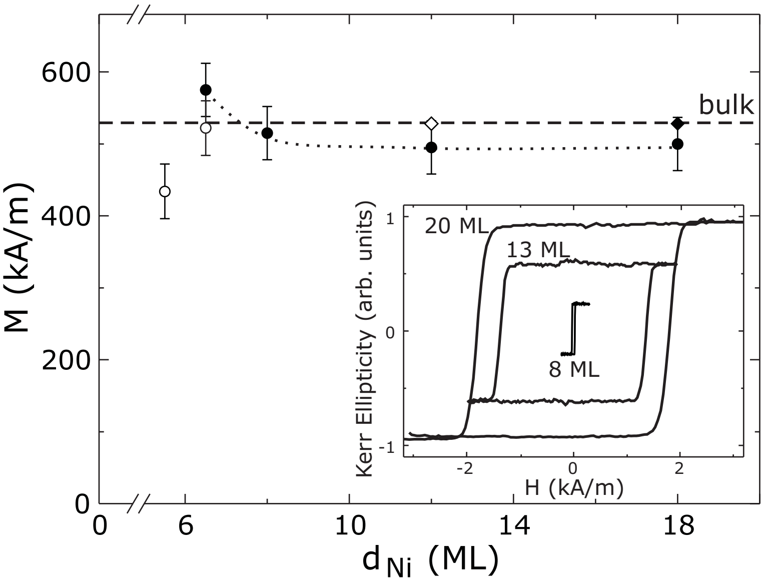

Figure 4.13: Magnetization as a function of the Ni film thickness obtained from the XMCD spectra for Ni on O/Cu(110) (solid circles) and Ni on O/Cu(100) (open circles) [99]. The magnetization of the reference sample (solid diamond for Ni/Cu(110), open diamond for Ni/Cu(100)) was fixed to the value for Ni bulk (marked by the dashed line) as described in the text. The inset shows square-like hysteresis loops of Ni on O/Cu(110) measured by polar MOKE at room temperature [77].

a single domain state of the films. The magnetization of films with out-of-plane magnetization can hence safely be transferred into magnetic moments.

As explained in Sec. 2.3, the magnetization of the Ni films is proportional to the ratio $\Delta A_3/A_3$ of the integrated areas at the Ni L_3 edge of the normalized XAS (A_3) and the XMCD spectra (ΔA_3). The proportionality factor is determined by calculating $\Delta A_3/A_3$ of 18 ML Ni grown on the clean Cu(110) and assuming a Ni bulk magnetization $M_{\mathrm{Ni}}^{\mathrm{bulk}} = 528$ kA/m. On the Cu(100) a 12 ML Ni film serves as the reference. The change of the number of Ni d holes n_h is also taken into account. Figure 4.13 shows the Ni magnetization as a function of the Ni thickness comparing the results on the two surfaces: Ni on O/Cu(110) (solid circles) and on O/Cu(100) (open circles). The magnetization values of the reference samples are included as diamonds (solid for Ni on Cu(110), open for Ni on Cu(100)). The discussion will be started with the more studied Cu(100) surface. Down to 6.5 ML Ni on O/Cu(100) the magnetization does not change within the error bar and remains at the bulk value. As may already be observed at first glance in the XMCD spectra, the magnetization decreases below 6.5 ML. Compared to the bulk, the Ni magnetization is reduced by $\sim 18\%$ for 5.5 ML Ni on O/Cu(100). Assuming the magnetic moments for inner Ni layers ($m_{\mathrm{Ni}}^{\mathrm{bulk}} = 0.61\mu_{\mathrm{B}}$) and the Ni-Cu interface ($m_{\mathrm{Ni}}^{\mathrm{interface}} = 0.31\mu_{\mathrm{B}}$) [56], one may estimate the reduction to be in the order of up to $\sim 50\%$ for the magnetic moment in the surface layer of the 5.5 ML sample. It is known that the magnetic moment of Ni at an interface to Cu is reduced [56, 65]. Looking at the surface layer of clean Ni/Cu(100) facing vacuum an increased magnetic moment is observed. No change in the total magnetization results for thin films of Ni/Cu(100) compared to bulk Ni, because the reduction at the interface is compensated by the enhancement at the surface [56]. Here in the case of surfactant grown films, 5.5 ML Ni on O/Cu(100) show a reduction of the magnetization signal compared to bulk Ni. This means effectively that the O surfactant lowers the surface magnetic moment. In the case of Ni films on the reconstructed O/Cu(110) just the opposite compared to Ni on O/Cu(100) is found: the total magnetization increases with decreasing Ni thickness. The magnetization of 6.5 ML Ni on O/Cu(110) is approximately 9% larger than the bulk value, although a reduction of similar size as on Cu(100) is also expected for the Ni moment at an interface to Cu(110) [65]. This means that Ni films on O/Cu(110) show an enhanced surface magnetization. The magnetic moment of the surface layer is estimated at $m_{\mathrm{Ni}}^{\mathrm{surf}} \approx 0.9\ \mu_{\mathrm{B}}$, which is $\sim 48\%$ larger than Ni bulk. Assuming that O has a similar influence on the Ni magnetization on the two surfaces, an additional mechanism is needed that leads to the observed enhancement on O/Cu(110). The main difference observed in the STM experiments between Ni films on the two surfaces is their roughness, in particular at 6–8 ML. As summarized in Sec. 4.1, Ni films grow layer-by-layer on the O/Cu(100) throughout the entire thickness range whereas for the Ni on O/Cu(110) the roughness shows a local maximum at 6–8 ML (Fig. 4.2). Several works have reported similar correlations between surface roughness and magnetic properties, e.g. magnetic surface anisotropy, giant magnetoresistance, and coercive field [136–139].

A full detailed sum rule analysis elucidates the magnetic moments of the investigated Ni films. For Ni the sum rules have proven to be applicable. The complete procedure with its limitations is discussed in Sec. 2.3. First of all, the ratio m_L/m_S^{eff} is considered. Here, the contribution of the magnetic dipole term $\langle T_z \rangle$ contained in the spin sum rule is not separated. Only an effective spin moment is obtained. In Table 4.2 the values m_L/m_S^{eff} of Ni films on the two Cu surfaces are given. In the considered thickness range the ratio stays constant for Ni on O/Cu(100). This agrees with investigations of Ni films on Co/Cu(100) where an increase of the ratio is observed only at a Ni thickness lower than 2 ML [53]. The authors of Ref. [53] find $m_L/m_S^{\mathrm{eff}} = 0.12$ for a 10 ML Ni film. In general, the tetragonal distortion of ultrathin

Table 4.2: Orbital moment per effective spin moment m_L/m_S^{eff} of Ni on O/Cu(110) and on O/Cu(100) obtained from the XMCD spectra [99].

d_{Ni} (ML)	m_L/m_S^{eff}	
	O/Cu(110)	O/Cu(100)
18	0.12(2)	–
18	0.15(3)*	–
12	0.11(1)	0.14(3)*
8	0.14(2)	–
6.5	0.17(3)	0.13(2)
5.5	–	0.14(2)

* Ni on clean Cu

Ni films leads to a slightly higher ratio than in Ni bulk where $m_L/m_S^{\text{eff}} = 0.10$. In contrast, for Ni on O/Cu(110) an enhancement of the ratio can be made out going to thinner Ni films. Like the magnetization, the ratio is increased in the same thickness range where the larger roughness of the Ni films on O/Cu(110) is observed.

To finally reveal the origin of the observed enhancement of the magnetization and the ratio of thin Ni films on O/Cu(110) in contrast to thin Ni films on O/Cu(100), the contributions of spin and orbital moment are deconvoluted. Figure 4.14 shows the effective spin moment m_S^{eff} (solid circles) and the orbital moment m_L (open circles) of the investigated films as a function of the Ni thickness. They are given relative to spin and orbital moment of the clean Ni references on the two Cu surfaces. This relative representation especially points out the changes of the values for the thin films in comparison to the bulk values. On the O/Cu(100) surface both the spin and the orbital moment of Ni films become smaller when their thickness is reduced. The relative change of spin and orbital moment is identical and their relative contribution to the total magnetization does not change. On the other hand, on O/Cu(110) a large relative increase of the orbital moment is observed for thinner Ni films whereas the spin moment stays more or less constant within the error. The error is estimated from variation of the results when varying the integration range. The definition of the integration range yields the largest contribution to the experimental error bar. The increase of the magnetization of ultrathin Ni films on O/Cu(110) stems mainly from a raised orbital moment at the surface of these films. Even if the spin takes up some of the enhancement, which is possible within the estimated error, the orbital

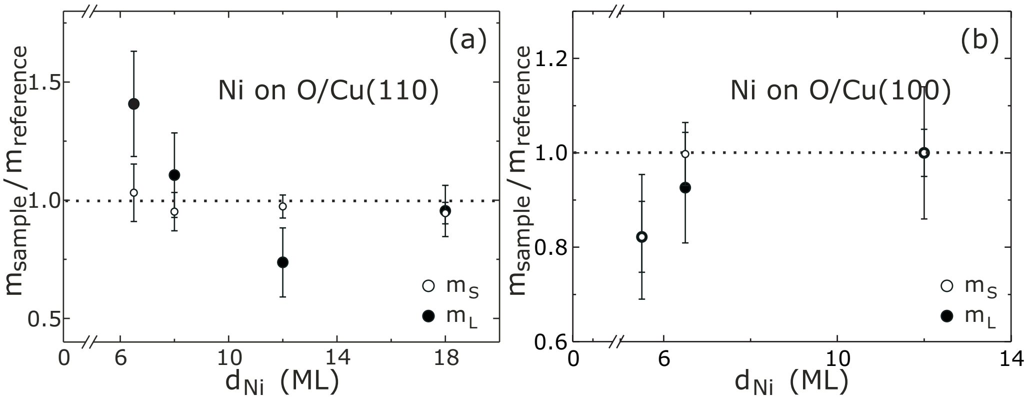

Figure 4.14: Orbital (solid circles) and effective spin (open circles) moment of Ni on the O reconstructed substrate relative to spin and orbital moment of bulk-like Ni on the clean Cu substrate [99]. (a) Ni on O/Cu(110), reference: 18 ML Ni/Cu(110), (b) Ni on O/Cu(100), reference: 12 ML Ni/Cu(100).

moment must take up around 50 % of the total enhancement. This is quite a lot considering that the orbital moment is only 10−15 % of the spin moment. In general, a reduced coordination number leads to an unquenching of the orbital moment. At the rougher surface, the coordination of the surface atoms is reduced compared to a flat film. Hence, the increase of the orbital moment may be attributed to the rougher growth of these films.

Summarizing, the influence of O surfactant growth on the magnetic properties of a ferromagnetic film has been evidenced by XMCD measurements using Ni on Cu substrates as an example. Especially, spin and orbital contributions have been separated by applying the integral sum rules. In the following section the focus is turned to the magnetic properties of the surfactant O itself.

4.5 Induced Magnetism at the O Site

It was shown by investigation of the XMCD at the O *K* edge in the group of T. Ohta that a magnetic moment will be induced in 0.5 ML oxygen if adsorbed onto a ferromagnetic Co film [121]. The sensitivity of the XMCD technique is sufficiently good to detect the XMCD signal that occurs due to the induced orbital moment in 0.5 ML oxygen. At the beginning of the preceding section it is already mentioned that the same observation of induced magnetism at the O site can be made in Co films grown with O surfactant on Cu(100) (Fig. 4.11). When adsorbing oxygen onto

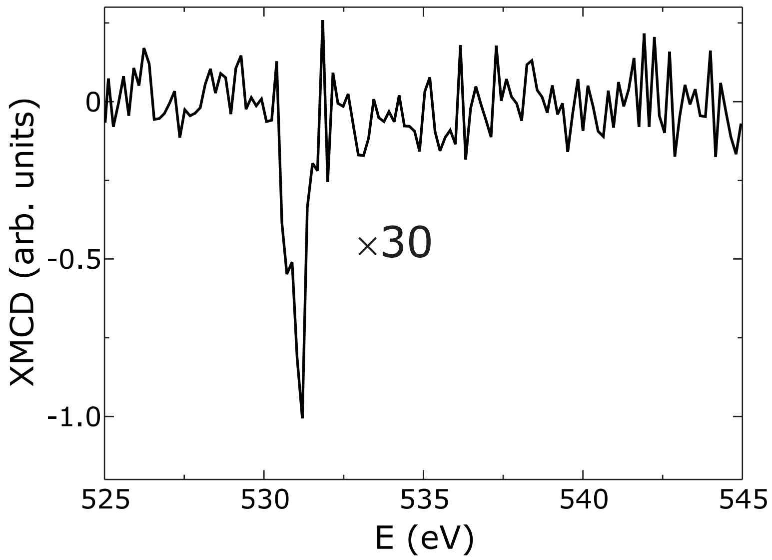

Figure 4.15: Dichroic signal at the O K edge of bulk-like Ni on O/Cu(110). The scaling factor is given with respect to the edge jump normalized to unity [99].

a Cu(100) or a Cu(110) single crystal to form the $\left(\sqrt{2} \times 2\sqrt{2}\right)$R45° reconstruction or the (2×1) reconstruction, respectively, as described in Sec. 3.2, the amount of O corresponds to 0.5 ML. In the present work the induced magnetic moment due to the hybridization of O $2p$ states with the $3d$ states of the FM was first investigated in the case of a bulk-like Ni film on O/Cu(110) [99]. Figure 4.15 shows the XMCD signal at the O K edge. The scaling factor is given with respect to the edge jump at the O K edge which has been normalized to unity. At the K edge transitions occur from $1s$ initial states to $2p$ final states. Thus, the initial states are not spin-orbit split and XMCD at the K edge provides only information on the *orbital* moment. At the same energy where transitions to $(2p_z3d)$ states are identified, a dichroic signal can be detected. Apart from that, no other significant features are observed in the spectrum. From the negative sign of the signal it can be concluded that the orbital moment of the oxygen is aligned parallel to spin and orbital moments of the nickel. In principle, XMCD spectra at K edges can be analyzed with the help of the orbital sum rule [47, 48] to determine the size of the orbital moment. However, in the present cases mainly two reasons make the application questionable. (i) The number of $2p$ holes is ill-defined. The integral of the calculated DOS given below in Fig. 4.18 grows monotonically with energy and does not saturate. Any integration cut-off will be arbitrary. (ii) It is not clear how to subtract the transitions into the continuum. The general procedure of applying a step function like at the $L_{2,3}$ edges of the $3d$ FMs fails in the following sense: Only by setting the step edge several

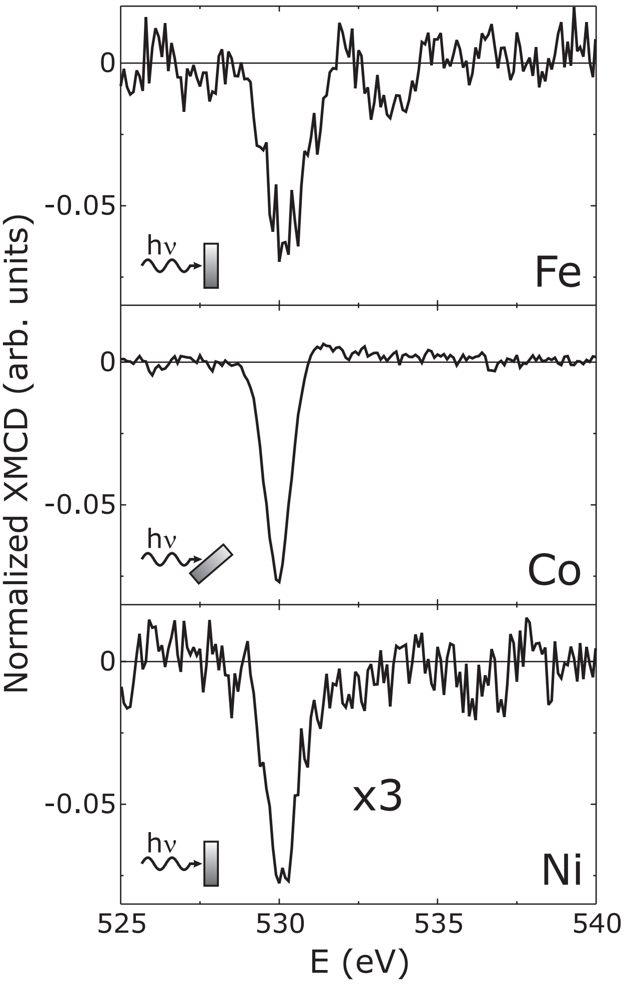

Figure 4.16: XMCD at the O K edge of the $3d$ ferromagnets grown on Cu(100) with oxygen as a surfactant [125].

eV above the O K edge and by assuming a very broad step it is possible to avoid apparent negative contributions, which of course would be nonphysical. Thereby the determination of the integrated area becomes arbitrary.

The orientation of the spin moments of Ni and O is not straightforward evident. It cannot be directly compared to the situation of NiO, where one usually discusses the antiparallel orientation of the Ni spins to each other in terms of superexchange. Since there is no experimental access to the O spin moment the question whether the coupling of the Ni and O spin moments is ferromagnetic or antiferromagnetic cannot be answered from the experiment. Theoretical investigations of spin-resolved density of states predict a parallel alignment of the induced O spin moment to the Ni spin moment [6]. Concluding, the situation of the O as a surfactant for Ni on Cu(100) is similar to O adsorbed on ultrathin Co films [121]. The sign and the order of magnitude of the XMCD signal at the O K edge are the same in both cases.

To study the systematics of the induced magnetism a the O site, films of all three FM $3d$ elements have been grown on Cu(100) with the help of O surfactant. The thickness has been chosen such that all films are FM at room temperature. Thus, investigations at low temperature are not necessary to detect the induced magnetism. The XMCD signal of the induced moment is very small, only about 8 percent normalized to the oxygen edge jump ($J_r \approx 6\%$). Any additional noise as it may occur at low temperatures, e.g. caused by vibrations due to the flowing liquid helium, has to be avoided. The measurements remain, however, quite demanding for the setup of the beamline. Various pairs of the two directions of the magnetization are measured at positive and negative helicity. At least four good ones of them are averaged in each case.

In Fig. 4.16 the XMCD signals at the O K edge of all three elements Fe, Co, and Ni are plotted. The XMCD at the O K edge is much sharper (about 1 eV FWHM) compared to the XMCD at the $L_{2,3}$ edges of the FMs. In all three cases it is located at 530 eV, i.e. the energy where the NEXAFS shows a sharp structure that originates from hybridized $2p_z3d$ states. This indicates that only the O $2p_z$ orbitals are polarized which hybridize with the $3d$ band of the FM. Furthermore, the excellent statistics even allows for the identification of a small asymmetry in the O XMCD, the small positive contribution located at about 532 eV. The main contribution is negative in all three cases revealing that the induced orbital moment is aligned parallel to the spin and orbital moments of the ferromagnetic films. At 538 eV, no XMCD signal is detected. The conclusion of this is that the O p_{xy} states are not magnetically polarized, only the O $2p_z$ states.

The XMCD signal at the O K edge is largest in the case of Co and smallest in the case of Ni. To explain this finding two effects have to be taken into account. (i) One may expect that the magnetic moment of the FM film determines the size of the induced moment and thus the size of the XMCD signal at the O K edge. That would mean that Fe (total bulk magnetic moment: $m_{\mathrm{tot}}^{\mathrm{bulk}} = 2.1\ \mu_{\mathrm{B}}/\mathrm{atom}$) induces the largest signal, followed by Co ($m_{\mathrm{tot}} = 1.6\mu_{\mathrm{B}}/\mathrm{atom}$) and Ni ($m_{\mathrm{tot}}^{\mathrm{bulk}} = 0.6\mu_{\mathrm{B}}/\mathrm{atom}$). (ii) Only the O $2p_z$ orbitals are polarized which are probed stronger at grazing X-ray incidence (see Fig. 4.9). Since the Co film is magnetized in the film plane, the sample is measured at grazing incidence and therefore the largest O K edge XMCD is determined for this case, followed by Fe and Ni (please note the enlargement factor for Ni), which are measured at normal X-ray incidence. The line shape of the O K edge XMCD spectra is similar in all three cases. It compares well to the ones reported in literature at the O K edge for atomic oxygen adsorbed on Co films [121] and molecular CO on Ni [122] and Co [123] films. Furthermore, similarly sharp dichroic features are detected in reflectance at the carbon K edge of Fe/C multilayers [124].

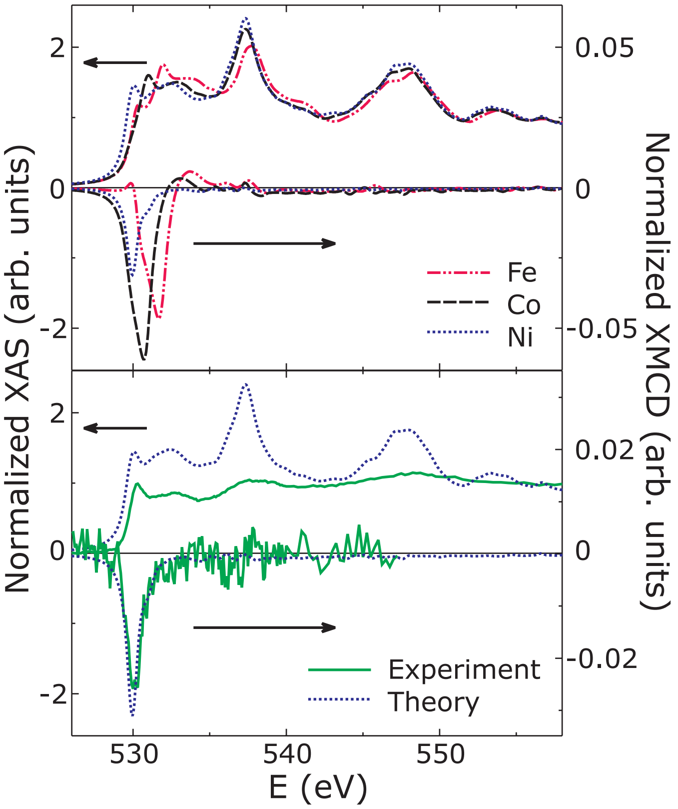

Figure 4.17: Top: Calculated XAS and XMCD at the O *K* edge of the O surfactant on the fcc Fe(100) (dash-2-dotted line), Co(100) (dashed line), and Ni(100) (dotted line) surfaces. Bottom: Comparison of measured (solid line) and calculated (dotted line) XAS and XMCD of the O surfactant on the Ni(100) film. Note that there is no scaling factor between experiment and calculation. The scale of the XAS is given on the left hand side, the one of the XMCD on the right hand side [125].

4.6 Comparison to Theory

The accompanying theoretical investigations have been carried out by R. Q. Wu, at the University of California in Irvine, USA. Density functional calculations for O adsorption on fcc Fe(100), Co(100), and Ni(100) surfaces have been conducted using the "thin-film full potential linearized augmented plane wave" (FLAPW) method [140, 141]. To account for the geometry of the samples, a c(2×2) oxygen layer is placed on top of a 7-layer slab of 3*d* atoms. The lattice parameter in the lateral plane is fixed to the one of bulk Cu (a = 3.61 Å). The vertical positions of all the atoms are optimized in an energy minimization procedure guided by the atomic forces calculated from first principles. Both the local density approximation (LDA) [142] and the generalized gradient approximation (GGA) [143, 144] are adopted to describe the exchange correlation interaction. The LDA calculations yield an optimized distance between the oxygen atom and its nearest Fe, Co, and Ni neighbor, respectively, of $R_{nn} = (1.85 - 1.86)$ Å depending on the 3*d* element. A distance of $R_{nn} = 1.93$Å results from GGA calculations. The LDA result agrees well with the experimentally determined value from the SEXAFS data in Sec. 4.2. Thus, the NEXAFS and XMCD spectra are calculated with LDA. In general, LDA yields better results for oxides, whereas GGA is the method of choice for metals. A priori

Table 4.3: Calculated spin magnetic moments and orbital magnetic moments induced in the oxygen in $3d$ FM films grown with O surfactant.

	m_S (μ_B/atom)	m_L (μ_B/atom)
Fe	0.053	0.0024
Co	0.132	0.0047
Ni	0.053	0.0021

it is not clear which of the methods is suited best in the present case where a metal is in contact with an oxide-like surface. Considering the NEXAFS results excluding the formation of bulk-like oxides at the surface, one might expect that GGA fits better. For that reason GGA was chosen in the earlier calculations of Ref. [6], when the SEXAFS results presented in Fig. 4.7 had not been know yet. It is known that GGA overestimates lattice sizes of oxides. The calculations here of O on $3d$ FMs reveal that it also does so on a surface in this case. The positions of the FM $3d$ atoms are nevertheless optimized with GGA, because for them the gradient corrections are crucial. In presence of O some displacement of the atoms in the subsurface layer occurs. For example, the subsurface Fe atom right beneath the O adatom goes inwards by 0.08 Å in O/Fe(100), whereas the other Fe atoms remain at their bulk positions. The interlayer distance between adjacent $3d$ layers is, depending on the element, (1.73 – 1.75) Å in agreement with $I(V)$-LEED results [77].

The top panel of Fig. 4.17 shows the calculated XAS and XMCD spectra. In the calculations only dipole transitions are treated. The spectra are convoluted by Doniach-Sunjic shapes of 0.45 eV width for lifetime broadening [145], and the theoretical spectra are shifted by 25 eV in energy to accommodate the core hole relaxation effect. The bottom panel of Fig. 4.17 presents the experimental data for Ni grown on O/Cu(100) together with the theoretical results. All spectroscopic features, i.e. the peak structures and the ratio between XAS and XMCD are well reproduced. Note also that there is no scaling factor between experiment and calculation. This indicates that the model used in the calculations represents the atomic arrangements in experimental samples very well.

The calculated spin and orbital moments projected into the O muffin-tin sphere are summarized in Table 4.3. The O atoms also influence the magnetization of the surface $3d$ atoms. The spin magnetic moment of a surface Ni atom is $m_\mathrm{Ni}^\mathrm{surf} = 0.26\ \mu_\mathrm{B}$, less than half of the one of an interior Ni atom with $m_\mathrm{Ni}^\mathrm{inner} = (0.66 - 0.69)\ \mu_\mathrm{B}$. These

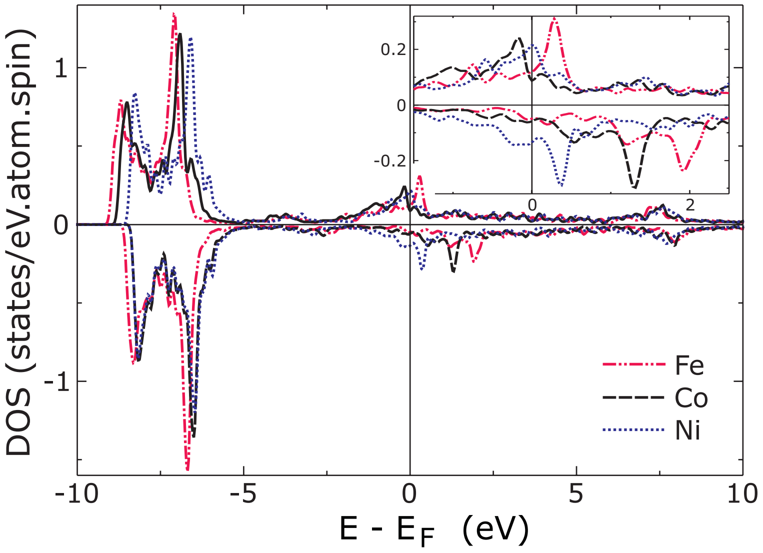

Figure 4.18: Calculated density of O p states. Positive and negative values represent states in the majority and minority spin channels, respectively. The energy E is given relative to the energy E_F of the Fermi level. The inset shows the region close to E_F [125].

values compare with the ones of a Ni/Cu interface where $m_{\mathrm{Ni}}^{\mathrm{interface}} = 0.31\mu_{\mathrm{B}}$ and $m_{\mathrm{Ni}}^{\mathrm{inner}} = 0.61\ \mu_{\mathrm{B}}$ have been determined experimentally [56]. Due to the fact that in an earlier publication [6] only GGA calculations were carried out, the values of the magnetic moments here differ from the ones reported earlier. In fact, the magnetic moments and the XMCD spectra depend sensitively on the height of oxygen atom on the substrates. When the GGA structure ($h = 0.68$ Å) is adopted, for example, the spin and orbital magnetic moments of O in O/Ni(100) are $0.17\mu_{\mathrm{B}}$ and $0.0025\mu_{\mathrm{B}}$, respectively. Consequently, the XMCD peak is larger than that shown in Fig. 4.17. The agreement of the calculated XMCD and the measured one reveals that indeed the LDA result of $R_{nn} = (1.85 - 1.86)$ Å for the O–3d bond length should be considered to be the better one. Furthermore, the core hole relaxation does not significantly affect the profile of the XAS and the XMCD [146].

Although the induced spin and orbital magnetic moments of O are small, the XMCD is sizable for all three systems. When comparing the energy position of the XMCD to the plot of the density of states (DOS) with O–2p features shown in Fig. 4.18, it becomes evident that these XMCD peaks stem from the substrate induced states right above the Fermi level. These states show a strong spin polarization and have an imbalance in the $m = 1$ and $m = -1$ compositions of their wave functions. This is mainly because of the large spin-orbit coupling inherited from the substrate atoms. In the calculation the position of these states shift to the higher energy side in a sequence as O/Ni(100), O/Co(100), and O/Fe(100). In the experiment this shift is hardly visible (see e.g. the difference between data for O/Fe(100) and O/Ni(100)). The two other main peaks in Fig. 4.18, $(7-8)$ eV and $(17-19)$ eV above E_f, show a very small exchange splitting and a weak resonance with the substrate states. Subsequently, they are only visible in the XAS but not in XMCD. Finally, the calculations confirm that the states $7-8$ eV above the Fermi energy are $p_{x,y}$ features, as deduced from the dependence of their intensity on the angle of incidence. Concluding, the calculations reproduce the measured spectra quite well. Thus, the theoretical results confirm and complement the experimental findings by providing, for instance, the magnetic moments.

Chapter 5

Importance of Enhanced Spin Fluctuations in Two-Dimensional Co/Cu/Ni Trilayers

Magnetic multilayers have become important for current research since they show a large number of magnetic effects that are not present in bulk material. Their relevance for technological applications due to their magnetic properties is nowadays well accepted (see e.g. Ref. [147]). In the present chapter, two effects in magnetic multilayers – spin fluctuations and the interlayer exchange coupling (IEC) – are discussed from a fundamental point of view. The main question is what happens when the two are considered simultaneously in the limit of 2D layers.

Coupled Co/Cu/Ni trilayers on a Cu(100) single crystal are used as a prototype system. The element specificity of the XMCD technique is especially valuable for the investigation of the trilayers because it reveals the magnetic behavior of each ferromagnetic constituent individually. It is demonstrated how to take advantage of XMCD to study temperature-dependent magnetization curves and thereby the Curie temperature. Moreover, due to the *in situ* preparation and measurement under UHV conditions it is possible to investigate the identical Ni film both with and without IEC. For this purpose, a Ni film capped with a Cu layer of the desired thickness is prepared and characterized first. Then, the Co film is deposited on top. Now the Ni film can be reinvestigated under the influence of the IEC with strength J_{inter}. Four characteristic temperatures are identified: the Curie temperature of the single Ni film $T_{\mathrm{C,Ni}}$, the Curie temperature of the single Co film $T_{\mathrm{C,Co}}$, and the two temperatures at which the individual Ni and Co magnetizations in the trilayer vanish, $T^{*}_{\mathrm{C,Ni}}$ and $T^{*}_{\mathrm{C,Co}}$, respectively. The temperature $T^{*}_{\mathrm{C,Ni}}$ of the Ni film in the trilayer is considerably larger by $\Delta T_{\mathrm{C,Ni}}$ than $T_{\mathrm{C,Ni}}$ of a single Ni film with the same thickness. In general, the IEC influences also the Co film. However, since the Co is much stronger than the Ni, the influence of the Ni on the Co is small. The Ni layer is much more suitable to observe the effect, also because its Curie temperature is easily tunable in a wide and convenient temperature regime up to room temperature. Thus, the technique gives unique insight in how each ferromagnetic (FM) layer contributes to the global behavior of the trilayer system. The experimental results together with a theoretical model contribute to the understanding of the interplay between spin fluctuations and IEC in magnetic multilayers.

The chapter starts with a detailed description of the motivation for the new investigations of the two-dimensional (2D) magnetic Co/Cu/Ni trilayers. A short summary of related research follows. Since a considerable number of publications by the group about the X-ray experiments previously carried out on coupled trilayers and IEC exists, a review of them is given separately in Sec. 5.3. Then, the new improved experiments and how they complement the earlier findings is explained in Sec. 5.4. The experimental results are analyzed within the theoretical model introduced in Sec. 2.4. Section 5.5 describes the determination of some model parameters from experimental observations. This completes the theoretical model such that the desired combination of two well-known effects, i.e. the oscillatory IEC as a function of the Cu-spacer thickness d_{Cu} and the 2D character of the magnetization as a function of the Ni thickness d_{Ni}, become possible. The summary of all, i.e. the full dependence $\Delta T_{\mathrm{C,Ni}}/T_{\mathrm{C,Ni}}$ as a function of *both* d_{Ni} *and* d_{Cu} is presented in a comprehensive two-parameter plot in Sec. 5.6. This combination is only possible after deducing the shift $\Delta T_{\mathrm{C,Ni}}/T_{\mathrm{C,Ni}}$ as a function of the coupling strength J_{inter} which – in contrast to earlier findings in a mean field (MF) description – turns out to be nonlinear.

5.1 Motivation

In general, coupled trilayers consist of two ferromagnetic layers (FM1 and FM2) and a nonmagnetic spacer (NM) in-between. They are the simplest type of multilayer which exhibits an indirect coupling via a nonmagnetic spacer layer. The two effects of spin fluctuations and IEC compete with each other and may dramatically influence the critical behavior of the trilayers. Fig. 5.1 illustrates the situation schematically. The strong interrelation of spin fluctuations and IEC is in particular interesting in the 2D limits of the thickness of FM1 and NM, d_{FM1} and d_{NM}, respectively, as indicated by the arrows, i.e. $d_{\mathrm{FM1}} \rightarrow 0$ and $d_{\mathrm{NM}} \rightarrow 0$. Spin fluctuations (or collective spin excitations) become important when a ferromagnetic layer is reduced in thickness

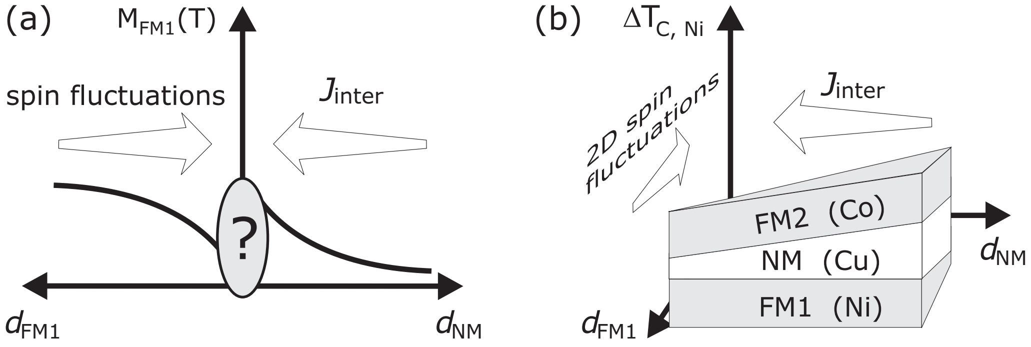

Figure 5.1: (a) Schematic illustration of two important effects in magnetic trilayers: (i) the spin fluctuations mainly determined by d_{FM1}, and (ii) the IEC mainly determined by d_{NM}. The two effects compete to finally determine M_{FM1} in the limit of low d_{FM1} and d_{FM2} [148]. (b) Schematic illustration of a ferromagnetic cross wedge trilayer. $\Delta T_{\mathrm{C,Ni}}$ is controlled by two independent parameters: (i) the IEC depending on d_{NM}, and (ii) the thickness d_{FM1}, while d_{FM2} is kept constant [59].

down to the 2D limit. In this case the correlation length and the thickness of the ferromagnet may reach the same order of magnitude. The coupling between spins then occurs only along paths in a 2D plane – the third dimension is lost for possible coupling paths. Thus, enhanced spin fluctuations diminish the magnetization of ultrathin FM films at a finite temperature. Their Curie temperature is reduced according to the finite size scaling (see e.g. [61, 102, 149]). As indicated on the left hand side of the graph in Fig. 5.1 (a), larger spin fluctuations lower the magnetization M_{FM1} of FM1 when its thickness d_{FM1} is reduced. The right hand side of the graph illustrates the second effect which leads to the opposite, i.e. an enhancement of the magnetization: The strength J_{inter} of the IEC is mainly determined by the thickness d_{NM} of NM. Disregarding the oscillatory contribution, $|J_{\mathrm{inter}}|$ will become larger if d_{NM} is reduced. Due to the IEC some of the "lost" coupling is regained, the spin fluctuations are suppressed and the magnetization increases. Thus, it is clear that the result of the competition between the spin fluctuations in 2D and the IEC when both d_{FM1} and d_{NM} are reduced can only be fully described when the two effects are considered in conjunction. Of course, in a full description, the oscillatory behavior of the IEC has to be included, too.

Up to now, numerous investigations of the IEC exist that treat either the dependence on the thickness of FM1 or the spacer thickness separately. The oscillatory character of the IEC (ferromagnetic, FM, or antiferromagnetic, AFM, coupling between FM1 and FM2) as a function of the spacer thickness d_{NM} is theoretically described [7, 8, 150, 151] and confirmed by experiments [15, 152]. The final goal of the investigations presented in this chapter is to combine the two effects as it is schematically indicated in the three-dimensional plot in Fig. 5.1 (b). In wedge samples it is possible to scan the thickness of one of the layers while the others are kept constant. Along the x-axis in Fig. 5.1 (b) the thickness of the ferromagnetic layer FM1 is varied. The increasing strength J_{inter} of the IEC with decreasing d_{NM} is represented on the y-axis. The z-axis of the schematic diagram shows $\Delta T_{\text{C,Ni}}$ as a measure of the spin-spin correlations, since this is the quantity which is directly accessible in the temperature-dependent XMCD experiments. Experiments have shown that $\Delta T_{\text{C,Ni}}$ oscillates as a function of the spacer thickness in the same manner as the IEC does [153, 154]. The relative shift $\Delta T_{\text{C,Ni}}/T_{\text{C,Ni}}$ of the critical temperature is larger than it has ever been observed in bulk magnetism. The first interpretations of this behavior have been carried out within mean field descriptions which turn out to be insufficient [14]. Collective spin excitations have to be taken into account in a more advanced theoretical description.

5.2 Summary of Related Research

Since Grünberg *et al.* have reported evidence for antiferromagnetic coupling of Fe layers across Cr interlayers [155] the systematics of this indirect coupling have attracted dramatic interest. Oscillations of the coupling through spacer layers have been reported for many different systems as a function of the spacer thickness, e.g. Ref. [156]. Recently, a continuous and reversible tuning of the coupling via hydrogen has been observed in Fe/V multilayers [157]. The interest in exchange coupled multilayers increased furthermore due to the discovery of the giant magnetoresistance (GMR) effect which is the main effect by which the data in today's hard disks is read. The relation of IEC and GMR is explained in detail for instance in Ref. [9]. However, the transport properties and GMR are not a topic of this present thesis and will not further be discussed.

Figure 5.2 reproduces the well-known results considering the two dependencies on d_{Cu} and d_{Ni} separately. On the left hand side, $\Delta T_{\text{C,Ni}}/T_{\text{C,Ni}}\,(d_{\text{Ni}})$ as discussed in Ref. [14] is plotted. The shift $\delta T_{\text{C,Ni}}/T_{\text{C,Ni}}$ becomes larger the thinner the Ni. A mean field description cannot reproduce the size of the shift found in experiments. Assuming a realistic coupling strength of $J_{\text{inter}} = 310$ μeV (solid line in Fig. 5.2) in MF results in a relative shift in the order of 5 % only. Applying the more advanced random phase approximation (RPA) which takes collective spin excitations

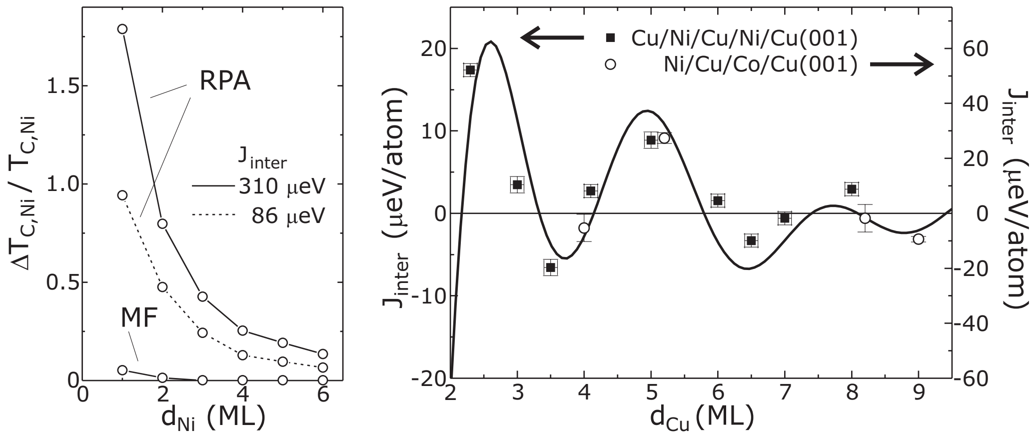

Figure 5.2: Review of the known dependencies $\Delta T_{\mathrm{C,Ni}}/T_{\mathrm{C,Ni}}\,(d_{\mathrm{Ni}})$ (left) Ref. [14], and $J_{\mathrm{inter}}\,(d_{\mathrm{Cu}})$ (right) Ref. [15]. If $J_{\mathrm{inter}} > 0$ the magnetizations of the two FM layers are aligned parallel whereas if $J_{\mathrm{inter}} < 0$ they are aligned antiparallel.

into account, the experimental findings can be explained [14]. On the right hand side of Fig. 5.2 the strength of the IEC is plotted as a function of the Cu spacer thickness as calculated by Bruno [150] and measured by FMR [15]. If $J_{\mathrm{inter}} > 0$ the magnetizations of the two FM layers will be aligned in parallel whereas if $J_{\mathrm{inter}} < 0$ they will be aligned antiparallel.

FMR provides the unique possibility to experimentally determine J_{inter} in absolute units [158] and thus complements the picture obtained by XMCD of the indirect coupling across a nonmagnetic spacer layer. The IEC provokes two resonance modes in FMR spectra, the acoustical and the optical mode, corresponding to an in-phase and an out-of-phase precession of the magnetizations in the two FM layers [159]. Ref. [160] provides a detailed review of FMR studies of the interlayer exchange coupling in ultrathin magnetic films. FMR is also the technique which has been mainly used to study the temperature dependence of the IEC experimentally [161, 162]. With the help of theory the origin of the temperature dependence may be revealed [162, 163]. The different mechanisms which are known to be present in such coupled trilayers, i.e. (i) the spacer effect due to the Fermi surface in the spacer layer, and (ii) the magnetic effect caused by the excitation and interaction of spin waves, may be separated [164]. Furthermore, analyzing the line width of the FMR spectra a spin-pumping effect has been evidenced in coupled trilayers recently [165]. It has been shown that the line width of such FMR spectra may be influenced by the temperature shift $\Delta T_{\mathrm{C,Ni}}$ of the Ni [166].

At $T = 0$ the oscillatory dependence of the IEC on the spacer thickness d_{Cu} is described by Bruno's expression [7, 8] as a sum of sine functions over the Fermi wave vectors k_n

$$J_{\text{inter}}(d_{\text{Cu}}) = \sum_n \frac{A_n}{d_{\text{Cu}}^2} \sin(k_n d_{\text{Cu}} + \phi_n) \ , \tag{5.1}$$

with amplitudes A_n and phase shifts ϕ_n. This form of Bruno's expression is called the asymptotic expansion and has been derived under the assumption of large spacer thickness. In Ref. [151] Bruno provides an extension, the "pre-asymptotic corrections". There, a further term of the approximation is included to improve the validity for thin spacer thickness below ~ 20 ML. However, the comparison of experimental results, e.g. FMR measurements [15], to Eq. (5.1) reveal a good overall agreement even without the correction. Moreover, the pre-asymptotic corrections introduce more parameters that are not known *a priori* and would have to be determined from a fit to the experiments. Of course, more fitting parameters make the results less reliable. Therefore, the extension is not applied in the present work. In the calculations for a Cu(100) spacer the superposition of two oscillations with periods $\Lambda_n = 2\pi/k_n$ and phase shifts ϕ_n has been determined: the short-period oscillation with $\Lambda_1 = 2.56$ ML and $\phi_1 = \pi/2$ and the long-period oscillation with $\Lambda_2 = 5.88$ ML and $\phi_2 = \pi$. They have been confirmed by experiments [153, 167]. For the ratio of the amplitudes, measurements find $A_1/A_2 = 1.3(5)$ [167]. Considering these values, the only remaining parameter is the absolute value A_1 in Eq. (5.1). A second example where Bruno's equation in the form of Eq. (5.1) was successfully applied is Fe/Au/Fe(100) [168, 169]. The authors of Refs. [168, 169] model the coupling in Fe/Au/Fe also by the sum of two sine waves and derive the phases, amplitudes, and oscillation periods within the model. Thus, they are able to describe their experimental data obtained by scanning electron microscopy with polarization analysis (SEMPA) in the studied range of $0 - 65$ ML Au without the pre-asymptotic correction [168]. Only for spacers of Au thinner than $\sim 2 - 3$ ML they find FM coupling across the spacer whereas the model predicts AFM coupling.

Special situations will occur in coupled trilayers if the easy axes of the two FM layers are perpendicular to each other, i.e. one in-plane and the other one out-of-plane. Their magnetization directions are determined by the competition between the anisotropy energy and the coupling energy. Depending on the thickness of the two FMs, spin reorientation between collinear and noncollinear arrangement of their magnetization occurs and a canted Ni magnetization is observed. Although a single Co/Cu(100) film will always have an in-plane easy axis, the Co magnetization can be turned out-of-plane by the indirect coupling to a perpendicular magnetized Ni film [170–173]. In the present thesis the studies were restricted to the case of parallel easy axes because Ni/Cu(100) never has an easy axis perpendicular to the surface of the sample and a Curie temperature of below room temperature at the same time. However, it is necessary for the present study to determine the Ni magnetization close to the Curie temperature. Thus, if this temperature is considerably above room temperature interdiffusion will happen and destroy the sample. This same problem of interdiffusion hinders also a measurement close to the Curie temperature of the second FM, i.e. the Co, in the present study. In a recent theoretical work bilayers of two strongly coupled FM films have been investigated within a mean field description [174]. They show that the coupling influences the Curie temperatures of both films which then in the bilayer show a common T_{C}. However, the major effect of giant spin fluctuations in 2D ferromagnets, as present in the trilayers investigated here, is evidenced at the temperature at which the Ni magnetization vanishes.

5.3 Element-Specific Magnetization Curves

Co/Cu/Ni trilayers have been used as a prototype system to study the IEC since the first pioneering experiments in the group [12, 175–178]. These experiments are summarized in this section. They revealed a separate onset of the magnetization of the two FM layers. Depending on the Ni and Co film thickness three different situations may occur: (i) $T_{\mathrm{C,Ni}} < T_{\mathrm{C,Co}}$ [12, 179, 180], (ii) $T_{\mathrm{C,Ni}} > T_{\mathrm{C,Co}}$ [181], and (iii) $T_{\mathrm{C,Ni}} \sim T_{\mathrm{C,Co}}$ [182]. The corresponding boundaries between the different cases have been determined by photoemission electron microscopy in cross-wedged Co/Cu/Ni/Cu(100) trilayers. Element-specific magnetic domain images were taken to reveal above which thickness magnetic ordering of the ferromagnetic layers is observed at room temperature [183]. The temperatures at which the individual Co and Ni magnetization vanish coincide with two peaks in the ac-susceptibility $\chi(T)$ [12, 14, 58, 184]. This brought up the academic question if the system had two Curie temperatures $T^*_{\mathrm{C,Ni}}$ and $T^*_{\mathrm{C,Co}}$ [185]. In the uncoupled case the susceptibility diverges at $T_{\mathrm{C,Ni}}$ whereas in presence of a nonvanishing IEC, it shows a resoncance-like peak. Thus, in a strict thermodynamical sense the trilayers do not show a phase transition at $T^*_{\mathrm{C,Ni}}$. The true phase transition of the whole trilayer happens at $T^*_{\mathrm{C,Co}}$ where both the Ni and the Co susceptibility show a singularity [58]. However, in a practical situation it makes sense to call $T^*_{\mathrm{C,Ni}}$ a quasi-critical temperature [12, 13]. Bergqvist *et al.* have calculated the spin-spin correlations for a trilayer with $T_{\mathrm{C,Ni}} < T_{\mathrm{C,Co}}$. They find that the spin-spin correlations above $T^*_{\mathrm{C,Ni}}$ are very small and indeed the Ni magnetization, which is the order parameter, practically vanishes [186].

The IEC induces a strong magnetization into the material with the lower Curie temperature [12, 14, 55, 180–183, 187]. If $T_{\mathrm{C,Ni}} < T_{\mathrm{C,Co}}$ then $T_{\mathrm{C,Ni}}$ will be shifted up to $T^{*}_{\mathrm{C,Ni}}$ by $\Delta T_{\mathrm{C,Ni}} = T^{*}_{\mathrm{C,Ni}} - T_{\mathrm{C,Ni}}$. The shift is always directed toward higher temperatures, independent of the relative alignment (parallel or antiparallel) of the Ni and Co magnetizations [153, 188]. It turned out that the relative shift $\Delta T_{\mathrm{C,Ni}}/T_{\mathrm{C,Ni}}$ becomes more pronounced for thinner Ni films [14].

All XMCD measurements of Co/Cu/Ni/Cu(100) trilayers prior to the work of the present thesis have been carried out in magnetic remanence. In fact, a single domain state is expected to be the ground state of an ultrathin FM with magnetization in the film plane [189]. Nevertheless, the formation of magnetic domains near the ordering temperature could not be ruled out. Remanent investigations of $4-8$ ML Ni/Cu(100), that are in-plane magnetized, have shown that magnetic domains exist in a wide temperature range of $T \approx 100-300$ K [190]. Such domains result in a reduced or vanishing net magnetization, which hampers the accurate determination of the ordering temperature. A vanishing net magnetization is a necessary but not sufficient condition for phase transition from the FM to the paramagnetic (PM) state [191]. The authors of Ref. [192] find that the magnetization determined for Cu/Ni bilayers in the early experiments is too low compared to their calculations. They suggest that this may be due to the fact that the bilayers are not fully saturated. However, all other experimental findings are fully confirmed by their investigations of Co/Cu/Ni trilayers and Cu/Ni bilayers on Cu(100) by their first-principles Green's function technique and fixed-spin-moment method. In the early experiments the thickness of the Ni layer was usually kept above ~ 4 ML, only two thinner cases of $d_{\mathrm{Ni}} = 3$ ML and $d_{\mathrm{Ni}} = 3.5$ ML exist [181]. The largest effects are however expected in the limit of low thickness. Therefore, the investigations presented in this work are carried out in a small applied magnetic field and include samples down to 2 ML Ni.

In many investigations the magnetism of the FM films has been treated in a static manner within a mean field theory (MFT). This description is insufficient to explain the effects of magnetic correlations in these ultrathin films [14, 55, 191, 193]. If collective spin excitations (spin waves) are not considered in the theoretical model, the large temperature shift will only be reproduced by assuming unphysically large coupling values [180, 194]. With reasonable values of the coupling, higher order contributions have to be taken into account to describe the experimental findings. In a localized picture this has been done using a Green's function theory (GFT) with random phase approximation (RPA) within a Heisenberg model [14, 58]. A second theoretical study uses the so-called spectral density approach within an itinerant single-band Hubbard model to describe the magnetism of coupled trilayers [55]. Here as well, the simplest approximation, which is the Stoner description, would not be sufficient to reproduce the experiments. Although an itinerant model is possibly more appropriate for $3d$ transition metals, the results of both approaches are in good agreement with the experiments yielding a strong shift $\Delta T_{\mathrm{C,Ni}}$ to higher values after the Co film has been evaporated on top, i.e., after the exchange coupling has been switched on. So it is not only the static exchange field of FM2 which acts on the magnetization of FM1. Static exchange fields of realistic values will shift $T_{\mathrm{C,Ni}}$ only by a few kelvin. Furthermore, the theoretical investigations revealed that the shift $\Delta T_{\mathrm{C,Ni}}$ is related to the strength J_{inter} of the IEC, i.e., the stronger the coupling the larger the shift. Therefore, it is also expected that $\Delta T_{\mathrm{C,Ni}}$ follows the oscillatory behavior of the IEC as a function of the spacer thickness. Indeed this has been observed experimentally [153, 154]. In a simple mean field picture, as it has been applied in this case up to now, J_{inter} and $\Delta T_{\mathrm{C,Ni}}$ depend linearly on each other [153, 154]. Since a MFT fails to reproduce the experimental $\Delta T_{\mathrm{C,Ni}}$, using it to determine $\Delta T_{\mathrm{C,Ni}}\,(J_{\mathrm{inter}})$ is also questionable. As will be shown in Sec. 5.6 considering the spin fluctuations appropriately, a nonlinear dependence follows from the Green's function approach applied by Jensen. Both theoretical pictures, the GFT considering localized spins in a Heisenberg model as well as the itinerant Hubbard model considering the band structure of the trilayers, expect a tail in the temperature-dependent Ni magnetization near the ordering temperature [14, 55, 58]. However, this tail was not observed in the earlier experiments [13, 52]. The clarification of this discrepancy between experiment and theory is crucial because it contributes to the understanding of the temperature dependence of the interlayer exchange coupling. The absence of the Ni tail would imply that J_{inter} vanishes when the magnetization of one FM component in the trilayer vanishes. Of course it is always more difficult to determine a vanishing quantity like M_{Ni} at $T_{\mathrm{C,Ni}}$ or $T^{*}_{\mathrm{C,Ni}}$, respectively, than to investigate a diverging one like e.g. the susceptibility.

5.4 New Improved Investigations Close to the Curie Temperature

Since in the present case the formation of magnetic domains cannot completely be ruled out when measuring in remanence only, the possibility to study X-ray absorption and XMCD with applied magnetic fields has been established in the UHV chamber as described in Chapter 3. New improved investigations of the coupled tri-

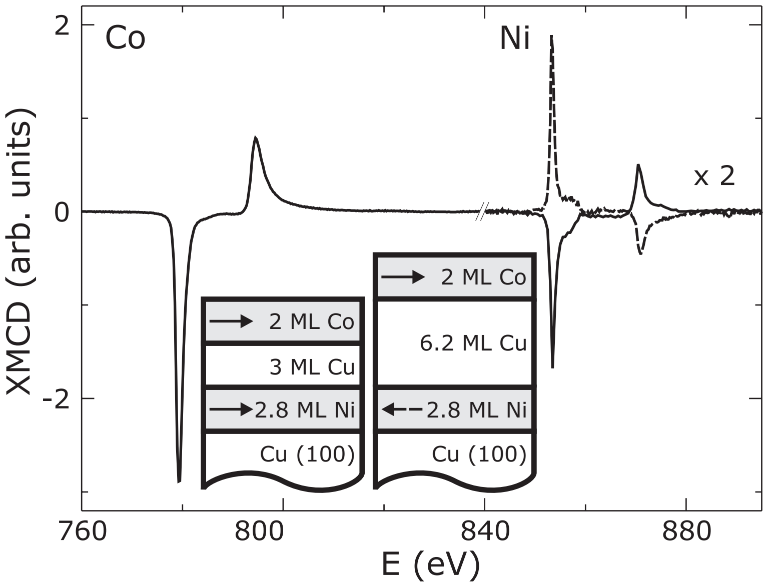

Figure 5.3: Two examples of the full XMCD spectra at both the Co and the Ni $L_{2,3}$ edges [78]. The XMCD signal at the L_3 edge of Co is negative in both cases whereas the sign of the Ni XMCD depends on the thickness of the Cu spacer layer, thus revealing the relative orientation of the element specific Ni and Co magnetizations. Only one line is shown for Co since the two are identical within the experimental noise.

layers have been carried out by applying a weak magnetic field $\vec{H}$ with $\mu_0 H \approx 4$ mT. This field is on the one hand large enough to suppress the formation of magnetic domains close to $T_{\mathrm{C,Ni}}$, on the other hand it is small enough not to cause a sizable field induced magnetization in the Ni film [179, 180]. The thickness of the layers is chosen such that all measurements can be done in a convenient temperature range $T \lesssim 330$ K to avoid considerable interdiffusion. The substrate crystal was oriented such that the XMCD was measured along the [110] direction, which is the easy magnetization direction of Co/Cu/Ni/Cu(100) trilayers. In Fig. 5.3 two examples of the full XMCD spectra at both the Co and the Ni $L_{2,3}$ edges are plotted. The graph shows nicely that the sign of the Ni XMCD signal depends on the thickness of the Cu spacer layer, thus revealing if the element specific magnetizations of Co and Ni are aligned parallel or antiparallel by the IEC.

In the new investigations the Ni thickness has been lowered down to $d_{\mathrm{Ni}} \approx 2$ ML. Particular attention has been drawn to the Ni magnetization near the Ni Curie temperature. Concerning the question of presence or absence of a tail of the Ni magnetization in the coupled trilayer systems, the Ni magnetization has to be investigated thoroughly close to the Curie temperature. Investigating $M_{\mathrm{Ni}}(T)$ close to $T_{\mathrm{C,Ni}}$ (or $T^*_{\mathrm{C,Ni}}$) requires the measurement of small magnetic signals with a sufficiently high density of temperature points. The progress achieved with the new undulator beamlines at third generation synchrotrons has very much improved the technical possibilities. Taking advantage of the high photon flux and the high and constant degree of circular polarization in the desired energy range small XMCD signals near the Curie temperature can be determined more precisely. Better statistics can be obtained in shorter time and therefore, measuring $M_{\mathrm{Ni}}(T)$ close to $T^*_{\mathrm{C,Ni}}$ with a relatively high density of data points has become feasible.

In the early experiments several full energy-dependent XMCD spectra were recorded and averaged at each temperature to determine the magnetization. Due to the improved synchrotron technique it is now possible to apply a “time scan procedure” to determine the temperature-dependent magnetization curve. At each temperature the absorption signal is recorded as a function of time for the two directions of magnetization at two fixed energy positions: (i) at the maximum of the L_3 edge and (ii) in the pre-edge region where the XMCD signal is zero. In this way both absorptions signals are measured many times and their values are obtained as the average of many data points. A corresponding example of the raw time scan data is shown in Fig. 5.4. As discussed in Sec. 2.3 the temperature-dependent magnetization can be derived from the ratio $\Delta A_3/A_3$. Since for the $3d$ FMs neither the ratio of orbital and spin moment nor the line shape of the XMCD spectrum depends

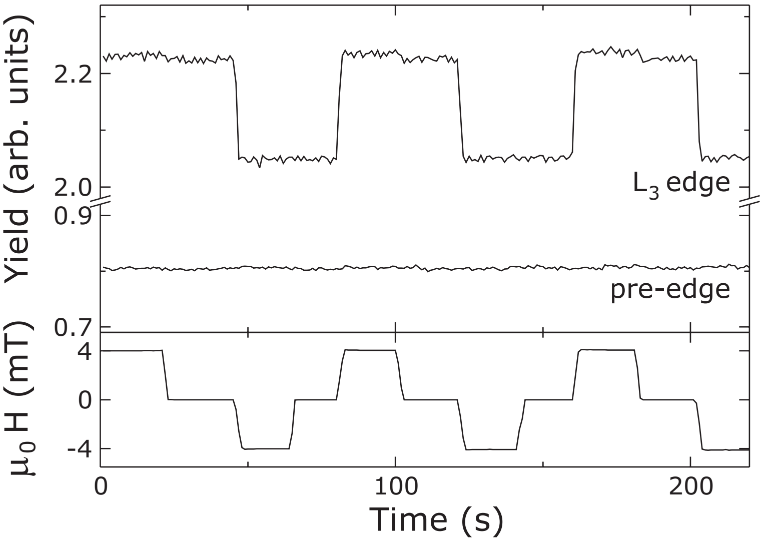

Figure 5.4: Illustration of the time scan procedure to determine $M(T)$. The upper panel shows the absorption signal at the L_3 edge and in the pre-edge region as a function of time as it was directly measured. The lower panel shows $\mu_0 H$ of the corresponding static magnetic field $\vec{H}$ which was applied [78].

on the temperature, the magnetization curve can be determined from the helicity-dependent absorption signals at the maximum of the L_3 edge $\mu^{\pm}_{L_3}$ and in the pre-edge region $\mu^{\pm}_{\mathrm{pre}}$ via

$$M \propto \frac{(\mu^{+}_{L_3} - \mu^{+}_{\mathrm{pre}}) - (\mu^{-}_{L_3} - \mu^{-}_{\mathrm{pre}})}{\frac{1}{2}\left((\mu^{+}_{L_3} - \mu^{+}_{\mathrm{pre}}) + (\mu^{-}_{L_3} - \mu^{-}_{\mathrm{pre}})\right)} \,. \tag{5.2}$$

The normalization to the signal in the pre-edge region is necessary to zero out any artificial magnetic background. An artificial magnetic background may occur due to small stray fields inside the chamber. Such backgrounds are usually below one percent of the XMCD signal at the L_3 edge maximum. In many cases like, for instance, the one shown in Fig. 5.4, they do not occur at all. To determine the absolute value of the magnetization the full energy-dependent XMCD is recorded and analyzed solely at the lowest temperature.

In principle, the time scan procedure can also be applied to measure element-specific hysteresis loops. Then the absorption signal is recorded along with the voltage at the coil while the current in the coil is steadily changed. The voltage of the coil can be converted to the magnetic field and thus the magnetization plotted as a function of the magnetic field. For a more careful determination of the magnetic field a current measurement with the help of a precise shunt in series with the coils is advisable.

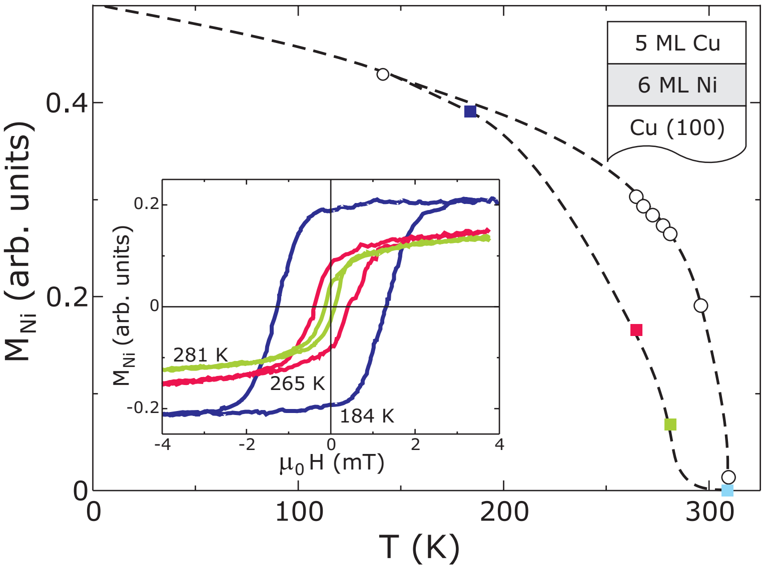

Figure 5.5: Temperature-dependent Ni magnetization of a Cu/Ni/Cu(100) bilayer system in a constant applied magnetic field $\vec{H}$ with $\mu_0 H = 4$ mT ($\hat{=}$ 40 G, open circles), and at remanence (solid squares). The dashed lines serve as guides to the eyes. The inset shows the Ni hysteresis from which the remanent magnetization has been determined at three different temperatures [179].

From the voltage at this shunt the current can be determined more precisely and from this current the magnetic field of the coils. However, under the given conditions for the present experiments, the temperature of the coils and thus their resistance varied only very little. The error introduced by the temperature variation is much lower than the one due to the calibration of the magnetic field.

Figure 5.5 shows the magnetization of a 6 ML Ni film on Cu(100) covered with 5 ML Cu. Two cases of the temperature-dependent magnetization are given: (i) $M_{\mathrm{Ni}}(T)$ in an applied magnetic field $\vec{H}$ with $\mu_0 H = 4$ mT ($\hat{=}$ 40 G) as obtained from the time scan procedure (open circles) and (ii) $M_{\mathrm{Ni}}(T)$ in remanence (solid squares) as determined from the element-specific hysteresis loops given in the inset. At $T = 184$ K the magnetization saturates for $\mu_0 H \gtrsim 3$ mT. At temperatures $T \gtrsim 200$ K the magnetization in a field with $\mu_0 H = 4$ mT decreases less than the one in zero field. Such a behavior occurs if magnetic domains are formed near the Curie temperature of these films [195]. In the present case a magnetic field with $\mu_0 H \approx 3$ mT ($\hat{=}$ 30 G) is sufficient to ensure a single domain state even close to the Ni Curie temperature without inducing considerable magnetization in addition. It is true, that the proper magnetization curve is given by the spontaneous magnetization,

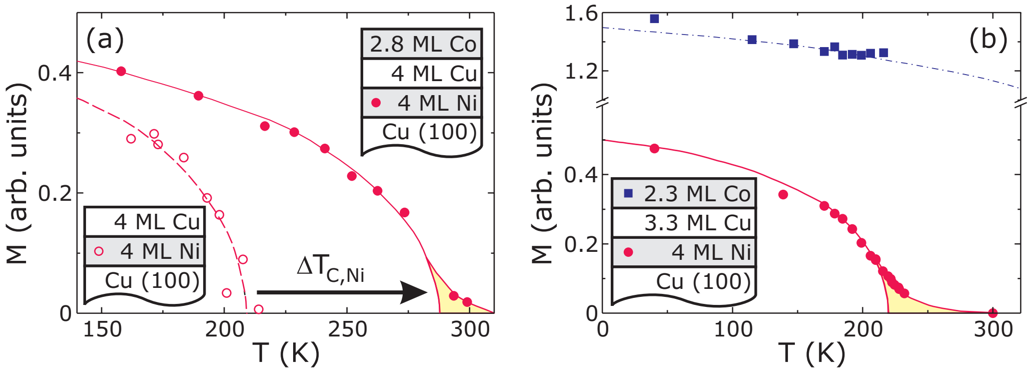

Figure 5.6: (a) Ni magnetization of a trilayer before (open circles) and after (solid circles) evaporation of the Co layer measured at $\mu_0 H = 4$ mT and (b) individual Ni (circles) and Co magnetization (squares) of a Co/Cu/Ni trilayer. A tail in the Ni magnetization near the ordering temperature is clearly visible [179].

i.e. without magnetic field. However, if a multi domain state occurs, a small magnetic field will help to align the domains so that their contributions are not averaged out due to the measuring procedure. Although it is not a main issue of the present study, it shall be noted that operating in low fields of a few milliteslas only, attention needs to be paid to small stray fields. Zero current in the electro magnet does not necessarily correspond to zero magnetic field in the sample. Already a tiny magnetic stray field may displace the hysteresis loops significantly and result in an erroneous measurement of the proper magnetization.

After establishing the new measuring procedure, Co/Cu/Ni trilayers comparable to the ones of the early experiments have been reinvestigated first. Figure 5.6 demonstrates that the results of the early experiments are basically confirmed apart from the fact that now the tail close to $T^*_{\mathrm{C,Ni}}$ is observed. Part (a) of the figure shows the temperature-dependent magnetization of the Ni layer in a coupled trilayer system measured at $\mu_0 H = 4$ mT both before (open circles) and after depositing the Co film (solid circles). The Ni magnetization of the bilayer, i.e. a 4 ML Ni film capped with 4 ML Cu, was studied first and vanishes at $T_{\mathrm{C,Ni}} \approx 210$ K. By evaporating 2.8 ML Co on top of the already investigated sample, an IEC is applied to the Ni film whose properties are now known. In the trilayer $T^*_{\mathrm{C,Ni}} \approx 290$ K is $\Delta T_{\mathrm{C,Ni}} \approx 80$ K higher than $T^*_{\mathrm{C,Ni}}$ of the bilayer system. Measuring in the small magnetic field, $\Delta T^*_{\mathrm{C,Ni}}$ cannot be addressed to an effect due the formation of magnetic domains close to the Curie temperature. In fact, the IEC can now be considered the main reason for the large change of the Ni magnetization curve. In addition, the new experiments show the tail which is predicted by theory, both in the itinerant approach [55] and the localized Heisenberg model [14]. Part (b) of Fig. 5.6 shows the element-specific and temperature-dependent Ni and Co magnetization curves of a second example of a trilayer system. Since it has been measured with a larger density of points especially close to $T^*_{\mathrm{C,Ni}}$ the line shape of the Ni magnetization becomes evident. In principle, with the theoretical model by P. Jensen described in Sec. 2.4, it is possible to exploit the line shape by fitting $M_{\mathrm{Ni}}(T)$. The various coupling parameters are then obtained as fitting parameters. However, it is shown in Sec. 5.5 how some of the model parameters can be obtained in a more restrictive way thus leaving less free fitting parameters.

Knowing these first results of the improved measurements, more detailed experiments and analysis have finally been tackled. As already explained above in detail, the aim was on the one hand to extend the investigated Ni thickness range down to $d_{\mathrm{Ni}} = 2$ ML and on the other hand to analyze and interpret the results with simultaneous consideration of two known effects in trilayer systems – the 2D character determined by d_{Ni} and the oscillatory dependence of the IEC on d_{Cu}. Figure 5.7 shows one example of a new experiment with all the details concerned to characterize the IEC and the critical behavior close to the Curie temperature. The results of the experiments are given by the various symbols: open circles for $M_{\mathrm{Ni}}(T)$ in the Cu/Ni/Cu(100) bilayer before the evaporation of Co, i.e. without IEC, solid circles for $M_{\mathrm{Ni}}(T)$ and solid squares for $M_{\mathrm{Co}}(T)$ after the evaporation of Co on top. The solid and dot-dashed lines are guides to the eye. The influence of the IEC is obvious from the experimental data and shows the expected behavior. The Ni magnetization has become larger in a wide temperature range after the Co film was deposited. Even in a temperature range where M_{Ni} was zero within the experimental error before, it has gained considerable magnitude and the expected tail is clearly visible.

For the further analysis the characteristic Ni temperatures of the two cases need to be determined, i.e. $T^*_{\mathrm{C,Ni}}$ for the full trilayer and $T_{\mathrm{C,Ni}}$ for the corresponding Cu/Ni/Cu(100) bilayer system. This is done with the help of a standard magnetization curve which has been obtained from various measurements of thin Ni/Cu(100) films in the thickness range $3-5$ ML [13]. The temperature-dependent magnetization curves of these Ni films were plotted in reduced units $M/M_0\,(T/T_{\mathrm{C,Ni}})$ and averaged to provide the standard magnetization curve. The curve follows Bloch's law in the low temperature range where the temperature dependence of the magnetization results from thermal excitation of spin waves and a power law close $T_{\mathrm{C,Ni}}$ according to the theory of second order phase transitions [78]. Fitting this standard curve to the data points of $M_{\mathrm{Ni}}(T)$ of a Cu/Ni/Cu(100) sample yields $T_{\mathrm{C,Ni}}$

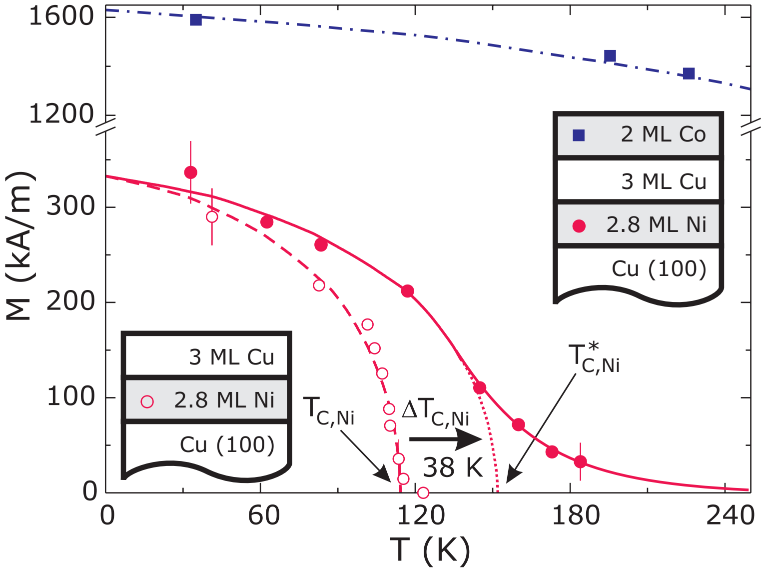

Figure 5.7: Ni (circles) and Co (squares) magnetizations $M_{\mathrm{Ni}}(T)$ and $M_{\mathrm{Co}}(T)$ as obtained from XMCD measurements. The influence of the IEC on the Ni magnetization becomes obvious when comparing $M_{\mathrm{Ni}}(T)$ before (open circles) and after (closed circles) the deposition of the Co film. The solid and dot-dashed lines are guides to the eye. A standard Ni magnetization curve (see text) is fitted to the Ni data points (dashed and dotted lines), yielding $T_{\mathrm{C,Ni}}$ and $T^*_{\mathrm{C,Ni}}$ [59].

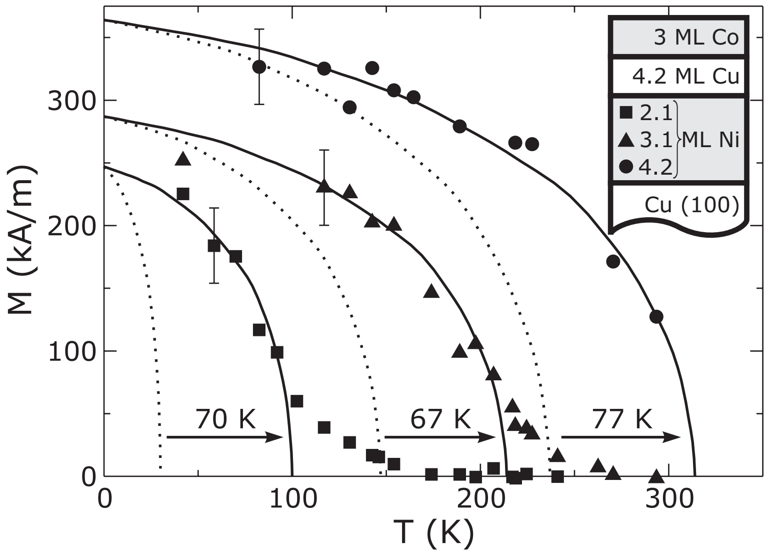

Figure 5.8: $M_{\mathrm{Ni}}(T)$ in a trilayer (solid symbols) with a Ni staircase and constant d_{Cu} and d_{Co}. The curves of $M_{\mathrm{Ni}}(T)$ are given as expected for Cu-capped Ni films with the same thickness (dotted lines). The resulting temperature shift $\Delta T_{\mathrm{C,Ni}}$ due to the IEC is indicated by the arrows [148].

with an accuracy of a few kelvin (dashed line in Fig. 5.7). Determining $T^*_{\mathrm{C,Ni}}$ of the Co/Cu/Ni/Cu(100) trilayer is less evident due to the presence of the tail. Therefore, the same standard magnetization curve is fitted to the data points of $M_{\mathrm{Ni}}(T)$ in the trilayer (dotted line in Fig. 5.7). The point at which the fitted standard curve meets the x-axis is identified with the temperature $T^*_{\mathrm{C,Ni}}$. This $T^*_{\mathrm{C,Ni}}$ is identical to the temperature of the maximum of the calculated susceptibility [14, 78]. By the procedure of fitting the standard magnetization curve, $\Delta T_{\mathrm{C,Ni}} \approx 38$ K is determined for the example given in Fig. 5.7. An alternative would be to use the inflection point of the temperature-dependent magnetization as it has been done in the earlier theoretical work [14, 58]. For the measured curves this is hardly possible because the experimental data points have an error, many more of them would be needed, and no analytical function is known to describe $M_{\mathrm{Ni}}(T)$ in the trilayer.

The shift $\Delta T_{\mathrm{C,Ni}}$ as well as the strength of the IEC may depend sensitively on the thickness of each of the three layers. To ensure that the observations can be attributed exclusively to the change of one parameter, namely the thickness of one particular constituent, staircase trilayer samples were prepared. In these samples one constituent has macroscopic steps of ~ 2 mm width, each with a different thickness. The other two layers have a constant thickness over the whole sample area. Figure 5.8 shows the temperature-dependent magnetization of the three Ni steps in a sample with constant $d_{\mathrm{Cu}} = 4.2$ ML and $d_{\mathrm{Co}} = 3$ ML (solid symbols, Ni thickness as specified in the figure). In the case of this trilayer sample with a staircase Ni layer the Cu/Ni bilayer systems have not been measured separately due to the limited beamtime. Therefore, $T_{\mathrm{C,Ni}}$ is taken from a fit to all measured Curie temperatures as a function of the thickness, $T_{\mathrm{C,Ni}}(d)$ according to a finite size scaling [196]

$$\frac{T_{\mathrm{C,Ni}}(d_{\mathrm{Ni}})}{T_{\mathrm{C,Ni}}^{\mathrm{bulk}}} = 1 - C_0\, d_{\mathrm{Ni}}^{-1/\nu} \tag{5.3}$$

where ν is a critical exponent and C_0 a system-dependent constant. The Curie temperature of bulk Ni is $T_{\mathrm{C,Ni}}^{\mathrm{bulk}} = 627$ K. The new experiments reveal Curie temperatures of the Cu-capped Ni films that are approx. 30 K higher than in earlier experiments [197]. The early experiments were carried out in remanence only and probably suffered from the formation of magnetic domains close to $T_{\mathrm{C,Ni}}$. For the present case of Cu-capped Ni films $C_0 = 1.67$ and $\nu = 1.46$ have been determined [78]. Since besides the reduction of the coordination number also a reduction of the magnetic moments at the interfaces affects the Curie temperature here, ν cannot be directly identified with the critical exponent of theoretical predictions. Calculations predict values in the range of 0.5 to 1 depending on the model used. These values are smaller than our result because the theoretical models consider only the decrease of the coordination [196]. The dotted lines in Fig. 5.8 represent the temperature-dependent magnetizations as they are expected for the corresponding bilayer systems according to the finite size scaling of $T_{\mathrm{C,Ni}}\,(d_{\mathrm{Ni}})$. The absolute temperature shift $\Delta T_{\mathrm{C,Ni}}$ does not vary much. The relative shift $\Delta T_{\mathrm{C,Ni}}/T_{\mathrm{C,Ni}}$ becomes larger for the thinner Ni film because $T_{\mathrm{C,Ni}}$ of the thinner Ni film is smaller. The characteristic temperatures of the staircase sample of Fig. 5.8 are summarized in Table 5.1 together with the ones of all other investigated samples. The results are sorted in three groups: (i) the dependence on the Ni film thickness d_{Ni}, (ii) the dependence on the Cu spacer thickness d_{Cu}, and (iii) some dependence on the Co film thickness d_{Co}. Some samples are listed twice in the table to facilitate the comparison.

5.5 Determination of Model Parameters: The Intralayer Coupling

The theoretical model introduced in Sec. 2.4 contains three coupling parameters: the strength of the intralayer couplings J_{Ni} and J_{Co} and the strength of the interlayer exchange coupling J_{inter}. J_{Ni} and J_{Co} describe the coupling between spins within

Table 5.1: Measured ordering temperatures of the Ni films in Cu/Ni/Cu(100) and Co/Cu/Ni/Cu(100), and the resulting $\Delta T_{\mathrm{C,Ni}} = T^{*}_{\mathrm{C,Ni}} - T_{\mathrm{C,Ni}}$. The systems marked by a † refer to samples with a staircase layer of either Ni or Co. According to the description in Chapter 3, the error in the thickness calibration is within 5 %. The fourth column denotes whether the Ni and Co films are coupled ferromagnetic (FM) or antiferromagnetic (AFM) to each other. Some samples are listed twice for a better comparison of the results.

d_{Ni} (ML)	d_{Cu} (ML)	d_{Co} (ML)	IEC	$T_{\mathrm{C,Ni}}$ (K)	$T^{*}_{\mathrm{C,Ni}}$ (K)	$\Delta T_{\mathrm{C,Ni}}$ (K)	$\Delta T_{\mathrm{C,Ni}}/T_{\mathrm{C,Ni}}$
Ni dependence:							
†2.1	4.2	3.0	AFM	30(15)	100(5)	70(16)	2.3(17)
†3.1	4.2	3.0	AFM	147(16)	214(5)	67(17)	0.46(16)
†4.2	4.2	3.0	AFM	237(13)	314(5)	77(14)	0.32(7)
2.6	3.3	2.4	AFM	85(18)	175(5)	90(19)	1.1(5)
2.8	3.0	2.0	FM	114(6)	152(5)	38(8)	0.33(8)
3.8	3.0	2.0	FM	223(2)	251(6)	28(6)	0.13(3)
Cu dependence:							
2.8	3.0	2.0	FM	114(6)	152(5)	38(8)	0.33(8)
2.8	6.2	2.0	AFM	117(2)	141(5)	24(5)	0.21(5)
2.8	7.0	2.0	AFM	114(6)	132(5)	18(8)	0.16(8)
2.8	7.8	2.0	FM	111(3)	138(4)	27(5)	0.24(5)
Co dependence:							
†3.1	4.2	2.2	AFM	147(16)	170(5)	23(17)	0.16(13)
†3.1	4.2	1.5	AFM	147(16)	156(5)	9(17)	0.06(12)

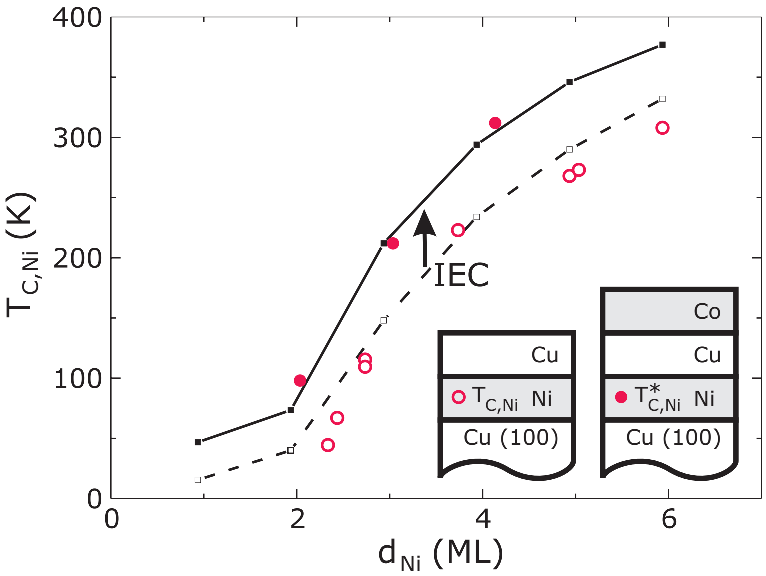

Figure 5.9: $T_{\mathrm{C,Ni}}$ and $T^*_{\mathrm{C,Ni}}$ as functions of the Ni film thickness d_{Ni} (experiment: open and full circles, theory: solid and dashed lines). In the calculation the IEC is $J_{\mathrm{inter}} = 310\ \mu\mathrm{eV/bond}$ [59].

the same FM layer. J_{inter} describes the coupling between the two FM layers of Ni and Co across the nonmagnetic spacer layer of Cu. The IEC can only be present, if two FM films exist. The intralayer coupling within one FM layer is always present, independent of the presences of a second FM layer. It does not depend on J_{inter} since it includes properties of the single film only. Therefore, the idea is to determine J_{Ni} and J_{Co} from the measurements of the single films first.

In the case of Ni, the intralayer coupling is considered layer-resolved, as introduced in Sec. 2.4. For the inner layers of the film the bulk coupling $J_{\mathrm{Ni}}^{\mathrm{interior}} = 15.3$ meV/bond is assumed. The interface layers next to the Cu substrate and the Cu spacer are assumed to possess a reduced coupling $J_{\mathrm{Ni}}^{\mathrm{interface}}$ in the same manner as the magnetic moments at the interface are reduced [56]. Changing the values for J_{Co} does not influence the results of the calculations significantly so that a layer-dependent approach is not necessary. The bulk value $J_{\mathrm{Co}} = 34.3$ meV/bond is used. The only intralayer coupling parameter still missing is $J_{\mathrm{Ni}}^{\mathrm{interface}}$. It is determined by fitting the calculated $T_{\mathrm{C,Ni}}\,(d_{\mathrm{Ni}})$ to the measured $T_{\mathrm{C,Ni}}\,(d_{\mathrm{Ni}})$. During this fitting procedure only $J_{\mathrm{Ni}}^{\mathrm{interface}}$ is varied. Figure 5.9 shows $T_{\mathrm{C,Ni}}\,(d_{\mathrm{Ni}})$ of various experiments (open circles) together with the calculated curve (dashed line) as it is obtained after $J_{\mathrm{Ni}}^{\mathrm{interface}} = 3.1$ meV/bond has been determined. The solid circles in Fig. 5.9 represent $T^*_{\mathrm{C,Ni}}$ of the staircase sample with three Ni steps given in Fig. 5.8 and the first three rows of Table 5.1. The thickness $d_{\mathrm{Co}} = 3$ ML is chosen to ensure $T_{\mathrm{C,Co}} \gg T_{\mathrm{C,Ni}}$. In this sample the Cu and Co layer is identical for all three Ni steps. After the determination of the intralayer coupling parameters the only remaining parameter to adjust in the calculations is J_{inter}. The correct value is found once the calculations reproduce the shift $\Delta T_{\mathrm{C,Ni}}$. The $T^{*}_{\mathrm{C,Ni}}\,(d_{\mathrm{Ni}})$ curve in Fig. 5.9 is obtained by applying an IEC of $J_{\mathrm{inter}} = 310$ meV/bond. The calculated curve (solid line) meets the experimental values (solid circles) almost perfectly. In presence of the IEC, i.e. in the full trilayer, the Ni magnetization vanishes at systematically higher temperatures than in the Cu/Ni bilayer. The calculations within the GFT are carried out with integer thickness from 1 to 6 ML, showing that even 1 ML remains FM with $T_{\mathrm{C,Ni}} > 0$ K. Of course, preparing a film with 1 ML thickness only is not possible in a real experiment. It is true that one may deposit the mass equivalent of 1 ML but the result will not be the smooth, perfect layer of 1 ML as it is easily plugged into the calculations. The experimental sample would consist of many islands rather than one closed layer and any consideration as a layered sample would be questionable. The shift $\Delta T_{\mathrm{C,Ni}}$ in Fig. 5.9 is in the range of $\sim 30 - 80$ K. Relating this absolute shift to $T_{\mathrm{C,Ni}}$ of the single film it becomes more pronounced the thinner the Ni because $T_{\mathrm{C,Ni}}$ decreases with the Ni thickness. In the thinnest case of $d_{\mathrm{Ni}} = 2.1$ ML the relative shift of the magnetic ordering temperature of the ultrathin 2D-like film exceeds 200 % which is never possible in 3D bulk material.

When all coupling parameters are known, they can be used in the theoretical model and the full temperature-dependent magnetization curves can be calculated. Figure 5.10 shows the calculated $M(T)$ for the experiment given in Fig. 5.7. Merely the thickness has been put to integer numbers because of the requirements by the theoretical model. In the two figures 5.7 (experiment) and 5.10 (theory) lines with the same style represent the same physical quantity. First, $M_{\mathrm{Ni}}(T)$ is calculated for the Cu/Ni/Cu(100) system (dashed line) and the full Co/Cu/Ni/Cu(100) trilayer (solid line). Strictly speaking, the results for the Cu/Ni/Cu(100) system are obtained by setting $J_{\mathrm{inter}} = 0$ to decouple the Co film from the Ni. Thus, the same code can be used to calculate both the bilayer and the trilayer systems. The shift $\Delta T_{\mathrm{C,Ni}}$ has now to be determined in a way that it is directly comparable to the experiment. Therefore, the calculated curve for the uncoupled case is stretched on the x-axis such that it follows $M_{\mathrm{Ni}}(T)$ of the full trilayer in presence of an IEC (dotted line in Fig. 5.10). The temperature where the stretched curve meets the x-axis is then identified with $T^{*}_{\mathrm{C,Ni}}$. In the case shown in Fig. 5.10 $T_{\mathrm{C,Ni}} = 151$ K, $T^{*}_{\mathrm{C,Ni}} = 188$ K, and $\Delta T_{\mathrm{C,Ni}} = 37$ K are determined. The absolute temperatures are somewhat larger in the calculation than in the experiment, but comparing with the

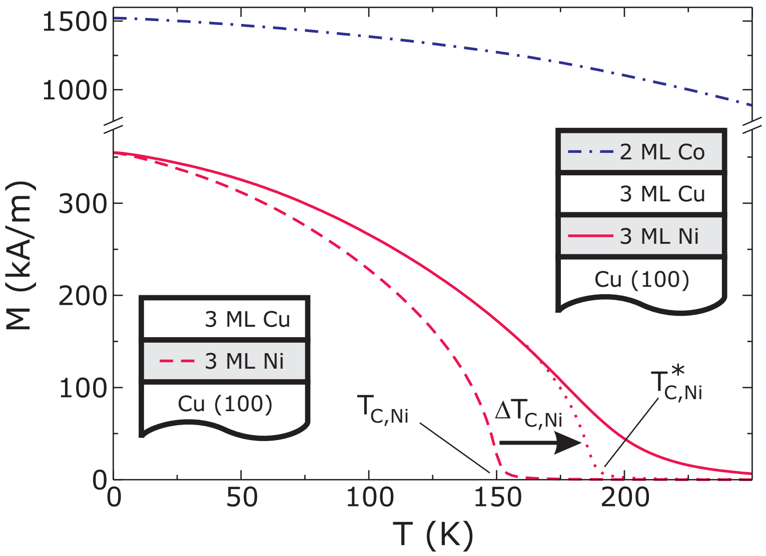

Figure 5.10: Calculated Ni magnetization of a single Ni film (dashed line) and of a Ni film coupled to a Co film (solid line) as a function of the temperature, corresponding to the experiment shown in Fig. 5.7. The dot-dashed line refers to the Co magnetization. $J_{\text{inter}} = 86\ \mu\text{eV/bond}$ is used. An external magnetic field $\vec{H}$ with $\mu_0 H = 4$ mT causes the small tail in the calculated Ni magnetization of the bilayer. By applying $M_{\text{Ni}}(J_{\text{inter}} = 0)$, $T^*_{\text{C,Ni}}$ (dotted line) and $\Delta T_{\text{C,Ni}} = 37$ K are identified (see text) [59].

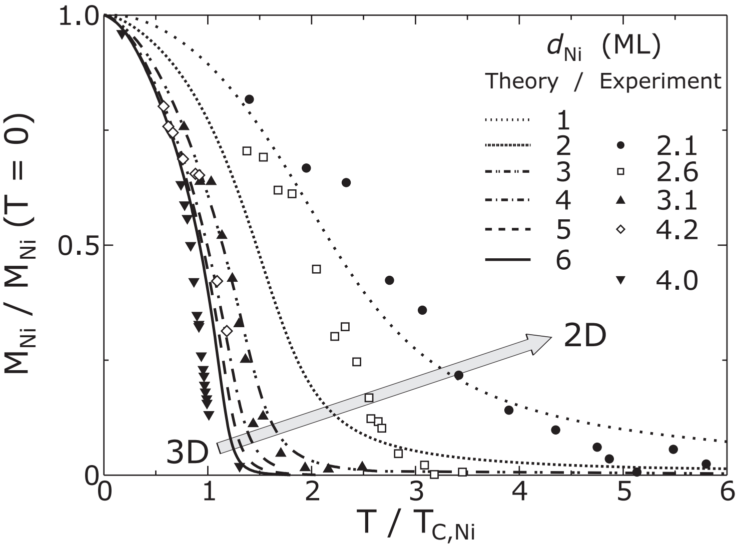

Figure 5.11: Magnetization $M_{\mathrm{Ni}}(T)/M_{\mathrm{Ni}}(T=0)$ as a function of the relative temperature $T/T_{\mathrm{C,Ni}}(d_{\mathrm{Ni}})$ scaled by the corresponding Curie temperature of the Cu-capped Ni films. For the calculations $J_{\mathrm{inter}} = 310$ μeV/bond and $d_{\mathrm{Co}} = 3$ ML are used. The cases with a Ni thickness of 2.1, 2.6, 3.1, and 4.2 ML are given in Table 5.1. The top-down triangles ($d_{\mathrm{Ni}} = 4.0$ ML) represent a case without IEC ($J_{\mathrm{inter}} = 0$) [59].

curves given in Fig. 5.9 this discrepancy can be explained by the slightly different thickness. The calculated shift is identical within the accuracy to the experimental finding of Fig. 5.7 where $\Delta T_{\mathrm{C,Ni}} = 38$ K. Indeed the shift is the important quantity from which the coupling strength is determined, in the case of Fig. 5.10 $J_{\mathrm{inter}} = 86$ μeV/bond $\cong 1$ K/bond. The full dependence of $\Delta T_{\mathrm{C,Ni}}\,(J_{\mathrm{inter}})$ is discussed in the next Sec. 5.6. It is needed for the final goal to combine the influence of the IEC as a function of d_{Ni} with the one of d_{Cu}. The determined value of the IEC is of the same order of magnitude as obtained by ferromagnetic resonance (FMR) [152].

The temperature dependence of the Ni magnetization has been studied in theory and experiment for different Ni thickness. The results are summarized in Fig. 5.11. To point out that the IEC influences the Ni magnetization most in the thinnest Ni films, M_{Ni} normalized to $M_{\mathrm{Ni}}\,(T=0)$ is plotted as a function of T normalized to $T_{\mathrm{C,Ni}}\,(J_{\mathrm{inter}}=0)$. The GFT calculations (lines) as well as the experiments (symbols) show that M_{Ni} close to the Curie temperature of the bilayer, i.e. at $T/T_{\mathrm{C,Ni}} = 1$ in Fig. 5.11, is more enhanced the thinner the Ni film. The tail is most pronounced for the thinnest Ni (theory: 1 ML Ni, dotted line; experiment: 2.1 ML Ni, solid circles). The static exchange field of the Co film is not sufficient to explain this finding [198].

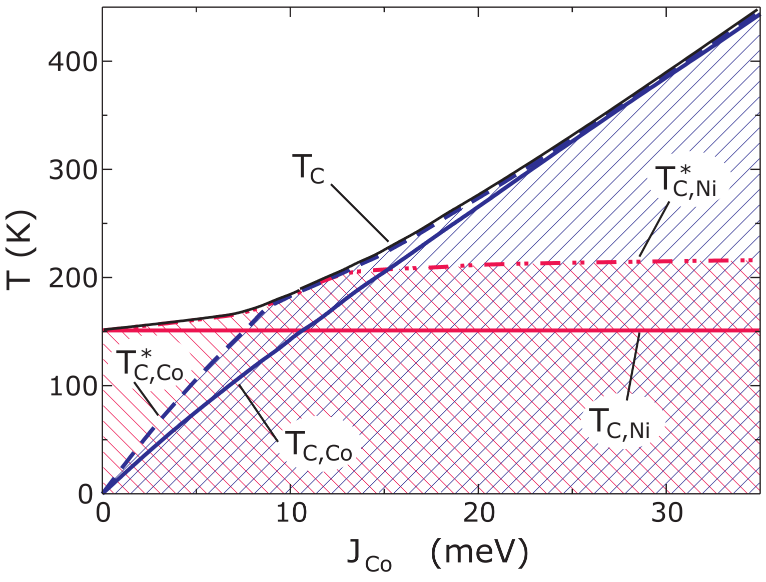

Figure 5.12: Calculated phase diagram of the Co/Cu/Ni trilayer system. The Curie temperatures T_C, $T_\mathrm{C,Ni}$, and $T_\mathrm{C,Co}$, and the quasi-critical temperatures $T^*_\mathrm{C,Ni}$ and $T^*_\mathrm{C,Co}$ are shown as a function of the exchange coupling J_Co in the Co film [59].

A higher order contribution, i.e. the second term of Eq. (2.21) has to be taken into account in the calculations, i.e. spin-spin correlations in the GFT. The results of the four experiments with a Ni thickness of 2.1, 2.6, 3.1, and 4.2 ML are the ones given in the first four rows of Table 5.1. Three of them are part of the same staircase sample and thus have the same Cu and Co thickness. The one with $d_\mathrm{Ni} = 2.6$ ML has slightly different Cu and Co thickness, but it fits into the series given in Fig. 5.11. All four cases have a comparable IEC. Of course, preparing samples with exactly identical IEC is hardly possible in any experiment since strictly speaking also the thickness of the FMs influence the IEC, although the main contribution is by d_Cu [150, 199]. Thus, in the present study J_inter is assumed to be in good approximation constant when d_Cu is constant. In general, the oscillatory coupling depends also on the thickness of the Co layer on top, but to less extend. The change of the magnetization of the trilayers can be seen by comparing their $M_\mathrm{Ni}(T)$ to the one with the top-down triangles ($d_\mathrm{Ni} = 4.0$ ML) which represents a case without IEC ($J_\mathrm{inter} = 0$). Although the experimental and theoretical results differ in the 3D to 2D crossover by approximately 1 ML, they show the same trend and the overall agreement is clearly visible.

The theoretical model applied here includes simplifications in various points. However, it gives major insight into the physics of the trilayers without introducing the full complexity of a more advanced itinerant theory of $3d$ ferromagnetism. To demonstrate the capability of the model, a phase diagram of the Co/Cu/Ni trilayer system has been calculated. It is shown in Fig. 5.12. The different characteristic temperatures of the trilayer T_C, $T_\mathrm{C,Ni}$, $T^*_\mathrm{C,Ni}$, $T_\mathrm{C,Co}$, and $T^*_\mathrm{C,Co}$ are plotted as functions of the direct exchange coupling J_Co in the top Co film. In the calculations $d_\mathrm{Ni} = 3$ ML, $d_\mathrm{Co} = 2$ ML, and $J_\mathrm{inter} = 310$ μeV/bond were entered. Lets first discuss the boundaries of the diagram: $J_\mathrm{Co} = 0$ corresponds to a system without Co, yielding $T_\mathrm{C,Ni} = 150$ K of a 3 ML Ni film covered with Cu. It is trivial that in this case $T^*_\mathrm{C,Ni} = T_\mathrm{C,Ni}$ and the Curie temperature T_C of the whole system coincides with the one of Ni. The other limit of the diagram is at $J_\mathrm{Co} \approx 34$ meV/bond which corresponds to a realistic exchange coupling of 2 ML Co [180]. In this case $T^*_\mathrm{C,Ni} = 216$ K of the trilayer is larger than $T_\mathrm{C,Ni}$ of the Cu-capped Ni film without Co due to the IEC. The characteristic temperatures of Co, $T_\mathrm{C,Co}$ and $T^*_\mathrm{C,Co}$, are both well above the characteristic temperatures of Ni. Since here the Ni film is much weaker than the Co, the Curie temperature $T_\mathrm{C,Co}$ of the single Co film and $T^*_\mathrm{C,Co}$ of the Co in the trilayer coincide. The Curie temperature of the whole system is always identical to the one of the ferromagnet with the larger quasi-critical temperature in the trilayer, i.e. on the right hand side of the diagram $T_\mathrm{C} = T^*_\mathrm{C,Co}$. The two edges of the diagram represent the situation of the experiments of the present work: Before the evaporation of the Co film, the left hand side ($J_\mathrm{Co} = 0$) is valid, whereas after Co has been deposited the right hand side ($J_\mathrm{Co} \approx 34$ meV/bond) where $T_\mathrm{C,Co} > T^*_\mathrm{C,Ni}$ illustrates the facts. In between the edges a variety of possible situations can be considered. The whole T–J_Co plane is separated into four areas by the curves of the quasi-critical temperatures $T^*_\mathrm{C,Ni}$ (dash-dotted line) and $T^*_\mathrm{C,Co}$ (dashed line). These areas are differently hatched. (i) In the area below the dash-dotted line, hatched with lines of one direction, the Ni film is FM. (ii) In the area below the dashed line, hatched with lines of the other direction, the Co film is FM. (iii) In the area where the two hatchings overlap to a crossed hatching, both the Ni and the Co film are FM. (iv) In the white area without any hatching, both films are PM and the whole trilayer is above its transition temperature T_C. To summarize short: where one hatching is present, one film is FM and the other one is PM, where both hatchings overlap both films are FM, and where there is no hatching at all both films are PM. In the hatched areas three relevant cases can be distinguished: (i) If $J_\mathrm{Co} \lesssim 9$ meV the quasi-critical temperature of Co $T^*_\mathrm{C,Co} < T_\mathrm{C,Ni}$. $T_\mathrm{C,Co}$ is shifted up to $T^*_\mathrm{C,Co}$ by the IEC. Interestingly, even a small increase of $T_\mathrm{C,Ni}$ to $T^*_\mathrm{C,Ni}$ is visible. (ii) In the range of 9 meV $\lesssim J_\mathrm{Co} \lesssim$ 13 meV the two quasi-critical temperatures $T^*_\mathrm{C,Co}$ and $T^*_\mathrm{C,Ni}$ coincide. They are both increased compared to the Curie temperatures of the single

Ni and Co films. (iii) In the region $J_{\mathrm{Co}} \gtrsim 13$ meV where $T_{\mathrm{C,Co}} > T^{*}_{\mathrm{C,Ni}}$ the largest increase of $T_{\mathrm{C,Ni}}$ is observed.

5.6 Simultaneous Consideration of Spacer and FM Film Thickness

Up to now the results of the new improved experiments and the accompanying calculations of the temperature-dependent magnetization have been explained and discussed. In this last section of the chapter the final and most important aim of the new investigations is presented: The oscillatory behavior of the IEC as a function of the Cu spacer thickness is simultaneously considered together with its growing influence when approaching the 2D limit as a function of the Ni thickness. Looking again at the well-known and often discussed results of Fig. 5.2, one important fact has to be pointed out: On the y-axis two different quantities are plotted in the two cases: the coupling strength J_{inter} and the shift $\Delta T_{\mathrm{C,Ni}}/T_{\mathrm{C,Ni}}$. Therefore, it is essential to express $\Delta T_{\mathrm{C,Ni}}/T_{\mathrm{C,Ni}}$ as a function of J_{inter}, before the desired combination of the two known effects can be accomplished. In earlier works a linear dependence has been derived in a MFT [153]. However, since MFT does not satisfy the description of the temperature shift $\Delta T_{\mathrm{C,Ni}}$, it is appropriate to find an improved description of $\Delta T_{\mathrm{C,Ni}}\,(J_{\mathrm{inter}})$ within the GFT.

The shift $\Delta T_{\mathrm{C,Ni}}$ is always toward higher temperature, independent of the relative alignment (FM or AFM) of the individual Ni and Co magnetizations. Their relative orientation is reflected in the sign of J_{inter}, i.e. $J_{\mathrm{inter}} > 0$ for FM and $J_{\mathrm{inter}} < 0$ for AFM coupling. For the present study, the relative temperature shift $\Delta T_{\mathrm{C,Ni}}/T_{\mathrm{C,Ni}}$ has been calculated as a function of $|J_{\mathrm{inter}}|$ for Ni films with $1\,\mathrm{ML} \leq d_{\mathrm{Ni}} \leq 6\,\mathrm{ML}$. In the calculations here, it is assumed that the variation of d_{Cu} only influences J_{inter}, and not the intralayer couplings J_{Co} and J_{Ni}. As Fig. 5.13 shows the dependence is clearly nonlinear. These results indicate again that magnetic fluctuations are efficiently suppressed even by relatively small coupling strengths.

Knowing the relation between $\Delta T_{\mathrm{C,Ni}}/T_{\mathrm{C,Ni}}$ and $|J_{\mathrm{inter}}|$ finally provides the possibility for the desired combination: The influence of the spin fluctuations visualized in the relative shift $\Delta T_{\mathrm{C,Ni}}/T_{\mathrm{C,Ni}}$, depends on the one hand on d_{Ni} (2D character of FM1). On the other hand it depends on the strength of the IEC, i.e. $|J_{\mathrm{inter}}|$. Combining both variables with the help of the relation given in Fig. 5.13, the 3D plot as anticipated at the beginning can be established. The result is a curved surface of $\Delta T_{\mathrm{C,Ni}}/T_{\mathrm{C,Ni}} =$

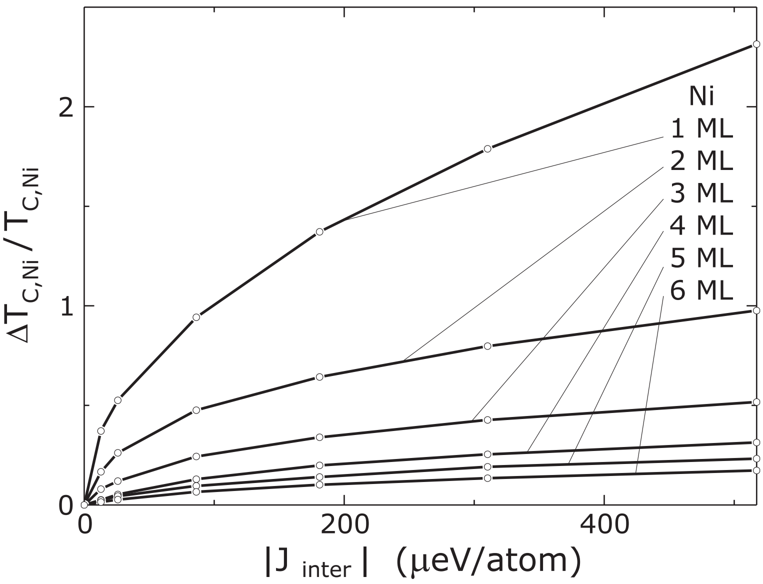

Figure 5.13: Relative temperature shift $\Delta T_{\mathrm{C,Ni}}/T_{\mathrm{C,Ni}}$ of the Ni magnetization as a function of the strength of the IEC $|J_{\mathrm{inter}}|$. Different Ni film thickness is assumed as indicated [59].

$f\,(d_{\mathrm{Ni}}, d_{\mathrm{Cu}})$. Figure 5.14 shows this final result of the calculation together with the experimental findings. The experimental data of Table 5.1 together with results of earlier investigations are shown as full dots and in the projection to the d_{Ni}–d_{Cu} plane (open circles). The results are sorted according to the thickness of the Co film: $d_{\mathrm{Co}} = 2$ ML in Fig. 5.14 (a) and $d_{\mathrm{Co}} = 3$ ML in Fig. 5.14 (b). The zero plane is given by $J_{\mathrm{inter}} = 0$ with a shift $\Delta T_{\mathrm{C,Ni}} = 0$. Of course, the shift is indeed always positive. However, the illustration has been chosen such that regions with a parallel alignment of the magnetizations of the two FM layers ($J_{\mathrm{inter}} > 0$, above the zero plane) are distinguished from the ones with an antiparallel alignment ($J_{\mathrm{inter}} < 0$, below the zero plane).

The envelope of $\Delta T_{\mathrm{C,Ni}}/T_{\mathrm{C,Ni}}$ as a function of d_{Cu} decreases approximately as d_{Cu}^{-2} for $d_{\mathrm{Ni}} \geq 5$ ML. For thinner Ni films $\Delta T_{\mathrm{C,Ni}}/T_{\mathrm{C,Ni}}$ decreases more softly because of the nonlinear dependence on J_{inter}. The experimental and theoretical shifts $\Delta T_{\mathrm{C,Ni}}/T_{\mathrm{C,Ni}}$ agree reasonably well for $d_{\mathrm{Ni}} \geq 3$ ML and $d_{\mathrm{Co}} = 2$ ML (Fig. 5.14 (a)). For $d_{\mathrm{Co}} = 3$ ML (Fig. 5.14 (b)) the experimental shifts are much larger than the theoretical ones, especially for a Ni thickness below 3 ML. By matching the calculated relative temperature shifts $\Delta T_{\mathrm{C,Ni}}/T_{\mathrm{C,Ni}}$ to the experimental data, the IEC can be quantitatively derived. Assuming the various quantities in Bruno's expression as explained in Sec. 5.2 ($\Lambda_1 = 2.56$ ML, $\phi_1 = \pi/2$, $\Lambda_2 = 5.88$ ML, $\phi_2 = \pi$,

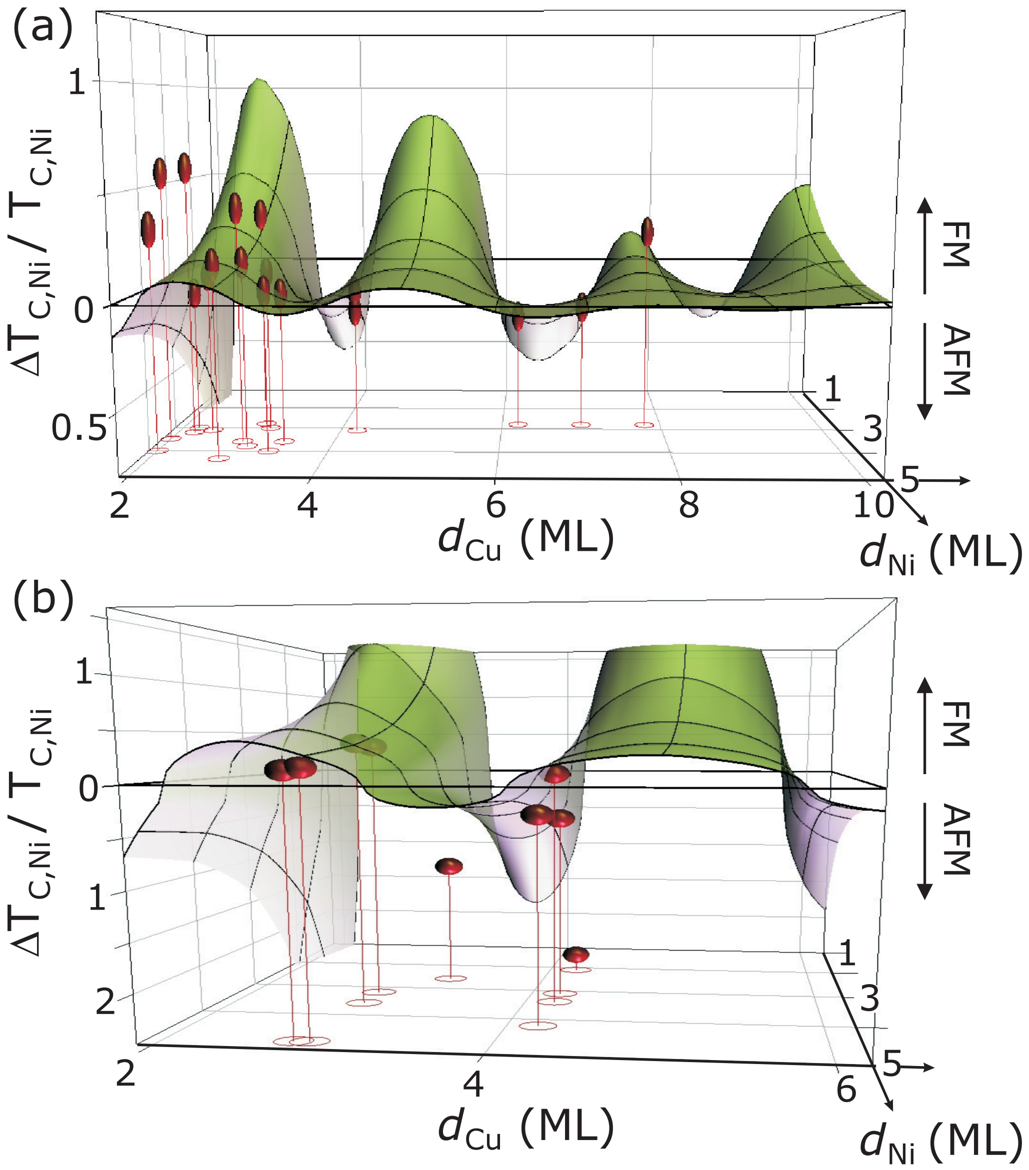

Figure 5.14: Two-parameter plot of the relative temperature shift $\Delta T_{\mathrm{C,Ni}}/T_{\mathrm{C,Ni}}\,(d_{\mathrm{Ni}}, d_{\mathrm{Cu}})$ for Co/Cu/Ni/Cu(100) trilayers as a function of the Ni film thickness d_{Ni} and the thickness d_{Cu} of the Cu spacer layer with (a) $d_{\mathrm{Co}} = 2$ ML and (b) $d_{\mathrm{Co}} = 3$ ML [59].

and $A_1/A_2 = 1.3(5)$), the amplitude of the short-period oscillation in Bruno's expression Eq. (5.1) is obtained to be $A_1\,(d_{\mathrm{Co}} = 2\ \mathrm{ML}) = 1.0$ meV/bond by fitting the experimental results of Fig. 5.14 (a). This value corresponds to a coupling energy of $J_{\mathrm{inter}}\,(T = 0, d_{\mathrm{Cu}} = 5\ \mathrm{ML}) = 63\ \mu\mathrm{eV/bond}$. This value fairly agrees with results of FMR measurements with $d_{\mathrm{Co}} = 2$ ML [152]. For a proper comparison the FMR data, which were recorded at room temperature, have to be extrapolated to $T = 0$. Determining A_1 for $d_{\mathrm{Co}} = 3$ ML (by fitting to the experimental data of Fig. 5.14 (b) by the same procedure) yields a 10 times larger value as compared to the previous case. Such a large variation of $A_1\,(d_{\mathrm{Co}})$ is not expected when just increasing the thickness of the Co film. The difference between the results for 2 ML and 3 ML Co indicates, that the whole set of experimental data cannot yet be fitted with one unique set of parameters in the calculations. However, the basic picture of the interpretation fits for both cases. Further studies are needed to get a unified set of principal parameters. Various improvements, and most likely a combination of them, may be possible. First of all, the samples consist of extremely thin layers which are not as flat and smooth as assumed for the calculations. It is a general problem that the easy to handle samples in theory have perfect surfaces and interfaces whereas the experimentalist can hardly produce them. Samples in the experiment always include inhomogeneities. The difficulties become most pronounced at very low thickness, because the relative contribution of the interfaces is larger the thinner the layers. Therefore, at very low thickness, e.g. in Fig. 5.14 (a) at 2 ML Cu and in Fig. 5.14 (b) at approx. 2 ML Ni, the experimental results can hardly be brought into agreement with the calculations. In the extreme case of an only 2 ML thin spacer the coupling is experimentally found to be FM whereas Bruno's model predicts AFM coupling. This same discrepancy occurs for Fe/Au/Fe [168]. Isaev *et al.* however find FM coupling between Ni and Co across a 1 ML Cu spacer in their calculations and thus agree with the experimental findings [192]. Roughness and a noninteger film thickness might sensitively change $\Delta T_{\mathrm{C,Ni}}$ and J_{inter}, in particular when approaching the ultrathin film limit for both Ni and Cu, where the largest influence on the Ni magnetization is expected. It has been shown that roughness may play a crucial role for the IEC [200]. Thus, one useful but difficult task for the theorists would be to introduce roughness and maybe also interdiffusion at the interfaces in their samples. However, also other aspects of the theory may need further consideration. In the simple model used, only the direct intralayer coupling of Ni is separated into a bulk and an interface component ($J_{\mathrm{Ni}}^{\mathrm{interior}}$ and $J_{\mathrm{Ni}}^{\mathrm{interface}}$). A more advanced model might include a complete thickness dependence of J_{Co} and J_{Ni}. Such a variation due to quantum well states has been determined [201, 202]. Furthermore, using a Heisenberg Hamiltonian with localized spins represents an approximation to the present itinerant-electron magnets Ni and Co, although such a model reproduces a number of important features, e.g. Bloch's $T^{3/2}$ law for the decrease of the bulk magnetization, a Curie-Weiss behavior of the susceptibility for $T > T_\mathrm{C}$, etc. Moreover, the applied Tyablikov decoupling could underestimate the effect of spin fluctuations in particular for 2D systems, which should be tested by improved approximations beyond RPA [203]. It should be noted that the present theoretical calculation and the recently published one in Ref. [63] will give quantitatively satisfactory results if the anisotropies are much smaller than the exchange coupling. However, for ultrathin films out-of-plane magnetocrystalline anisotropies may be important. Schwieger *et al.* consider exchange and magnetic anisotropy equally important in their theory [63]. Future treatments within this theory are advisable to further analyze the experimental results of this work. In conclusion however, fair agreement between the experimental results and the calculations even in the simplified model show the importance of spin fluctuations in the coupled trilayers especially at thin thickness. Furthermore, the desired combination of the two dependencies on d_Ni and d_Cu and their simultaneous consideration has been accomplished.

Chapter 6

Detailed Analysis of XMCD at the $L_{2,3}$ Edges of Gd, Tb, and Dy

In this chapter the systematics of the detailed fine structure of XMCD at the $L_{2,3}$ edges of Gd, Tb, and Dy is investigated. The three elements are characterized by their partly, however, more than half filled $4f$ shell. Their large magnetic moment arises mostly from the highly localized $4f$ orbitals which have negligible overlap on neighboring sites. The exchange interaction between the $4f$ electrons is mediated by the polarization of the $5d$ conduction band [204]. Since XMCD spectroscopy is a shell-selective method for magnetic measurements it provides a useful tool for studying the $5d$ magnetism directly and separately from the $4f$ magnetism which is up to 10 times stronger than the $5d$ one. Interpretation of XMCD at the $L_{2,3}$ edges of rare earth elements is a matter of discussion since the first spectra have been published [205]. At the beamlines of today's synchrotron sources, rich and detailed fine structures in the XMCD at the $L_{2,3}$ edges of rare earth elements can be revealed. One reason for additional fine structure features is the importance of electric quadrupole (E2) transitions for the X-ray absorption of the rare earth elements. Further analysis of the rare earth XMCD as, for example, determining magnetic moments like it its possible for the $3d$ ferromagnets by the integral sum rules, is rarely discussed. Is it possible to understand the line shape of the spectra and extract the magnetic information out of them? The first, and most important, step to answer this question is to carefully measure and properly normalize XMCD spectra. Most of the XMCD data of rare earth elements available up to now stem from measurements of compounds. These compounds are in general complex structures including various interactions. This may well introduce additional complication in the fine structure of the spectra. Therefore, measurements on high purity single crystals have been carried out in the present work. The series of Gd, Tb, and Dy has been chosen as an example. Additionally, the magnetism of single crystals of these elements has been studied in great detail and can be considered understood. The correctness of the results of any analysis procedure can be easily crosschecked with the known magnetic properties. Therefore, single crystals of the rare earth elements are good candidates to be studied in an XMCD experiment to obtain the XMCD spectra and finally evidence what happens when the assumption of dipolar transitions only is no longer justified.

6.1 Quadrupolar and Dipolar Transitions at $L_{2,3}$ Edges of $4f$ Elements – Previous Research

Initial states at the $L_{2,3}$ edges are the $2p$ states. Due to the selection rules for electric dipole transitions (E1) Eq. (2.7), the final states for electrons excited by X-rays in elements of the $4f$ series are the located in the $5d$ shell. It was pointed out that electric quadrupolar (E2) transitions from $2p$ initial states to the $4f$ shell may be significant in XMCD spectra of the $4f$ elements [16]. The final states of these E2 transitions are in the partly occupied $4f$ shell, according to the selection rules for E2 transitions Eq. (2.8). As was suggested in Ref. [16] the presence of E2 transitions can be evidenced by employing the dependence of the dichroic signal on the angle ϑ between the photon wave vector and the magnetization of the sample. Any deviation from a pure $\cos\vartheta$ dependence is a sign for the presence of quadrupolar contributions [16]. However, the separation of E1 and E2 remains difficult because the angular dependence contains both contributions. Since the first evidence of these quadrupolar transitions in XMCD at the L_3 edges of Dy in a $Dy_{0.4}Tb_{0.6}$ alloy [17] and of Yb in $YbFe_2$ [18] many more XMCD investigations on a large variety of rare earth compounds have been carried out, e.g. [206–208]. The occurrence of the quadrupolar transitions leads to an additional rich spectroscopic fine structure in the XMCD of the rare earth elements. These additional features in the XMCD appear at the low energy side of the edge, because the E2 transitions appear lower in energy than the E1 transition.

6.2 Measured XAS and XMCD

In the present work the X-ray absorption of the lanthanides Gd, Tb, and Dy has been measured at their $L_{2,3}$ edges on single crystals as described in Sec. 3.4. At

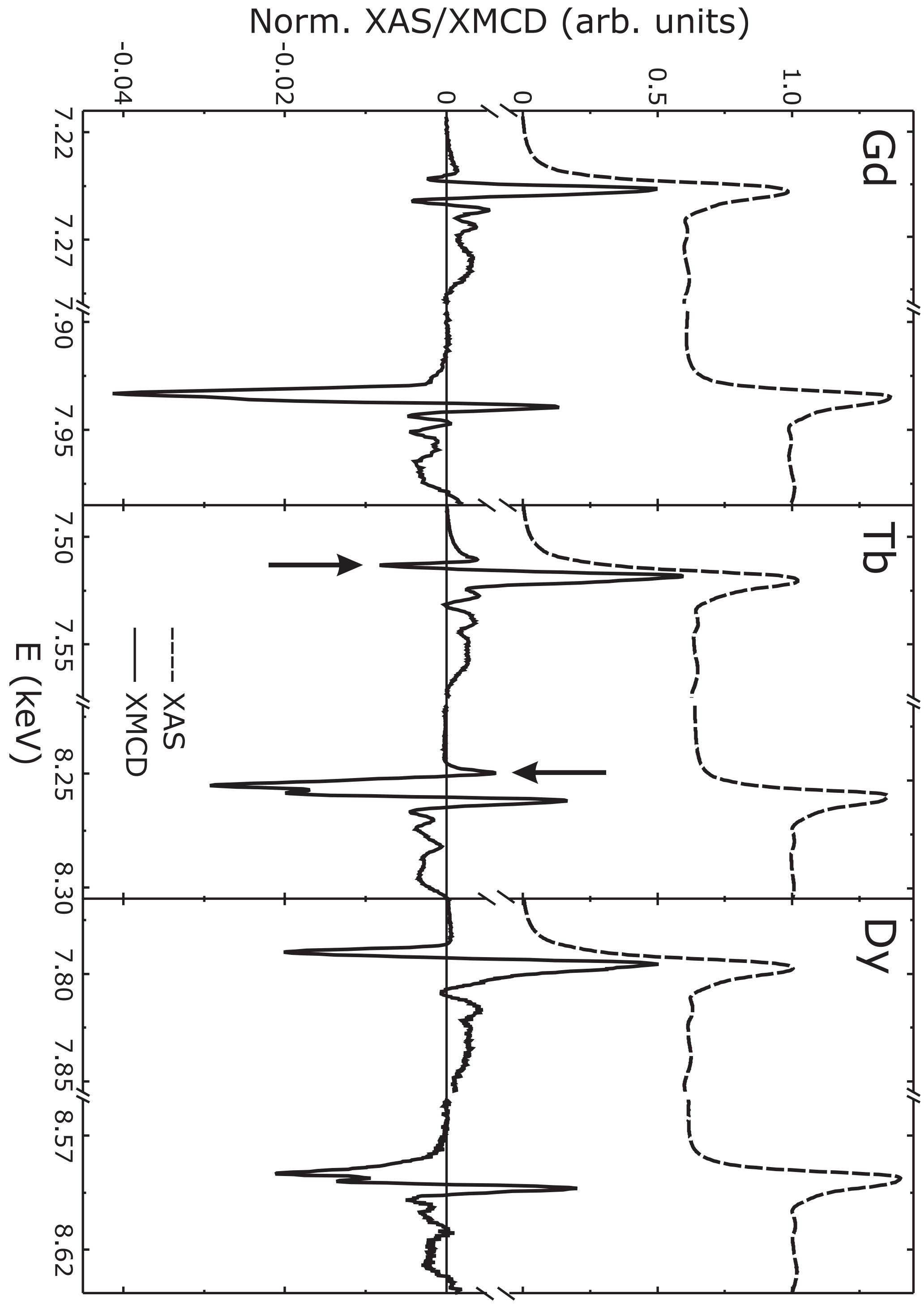

Figure 6.1: Normalized XAS (dashed line) and XMCD (solid line) at the $L_{2,3}$ edges of Gd ($T = 10$ K, $\mu_0 H = 3$ T), Tb ($T = 4$ K, $\mu_0 H = 7$ T), and Dy ($T = 5$ K, $\mu_0 H = 5$ T). The y-scale for the XAS is given above the axis break, the y-scale for the XMCD below. The arrows in the case of Tb mark the E2 contributions.

room temperature all three elements have a hexagonal closed packed (hcp) structure. They are cut such that the c-axis for Gd, the b-axis for Tb, and the a-axis for Dy are aligned perpendicular to the surface. In the cases of Tb and Dy these would be the crystallographic easy axis of magnetization in bulk material [209, 210]. For bulk Gd the crystallographic easy axis would be on a cone around the c-axis [210, 211]. However, all three samples exhibit a huge shape anisotropy. Therefore, a field of up to 7 T is applied to overcome the shape anisotropy and align the magnetization perpendicular to the surface during the measurements at normal incidence.

Figure 6.1 shows the spin-averaged XAS (dashed line, y-scale above break) and the XMCD (solid line, y-scale below break) of the three elements Gd, Tb, and Dy at low temperature. The XAS are normalized to a total edge jump of 1. The size of the XMCD is given according to this normalized scale. Since the two edges are well separated in energy they have been measured individually with the high density of data points to clearly identify all the spectral fine structure in the XMCD. The L_3 edge to L_2 edge step ratio is determined from a long scan with a lower density of data points including both edges. This step ratio is found to vary for the three elements. It is 1.55 : 1, 1.75 : 1, and 1.6 : 1 for Gd, Tb, and Dy, respectively.

Although the difference in the absorption spectra for the two helicities $\mu^+(E)$ and $\mu^-(E)$ can hardly be made out by eye (not shown in Fig. 6.1), clear XMCD spectra can be determined. Detailed fine structures are revealed. These fine structures are more clearly visible in Fig. 6.2 where they are discussed in detail. In the present Fig. 6.1 a broader overview is given. In the XAS the beginning of the EXAFS wiggles can be seen right above the edges. Although the extended energy range is not a focal point of the present thesis it is worth mentioning that in the extended energy range the magnetic EXAFS is observed. For rare earth metals the intensity of the magnetic EXAFS in comparison to the XMCD signal near the edge is much larger than for example for the $3d$ transition metals. The MEXAFS of the rare earth elements is essentially proportional to the total $4f$ magnetic moment, whereas in the NEXAFS reagion the XMCD is dominated by dipole transitions to the spin-polarized $5d$ densities of states. However, the $5d$ moment is only a small friction of the $4f$ moment. This explains the relative scales of the XMCD to MEXAFS intensities which are different at the $L_{2,3}$ edges of $3d$ FMs, cf. [212]. For details about the magnetic EXAFS in rare earth elements see Refs. [37, 213].

The most remarkable observation in the XMCD of Fig. 6.1 is that the main contribution of the signals is positive at the L_3 edge and negative at the L_2 edge. This main contribution to the XMCD corresponds to the dichroism of the electric dipole transitions. From a simple estimation with the help of the spin sum rule Eq. (2.16) one concludes that the spin of the 5d moments is aligned antiparallel to the one of the 4f moments. However, this conclusion is at odds with classical magnetometry measurements for the following reason: the magnetic moment of Gd, Tb, and Dy metal is $7.63\mu_\mathrm{B}$, $9.34\mu_\mathrm{B}$, and $10.33\mu_\mathrm{B}$, respectively [209, 210, 214, 215]. Assuming that in the solid one of the 4f electrons from the atomic configuration is transfered into the 5d shell, it follows from Hund's rule that the 4f contribution is at maximum $7\mu_\mathrm{B}$, $9\mu_\mathrm{B}$, and $10\mu_\mathrm{B}$ for Gd, Tb, and Dy, respectively. Strictly speaking, Hund's rules have been derived for the atomic case. However, they have proven good approximations also for solids in many cases and the 4f moment in the solids will not be larger than in the free atom. Therefore, from classical measurements of the magnetic moment it follows that the 5d moment of Gd, Tb, and Dy is aligned parallel to the 4f moment and has a size of at least $0.63\mu_\mathrm{B}$, $0.34\mu_\mathrm{B}$, and $0.33\mu_\mathrm{B}$, respectively. These discrepancies are explained by the neglect of the spin dependence of the transition matrix elements when deriving the sum rules [47, 48, 216]. Only if the transition matrix elements are independent of the spin, the XMCD spectra will reflect the profile of the difference of the density of states for spin-up and spin-down electrons. In general however, this is not true, since the exchange potential of spin-up 4f electrons is attractive for the spin-up 5d states whereas the 5d spin-down states are not so affected [204, 216, 217]. Therefore, applying the original integral sum rules may yield questionable results for Gd, Tb, and Dy.

Slightly below the edges, the quadrupolar (E2) contributions to the XMCD occur with opposite sign as the dipolar contributions. In the case of Tb they are marked by arrows in Fig. 6.1. They appear at lower energy than the edges themselves because of the strong attractive Coulomb interaction between the localized 4f electrons and the 2p core hole in the final state [218]. These quadrupolar contributions are more pronounced at the L_3 edge than at the L_2 edge. Only for Tb it can be clearly made out also at the L_2 edge. At the L_3 edge it seems to become larger with increasing f-count. The explanation why the quadrupolar peak is negative at the L_3 edge is the following: in general, X-rays with positive helicity generate more spin-up electrons at the L_3 edge, whereas those with negative helicity generate more spin-down electrons. Since all spin-up 4f states are occupied, transitions from 2p to 4f states, i.e. the E2 transitions, occur mainly for negative helicity. Thus, the XMCD of the E2 transitions will be negative.

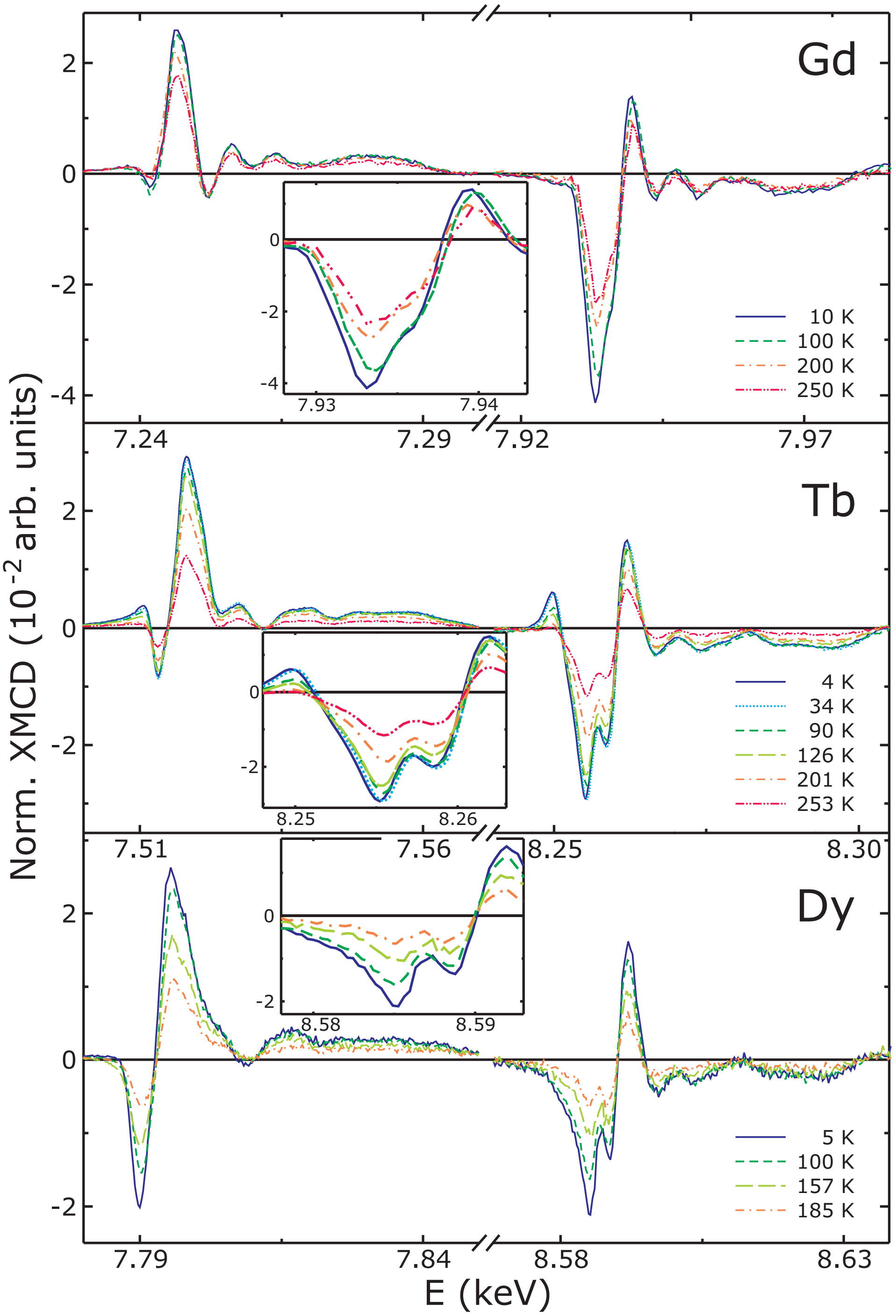

Figure 6.2: Temperature-dependent XMCD at the $L_{2,3}$ edges of Gd, Tb, and Dy. The y-scale is given according to the corresponding XAS which is normalized to unity. To overcome the shape anisotropy and to align the magnetization along the natural direction of easy magnetization, a magnetic field is applied with $\mu_0 H = 7$ T for Tb and $\mu_0 H = 5$ T for Dy at all temperatures. For Gd the field was reduced from $\mu_0 H = 3$ T at $T = 10$ K to $\mu_0 H = 2.8$ T at $T = 100$ K, $\mu_0 H = 2.5$ T at $T = 200$ K, and $\mu_0 H = 2$ T at $T = 250$ K.

Table 6.1: Temperature T_C at which in zero magnetic field Gd undergoes a phase transition FM-PM, Tb and Dy a transition FM-helical. At T_N the magnetic phases of Tb and Dy go from helical to PM. In Tb and Dy the helical phase is suppressed by a magnetic field larger than H_C and a transition FM-PM occurs at T_N [210, 219].

element	T_C	T_N	$\mu_0 H_\mathrm{C}$
Gd	293 K	–	–
Tb	220 K	230 K	< 0.1 T
Dy	88 K	178 K	1.2 T

6.3 Temperature-Dependent XMCD Spectra

After discussing the general features of the XAS and XMCD at low temperature, the focus is now turned to the details in the temperature-dependent XMCD spectra. In Fig. 6.2 the temperature-dependent XMCD of the three elements is plotted. Due to the performance of the beamline the spectra have an excellent signal-to-noise ratio. The high energy resolution allows to identify the detailed spectroscopic features. The spectra have been measured in a range from low temperature T up to the FM-PM transition temperature in each case. These characteristic temperatures as they occur in zero magnetic field are summarized in Table 6.1. In zero magnetic field Tb and Dy show a helical magnetic phase for $T_\mathrm{C} < T < T_\mathrm{N}$. However, since the measurements have been carried out in an applied magnetic field strong enough to overcome the shape anisotropy of the samples, this helical phase is suppressed. For each sample the magnetization as a function of the applied field has been determined before measuring the XMCD. From this, the field strength was chosen such that the samples are magnetically saturated during the XMCD measurements. For Tb it was set to $\mu_0 H = 7$ T, for Dy to $\mu_0 H = 5$ T at all temperatures. In the case of Gd the field was reduced from $\mu_0 H = 3$ T at $T = 10$ K to $\mu_0 H = 2.8$ T at $T = 100$ K, $\mu_0 H = 2.5$ T at $T = 200$ K, and $\mu_0 H = 2$ T at $T = 250$ K. In an applied magnetic field the magnetization vanishes at slightly higher temperatures than given in Table 6.1 [209, 215, 220]. Therefore, XMCD signals are still observed at the highest temperature points given in Fig. 6.2 for Tb and Dy, which are above the transition temperature to the PM phase.

The relative intensities of the different spectral features vary as temperature changes. At different photon energies different temperature dependencies of the XMCD are observed. This becomes obvious especially from the insets that show enlargements of the L_2 edges. Thus, for the rare earth elements, Gd, Tb, and Dy, the temperature dependence is more complex than for the $3d$ FMs. In the cases of Co and Ni, for example, the XMCD scales in intensity with the magnetization as a function of the temperature without changing its line shape. This fact has been exploited to determine the element-specific $M(T)$ of the coupled trilayers in Chapter 5 from a single spectral feature of the XMCD spectrum. The question is, of course, what causes the change of the relative intensities in the XMCD spectra of the rare earth elements. Possibly, the reason lies in a temperature-dependent change of the DOS. Final clarification could result from temperature-dependent calculations of the DOS, which at present cannot be carried out.

6.4 Comparison of Experiment and FEFF Results

To further analyze the measured XMCD spectra at low T calculations within the local spin density functional approximation (LDA) were carried out within this work using the version 8.2 of the FEFF code [130]. The theory allows to "switch on and off" the quadrupolar contributions in addition to the dipolar ones. Taking advantage of this possibility, the E1 and E2 contributions can be separated by the calculations. Since the $4f$ bands are very narrow in energy in the three investigated elements, the default atomic configuration was redefined to "solid state" configuration to help convergence. Dirac-Harra self-energy was used to reproduce the peak separation for both XMCD and XAS. The calculated XMCD spectra are shown in Fig. 6.3 together with the measured ones. The calculated curves are scaled down by a factor in the order of $2-3$ to match the experimental data. To account for the non-self-consistency of the FEFF code with respect to the spin, the energy axes have been adjusted by less than 5 eV in each case. Apart from the fact that the calculated spectra are slightly too broad directly at the edge, they reproduce the fine structure of the experiment quite well. Even the double structure at the L_2 edge of Tb and Dy is resolved. In the case of Gd the higher energy peak of this double structure reduces to a shoulder in the measured spectra. Also in the calculation its intensity is reduced, even though the reduction is less pronounced than in the experiment. The calculations confirm the quadrupolar contributions with opposite sign than the dipolar ones at the low energy side of the edges in all three cases. The E2 contributions can thus be attributed to the corresponding peaks in the measured spectra. At the L_2 edges of Gd and Dy the E2 contribution merges into the onset of the E1 contribution and can hardly be seen by eye from the experiments. Apart from one peak in the pre-edge region, the XMCD of the quadrupolar transitions does

Table 6.2: Crystal parameters of Gd, Tb, and Dy [221].

element	a	b	c
Gd (hcp)	3.63 Å		5.78 Å
Tb (hcp)	3.60 Å		5.70 Å
Tb (cmcm, $T < 220$ K)	3.59 Å	6.26 Å	5.72 Å
Dy (hcp)	3.59 Å		5.65 Å
Dy (cmcm, $T < 86$ K)	3.60 Å	6.18 Å	5.68 Å

not show any further structure. This reflects the fact that the $4f$ states, which are the final states for the E2 transitions, are well localized and have a narrow energy band.

In the calculations of Fig. 6.3 hexagonal-closed-packed (hcp) structures with the parameters listed in Table 6.2 have been assumed. Strictly speaking, these are the crystal structures of bulk Gd, Tb, and Dy at room temperature. For Tb and Dy a structural transition to a orthorhombic structure of the cmcm space group are reported at $T = 220$ K and $T = 86$ K, respectively [219]. These are about the temperatures at which the magnetic phase transition from the helical phase to FM occurs in zero magnetic field. As it is known, for instance, from the ultrathin ferromagnetic films on Cu single crystals, small changes of the nearest neighbor distance by a few hundredth of an ångström may change the magnetic anisotropy dramatically (Chapter 4). The question is to what extent the structural change influences the XMCD spectra. In general, in earlier investigations no structural change at low temperature was considered.

Figure 6.4 shows a comparison of the calculated XMCD of Dy assuming a hcp (solid line) or an orthorhombic (dashed line) structure with the corresponding parameters given in Table 6.4. The calculations assuming hcp structure seem to satisfy the experiments (dotted line) better. Two possible reasons may lead to this finding. (i) The samples are measured in an applied static magnetic field. There are several reports about rather significant magnetostrictive effects in rare earth elements [222, 223]. It is unclear what happens to the crystal structure of the specific samples in the given conditions of the present experiment. Possibly the crystal structure is affected by the large magnetic field. (ii) The FEFF code is based on a LDA procedure which in general is more reliable for delocalized states than for very localized ones probed close to the edge. However, assuming the hcp structure, the calculations yield satisfactory results even close to the edge. In general, FEFF yields best

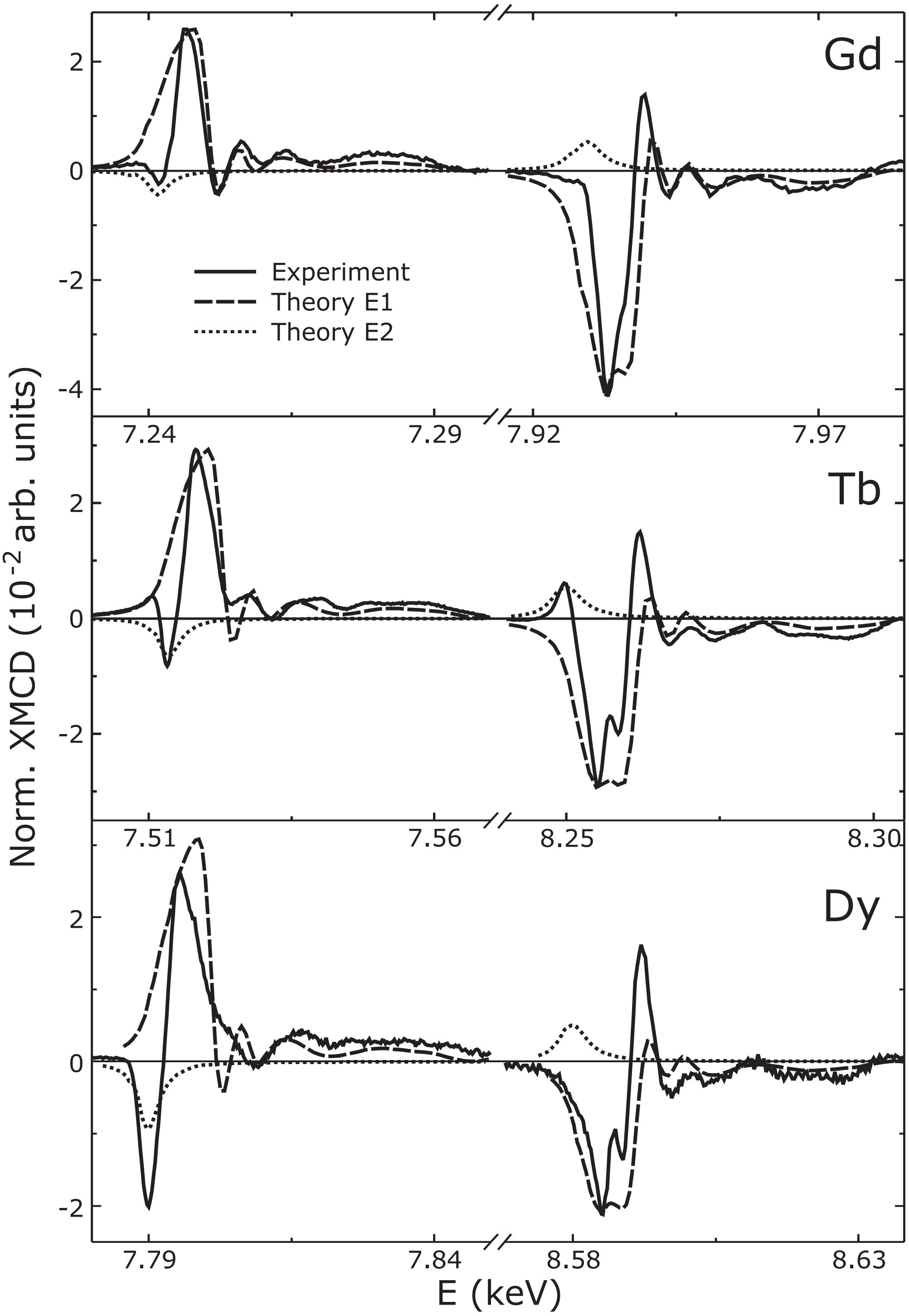

Figure 6.3: Comparison of the measured XMCD spectra of Gd, Tb, and Dy at low temperature to the spectra obtained from FEFF calculations.

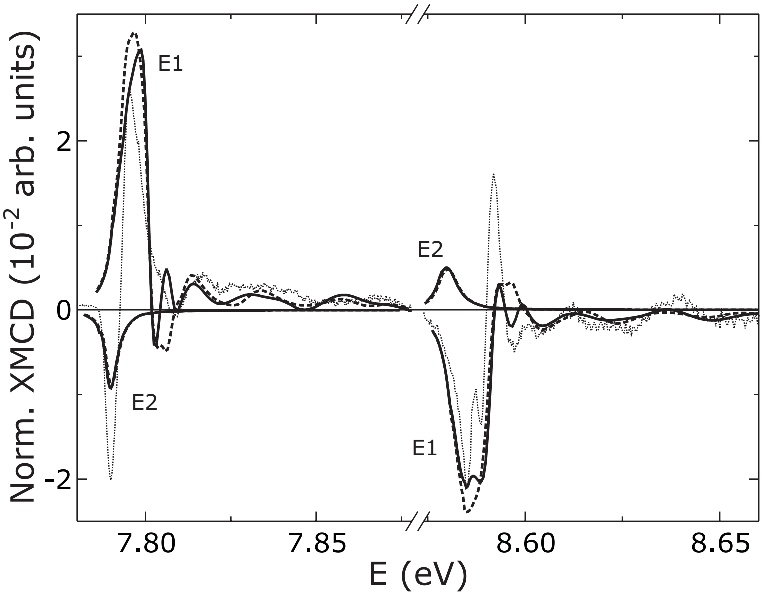

Figure 6.4: Comparison of FEFF results assuming hcp (solid line) or orthorhombic (dashed line) structure for Dy together with the measured spectra (dotted line).

results in the extended energy range where the difference between the calculations for two structures seems to be less pronounced. Especially the E1 contributions are affected by the structural change. Hardly any difference occurs for the E2 contributions. Magnetostriction affects the hybridization between nearest neighbors. This hybridization occurs among the 5d states. Thus, magnetostrictive effects are expected to become obvious in the E1 transitions. Due to their high localization the 4f moments and thus the E2 transitions are not influenced. Detailed analysis and FEFF calculations of the EXAFS would possibly enlighten the crystal structure in the specific samples of the present experiments.

Summarizing, high quality temperature-dependent XMCD spectra have been obtained from measuring single crystals of Gd, Tb, and Dy at their $L_{2,3}$ edges. They have been compared to FEFF calculations to systematically identify the E1 and E2 contributions, which are equally important for transitions at the $L_{2,3}$ edges of the three investigated elements. In the future the spectra should be compared to temperature-dependent calculated spectra, to identify the origin of the temperature dependence of the line shape. However, at present including temperature dependence in the calculations remains a challenge for theory to calculate the experimental spectra.

Chapter 7

Conclusions

In this thesis, XAS and XMCD were applied to study the magnetism of ultrathin ferromagnetic films of Fe, Co, and Ni, and of single crystals of the rare earth elements Gd, Tb, and Dy. In all cases, the experimental results have been compared to theory.

Tailoring the growth of $3d$ ferromagnets by O as a surfactant was exploited to influence their magnetism. Fe, Co, and Ni films were grown with and without O surfactant on single crystalline Cu substrates. At first, the electronic structure has been investigated. NEXAFS spectra, providing a fingerprint of the chemical bond, reveal that no bulk-like oxides with the FMs are formed. The angular dependence of the NEXAFS at the O K edge gives final evidence that the O atoms, which have been initially adsorbed onto the clean Cu surface, float on top as the growth of the FM films proceeds. Choosing Ni as an example, a charge transfer from the $3d$ states of the FM to the $2p$ states of the O has been determined from NEXAFS spectra at the Ni $L_{2,3}$ edges. Taking advantage of the element-specificity of XMCD, not only the influence of the O surfactant on the magnetism of the FMs themselves has been elucidated, but also the induced magnetism of the surfactant O was investigated by XMCD at the O K edge. The magnetic information that can be obtained from XMCD spectra at the O K edge is limited. Due to the missing spin-orbit splitting of the initial $1s$ state, XMCD at K edges yields only information about the orbital magnetism. Therefore, the systematics of the induced magnetism at the O site in surfactant grown samples has been studied for the three FM elements in comparison to *ab initio* calculations. Accompanying calculations reproduce the measured spectra and provide the spin-resolved density of states, the spin moments, and the orbital moments. To study the influence of the O surfactant on the FM layers in detail, Ni was chosen as an example for a series of thickness-dependent measurements. Ni films of different thickness above the SRT, i.e. with an easy axis of magnetization perpendicular to the sample surface, were grown on Cu(100) and Cu(110). The behavior of the total magnetization for the thinnest films is different on the two surfaces. Growing Ni with O surfactant on Cu(100), the total magnetization is reduced below the bulk value whereas on the more open Cu(110) surface it is enhanced. This difference in the magnetic behavior is attributed to a different surface roughness. A detailed analysis with the help of the integral sum rules has shown that this enhancement is mainly caused by the orbital moment of the Ni. In the rougher film the orbital moment of the surface atoms is less quenched because of their reduced effective coordination.

In the second part of this work Co/Cu/Ni/Cu(100) trilayers were chosen as a prototype system to study the influence of the IEC and the importance of enhanced 2D spin fluctuations. Since the two FM layers are of different elements, XMCD is especially suitable to study the magnetic behavior of them separately. The IEC results in a change of the element-specific magnetizations of the FM constituents. In the present study the Ni thickness was reduced down to $\sim$ 2 ML, considerably lower than in earlier investigations. In this very thin thickness range the temperature shift $\Delta T_{\mathrm{C,Ni}}/T_{\mathrm{C,Ni}}$ is most pronounced. It may be up to more than 200 % at $d_{\mathrm{Ni}} \approx 2$ ML. Such an enormous shift of a critical temperature is never attained in bulk material. It is known that a mean field description is insufficient to describe the magnetic behavior of trilayers in the ultrathin limit. Spin-spin correlations (spin fluctuations) have to be taken into account to properly describe the temperature shift $\Delta T_{\mathrm{C,Ni}}/T_{\mathrm{C,Ni}}$. With the help of theory including spin fluctuations it was possible to successfully derive a relation between the shift $\Delta T_{\mathrm{C,Ni}}/T_{\mathrm{C,Ni}}$ and the coupling strength J_{inter}. In contrast to earlier findings in MF, this dependence turns out to be nonlinear. Only with this relation it has become possible to combine the two dependencies $\Delta T_{\mathrm{C,Ni}}/T_{\mathrm{C,Ni}}\,(d_{\mathrm{Ni}})$ and $J_{\mathrm{inter}}\,(d_{\mathrm{Cu}})$ which were always discussed separately in the past. As a result a two-parameter plot (Fig. 5.14) is presented in this thesis. The theoretical curve is well in agreement with the experimental findings.

In connection with the investigations of the trilayer systems, measurements of the total electron yield in an applied magnetic field have been established in the existing UHV chamber. A water-cooled coil system was designed and set into operation in the course of this work. With this new coil system measurements in a static magnetic field $\vec{H}$ of up to $\mu_0 H \approx 50$ mT have become possible.

In the third part of this thesis, the shell selectivity of XMCD was exploited to investigate the interplay between the magnetism of the $5d$ conduction electrons and the localized $4f$ states in rare earth elements. Besides the dipole transitions (E1:

$2p \rightarrow 5d$), quadrupolar transitions (E2: $2p \rightarrow 4f$) are equally important for the X-ray absorption at the $L_{2,3}$ edges of these elements. Due to the states involved, investigations at the $L_{2,3}$ edges reveal information about the two contributions in one single experiment. In contrast to many existing XMCD results on complex compounds, the systematics of the rare earth XMCD was studied on single crystals in the present work. Single crystals do not include additional complex interactions of different species like in a compound. For the series of the rare earth elements Gd, Tb, and Dy high quality temperature-dependent XMCD spectra have been obtained. These spectra contain detailed fine structures in their spectroscopic features. In contrast to the XMCD of the $3d$ FMs, the relative intensities of these features change as a function of the temperature. The low temperature spectra were compared to *ab initio* calculations using the FEFF code. In this framework contributions to the XMCD from dipolar and quadrupolar transitions can be systematically identified. However, it remains a challenge for theory to describe and reproduce the temperature dependence of the spectra.

Concluding, this thesis has shown that by investigating the spin-averaged and spin-dependent X-ray absorption spectra, the delicate interplay of different magnetic contributions, as they are relevant for nanostructures, may be identified and separated. By combining experiment and theory, they lead to an advanced insight into the magnetic properties of the investigated systems.

Appendix A

Note on the Use of Units

Magnetic units are not used consistently in literature. In general, in this thesis the use of the modern SI units is preferred. A magnetic field $\vec{H}$ is characterized by the quantity $\mu_0 H$ given in tesla, which strictly speaking is a magnetic induction B. A magnetic field with $\mu_0 H = 100$ mT in vacuum corresponds to $H = 1$ kOe in the older but still commonly used cgs system. Magnetizations are given in kA/m where 1 kA/m in SI units corresponds to 1 G in cgs units. For atomic distances the convenient unit ångström (1 Å$= 10^{-10}$ m) is used like in many recent publications. The problems that occur due to different unit systems are a man-made and do not influence the physics themselves.

Appendix B

Additional Notes on the New Coil System

B.1 Geometry of the New Coil System with Respect to Helmholtz Geometry

A pair of two identical coils are in Helmholtz geometry if they are separated by a distance equal to their radius. Then the field in a certain area between them is a nearly spatially uniform magnetic field. The radius of the new coil system is $R_i = 18$ mm, the outer radius is $R_a = 65$ mm. Thus the mean radius is $R_m = 41.5$ mm. Their distance is $D = 68$ mm. This means they are further away from each other than in the ideal Helmholtz geometry. However, the calibration measurements (see Chapter 3) show a satisfactory homogeneity of the magnetic field at the sample position.

B.2 Operation of the New Coil System in Pulse Mode

Operation of the system in pulse mode is in general possible with the existing magnetic field pulse generation electronics by sudden discharge of a capacitor. Therefore, one has to be aware that the whole electric system, i.e. the pulse generation electronics together with the coil system, is an RCL oscillator, and in the strongly damped case the condition $(4L) / (CR^2) < 1$ has to be fulfilled. Since the inductance L of the coil system and the capacity C of the electronics are given, the ohmic resistance R has to be adjusted by installing a series resistance R_S in the feed cable. The capacity of the available electronics is $C = 5$ mF. The ohmic resistance R_coil and the inductance L of the new coil system (both coils in series) have been measured. They are $L = (305 \pm 15)\,\mu\mathrm{H}$ and $R_{\mathrm{coil}} = (0.208 \pm 0.006)\,\Omega$. Since also the maximum current is limited by the components of the electronics $R_{\mathrm{S}} = 0.47\,\Omega$ has been chosen for a first test. The maximum current can be obtained from the time dependence of the current $I(t) = C\frac{\mathrm{d}}{\mathrm{d}t}U_C(t)$ which is determined by the voltage $U_C(t)$ of the discharging capacitor. It is given by

$$I(t) = \frac{U_0 \cdot \mathrm{e}^{-\frac{R}{2L}(\gamma-1)t}}{R\gamma} \cdot \left(1 - \mathrm{e}^{-\frac{R}{L}t}\right),\ \gamma = \sqrt{1 - \frac{4L}{CR^2}}\,. \tag{B.1}$$

B.3 Choice of the PTFE Shrink Tube

PTFE shrink tube is used to electrically insulate the Cu tubes. During the construction of the coil system it turned out that PTFE shrink tube is delicate to handle. Therefore, it is useful to buy it directly from a manufacturer, where one has the possibility to get in contact with the corresponding technician. The PTFE shrink tube finally used was bought from IFK-ISOFLUOR GmbH, Neuss (http://www.isofluor.de). The type of the tube is “AWG 11 TW 2:1”. A shrinking rate of 2:1 is preferable. A tube with a shrinking rate of 2:1 ends up tighter on the Cu than a tube which shrinks 4:1.

Bibliography

[1] J. Stöhr: *NEXAFS Spectroscopy.* Vol. 25, Springer, Berlin Heidelberg (1992).

[2] J. Stöhr: *X-ray magnetic ciruclar dichroism spectroscopy of transition metal thin films.* J. Electr. Spectr. and Rel. Phenom. **75**, 253 (1995).

[3] J. Stöhr: *Exploring the microscopic origin of magnetic anisotropies with X-ray magnetic circular dichroism (XMCD) spectroscopy.* J. Magn. Magn. Mat. **200**, 470 (1999).

[4] J. Lindner, P. Poulopoulos, R. Nünthel, E. Kosubek, H. Wende, and K. Baberschke: *Improved growth and the spin reorientation transition of Ni on* $\left(\sqrt{2}\times 2\sqrt{2}\right)R45^\circ$ *reconstructed O/Cu(001).* Surf. Sci. **523**, L65 (2003).

[5] R. Nünthel, T. Gleitsmann, P. Poulopoulos, A. Scherz, J. Lindner, E. Kosubek, Ch. Litwinski, Z. Li, H. Wende, K. Baberschke, S. Stolbov, and T. S. Rahman: *Epitaxial growth of Ni on Cu(001) with the assistance of O-surfactant and its magnetism compared to Ni/Cu(001).* Surf. Sci. **531**, 53 (2003).

[6] J. Hong, R. Q. Wu, J. Lindner, E. Kosubek, and K. Baberschke: *Manipulation of Spin Reorientation Transition by Oxygen Surfactant Growth: A Combined Theoretical and Experimental Approach.* Phys. Rev. Lett. **92**, 147202 (2004).

[7] P. Bruno and C. Chappert: *Oscillatory Coupling between Ferromagnetic Layers Separated by a Nonmagnetic Metal Spacer.* Phys. Rev. Lett. **67**, 1602 (1991).

[8] P. Bruno and C. Chappert: *Oscillatory Coupling between Ferromagnetic Layers Separated by a Nonmagnetic Metal Spacer [Phys. Rev. Lett. 67, 1602 (1991)].* Phys. Rev. Lett. **67**, 2592 (1991).

[9] A. Fert, P. Grünberg, A. Barthélémy, F. Petroff, and W. Zinn: *Layered magnetic structures: interlayer exchange coupling and giant magnetoresistance.* J. Magn. Magn. Mat. **140**, 1 (1995).

[10] B. Heinrich and J. A. C. Bland: *Ultrathin Magnetic Structures II.* Springer, Berlin (1994).

[11] J. A. C. Bland and B. Heinrich: *Ultrathin Magnetic Structures III.* Springer, Berlin (2005).

[12] U. Bovensiepen, F. Wilhelm, P. Srivastava, P. Poulopoulos, M. Farle, A. Ney, and K. Baberschke: *Two Susceptibility Maxima and Element Specific Magnetizations in Indirectly Coupled Ferromagnetic Layers.* Phys. Rev. Lett. **81**, 2368 (1998).

[13] P. Poulopoulos and K. Baberschke: *Phase Transitions in Coupled Two-Dimensional Ferromagnetic Layers.* Lecture Notes in Physics **580**, 283 (2001).

[14] P. J. Jensen, K. H. Bennemann, P. Poulopoulos, M. Farle, F. Wilhelm, and K. Baberschke: *Enhanced induced magnetization in coupled magnetic trilayers in the presence of spin fluctuations.* Phys. Rev. B **60**, R14994 (1999).

[15] J. Lindner and K. Baberschke: *Ferromagnetic resonance in coupled ultrathin films.* J. Phys: Cond. Matter **15**, S465 (2003).

[16] P. Carra and M. Altarelli: *Dichroism in the x-ray absorption spectra of magnetically ordered systems.* Phys. Rev. Lett. **64**, 1286 (1990).

[17] J. C. Lang, G. Srajer, C. Detlefs, A. I. Goldman, H. König, X. Wang, B. N. Harmon, and R. W. McCallum: *Confirmation of Quadrupolar Transitions in Circular Magnetic X-Ray Dichroism at the Dysprosium L_{III} Edge.* Phys. Rev. Lett. **74**, 4935 (1995).

[18] C. Giorgetti, E. Dartyge, C. Brouder, F. Baudelet, C. Meyer, S. Pizzini, A. Fontaine, and R.-M. Galéra: *Quadrupolar Effect in X-Ray Magnetic Circular Dichroism.* Phys. Rev. Lett. **75**, 3186 (1995).

[19] H. Ebert: *Magneto-optical effects in transition metal systems.* Rep. Prog. Phys. **59**, 1665 (1996).

[20] J. L. Erskine and E. A. Stern: *Calculation of the M_{23} magneto-optical absorption spectrum of ferromagnetic nickel.* Phys. Rev. B **12**, 5016 (1975).

[21] G. Schütz, W. Wagner, W. Wilhelm, P. Kienle, R. Zeller, R. Frahm, and G. Materlik: *Absorption of circularly polarized x rays in iron.* Phys. Rev. Lett. **58**, 737 (1987).

[22] B. K. Agarwal: *X-Ray Spectroscopy.* Vol. 15, Springer, Berlin (1979).

[23] A. Scherz: *Spin-dependent X-ray Absorption Spectroscopy of 3d Transition Metals: Systematics and Applications.* Ph. D. thesis, Freie Universität Berlin, Dissertation.de-Verlag im Internet GmbH, Berlin, ISBN 3-89825-779-7 (2004).

[24] A. Scherz, E. K. U. Gross, H. Appel, C. Sorg, K. Baberschke, H. Wende, and K. Burke: *Measuring the kernel of time-dependent density functional theory with x-ray absorption spectroscopy of* 3*d transition metals.* Phys. Rev. Lett. submitted (2005).

[25] C. T. Chen, Y. U. Idzerda, H.-J. Lin, N. V. Smith, G. Meigs, E. Chaban, G. H. Ho, E. Pellegrin, and F. Sette: *Experimental Confirmation of the X-Ray Magnetic Circular Dichroism Sum Rules for Iron and Cobalt.* Phys. Rev. Lett. **75**, 152 (1995).

[26] W. Gudat and C. Kunz: *Close Similarity between Photoelectric Yield and Photoabsorption Spectra in the Soft-X-Ray Range.* Phys. Rev. Lett. **29**, 169 (1972).

[27] W. L. O'Brien and B. P. Tonner: *Orbital and spin sum rules in x-ray magnetic circular dichroism.* Phys. Rev. B **50**, 12672 (1994).

[28] J. Vogel and M. Sacchi: *Polarization and angular dependence of the* $L_{2,3}$ *absorption edges in Ni(110).* Phys. Rev. B **49**, 3230 (1994).

[29] J. Hunter-Dunn, D. Arvanitis, N. Mårtensson, M. Tischer, F. May, M. Russo, and K. Baberschke: *An angle-dependent magnetic circular X-ray dichroism study of Co/Cu(100): experiment versus theory.* J. Phys: Cond. Matter **7**, 1111 (1995).

[30] R. Nakajima, J. Stöhr, and Y. U. Idzerda: *Electron-yield saturation effects in L-edge x-ray magnetic circular dichroism spectra of Fe, Co, and Ni.* Phys. Rev. B **59**, 6421 (1999).

[31] W. L. O'Brien and B. P. Tonner: *Surface-enhanced magnetic moment and ferromagnetic ordering of Mn ultrathin films on fcc Co(001).* Phys. Rev. B **50**, 2963 (1994).

[32] E. Goering, A. Fuss, W. Weber, J. Will, and G. Schütz: *Element specific x-ray magnetic circular dichroism magnetization curves using total electron yield.* J. Appl. Phys. **88**, 5920 (2000).

[33] L. Tröger, D. Arvanitis, K. Baberschke, H. Michaelis, U. Grimm, and E. Zschech: *Full correction of the self-absorption in soft-fluorescence extended x-ray-absorption fine structure.* Phys. Rev. B **46**, 3283 (1992).

[34] S. Eisebitt, T. Böske, J.-E. Rubensson, and W. Eberhardt: *Determination of absorption coefficients for concentrated samples by fluorescence detection.* Phys. Rev. B **47**, 14103 (1993).

[35] H. Wende, Ch. Litwinski, A. Scherz, T. Gleitsmann, Z. Li, C. Sorg, K. Baberschke, A. Ankudinov, J. J. Rehr, and Ch. Jung: *A systematic study of embedded atom EXAFS: the* (2×1) *O/Cu(110) reconstruction as an ideal prototype system.* J. Phys: Cond. Matter **15**, 5197 (2003).

[36] J. J. Rehr and R. C. Albers: *Theoretical approaches to x-ray absorption fine structure.* Rev. Mod. Phys. **72**, 621 (2000).

[37] H. Wende, A. Scherz, C. Sorg, Z. Li, P. Poulopoulos, K. Baberschke, A. Ankudinov, J. J. Rehr, F. Wilhelm, N. Jaouen, A. Rogalev, D. L. Schlagel, and T. A. Lograsso: *Temperature Dependence of Magnetic EXAFS for Rare Earth Elements.* Phys. Scripta **T115**, 600 (2005).

[38] A. L. Ankudinov, J. J. Rehr, H. Wende, and K. Baberschke: *Information in Magnetic EXAFS.* Phys. Scripta **T115**, 651 (2005).

[39] P. Srivastava, L. Lemke, H. Wende, R. Chauvistré, N. Haack, K. Baberschke, J. Hunter-Dunn, D. Arvanitis, N. Mårtensson, A. Ankudinov, and J. J. Rehr: *Magnetic extended x-ray absorption fine structure at the $L_{3,2}$ edges of Fe and Co on Cu(001).* J. Appl. Phys. **83**, 7025 (1998).

[40] H. Wende, J. W. Freeland, V. Chakarian, Y. U. Idzerda, L. Lemke, and K. Baberschke: *Probing local magnetic disorder by investigating spin dependent photoelectron scattering.* J. Appl. Phys. **83**, 7028 (1998).

[41] E. Dartyge, F. Baudelet, C. Brouder, A. Fontaine, C. Giorgetti, J.-P. Kappler, G. Krill, M. F. Lopez, and S. Pizzini: *Hard X-rays magnetic EXAFS.* Physica B **208&209**, 751 (1995).

[42] H. Ebert, V. Popescu, D. Ahlers, G. Schütz, L. Lemke, H. Wende, P. Srivastava, and K. Baberschke: *Theoretical and experimental investigations on the magnetic EXAFS at the K- and $L_{2,3}$-edges of bcc-Fe.* Europhys. Lett. **42**, 295 (1998).

[43] D. Norman, J. Stöhr, R. Jaeger, P. J. Durham, and J. B. Pendry: *Determination of Local Atomic Arrangements at Surfaces from Near-Edge X-Ray-Absorption Fine-Structure Studies: O on Ni(100).* Phys. Rev. Lett. **51**, 2052 (1983).

[44] A. I. Nesvizhskii, A. L. Ankudinov, and J. J. Rehr: *Normalization and convergence of x-ray absorption sum rules.* Phys. Rev. B **63**, 94412 (2001).

[45] E. Hecht: *Optics.* Benjamin Cummings, (2001).

[46] U. Fano: *Spin Orientation of Photoelectrons Ejected by Circularly Polarized Light.* Phys. Rev. **178**, 131 (1969).

[47] B. T. Thole, P. Carra, F. Sette, and G. van der Laan: *X-Ray Circular Dichroism as a Probe of Orbital Magnetism.* Phys. Rev. Lett. **68**, 1943 (1992).

[48] P. Carra, B. T. Thole, M. Altarelli, and X. Wang: *X-Ray Circular Dichroism and Local Magnetic Fields.* Phys. Rev. Lett. **70**, 694 (1993).

[49] A. Scherz, H. Wende, K. Baberschke, J. Minár, D. Benea, and H. Ebert: *Relation between $L_{2,3}$ XMCD and the magnetic ground-state properties for the early 3d element V.* Phys. Rev. B **66**, 184401 (2002).

[50] A. Scherz, H. Wende, C. Sorg, K. Baberschke, J. Minár, D. Benea, and H. Ebert: *Limitations of intergral XMCD sum-rules for the early 3d elements.* Phys. Scripta **T115**, 586 (2005).

[51] M. M. Schwickert, G. Y. Guo, M. A. Tomaz, W. L. O'Brien, and G. R. Harp: *X-ray magnetic linear dichroism in absorption at the L edge of metallic Co, Fe, Cr, and V.* Phys. Rev. B **58**, R4289 (1998).

[52] F. Wilhelm: *Magnetic Properties of Ultrathin Films, Coupled Trilayers and 3d/5d Multilayers studied by X-ray Magnetic Circular Dichroism.* Ph. D. thesis, Freie Universität Berlin, Dissertation.de-Verlag im Internet GmbH, Berlin, ISBN 3-89825-177-2 (2000).

[53] S. S. Dhesi, H. A. Dürr, G. van der Laan, E. Dudzik, and N. B. Brookes: *Electronic and magnetic structure of thin Ni films on Co/Cu(001).* Phys. Rev. B **60**, 12852 (1999).

[54] W. D. Brewer, A. Scherz, C. Sorg, H. Wende, K. Baberschke, P. Bencok, and S. Frota-Pessôa: *Direct Observation of Orbital Magnetism in Cubic Solids.* Phys. Rev. Lett. **93**, 77205 (2004).

[55] J. H. Wu, T. Herrmann, M. Potthoff, and W. Nolting: *Theoretical approach to the Curie temperature shift in FM1/NM/FM2/SUB (ferromagnetic metal 1/nonmagnetic metal/ferromagnetic metal 2/substrate) systems.* J. Phys: Cond. Matter **12**, 2847 (2000).

[56] A. Ney, A. Scherz, P. Poulopoulos, K. Lenz, H. Wende, K. Baberschke, F. Wilhelm, and N. B. Brookes: *Clarification of contesting results for the total magnetic moment of Ni/Cu(001).* Phys. Rev. B **65**, 24411 (2002).

[57] A. Ney, P. Poulopoulos, and K. Baberschke: *Surface and interface magnetic moments of Co/Cu(001).* Europhys. Lett. **54**, 820 (2001).

[58] P. J. Jensen, K. H. Bennemann, K. Baberschke, P. Poulopoulos, and M. Farle: *Magnetization and susceptibility of coupled ferromagnetic trilayers calculated with a Green's function type theory.* J. Appl. Phys. **87**, 6692 (2000).

[59] A. Scherz, C. Sorg, M. Bernien, N. Ponpandian, K. Baberschke, H. Wende, and P. J. Jensen: *Importance of giant spin fluctuations in two-dimensional magnetic trilayers.* Phys. Rev. B **72**, 054447 (2005).

[60] P. J. Jensen: *Rapid evaluation of oscillating lattice sums.* Ann. Physik (Leipzig) **6**, 317 (1997).

[61] P. Poulopoulos and K. Baberschke: *Magnetism in thin films.* J. Phys: Cond. Matter **11**, 9495 (1999).

[62] M. Farle, W. Platow, A. N. Anisimov, P. Poulopoulos, and K. Baberschke: *Anomalous reorientation phase transition of the magnetization in fct Ni/Cu(001).* Phys. Rev. B **56**, 5100 (1997).

[63] S. Schwieger, J. Kienert, and W. Nolting: *Theory of field-induced spin reorientation transition in thin Heisenberg films.* Phys. Rev. B **71**, 024428 (2005).

[64] S. V. Tyablikov: *Methods in the quantum theory of magnetism.* Plenum Press, New York (1967).

[65] A. M. N. Niklasson, B. Johansson, and H. L. Skriver: *Interface magnetism of 3d transition metals.* Phys. Rev. B **59**, 6373 (1999).

[66] H. B. Callen: *Green Function Theory of Ferromagnetism.* Phys. Rev. **130**, 890 (1963).

[67] S. V. Tyablikov: Ukr. Mat. Zh **11**, 287 (1959).

[68] S. Sasaki, K. Miyata, and T. Takada: *A New Undulator for Generating Variably Polarized Radiation.* Jpn. J. Appl. Phys. **31**, L1794 (1992).

[69] H. Winick: *Synchrotron Radiation Research.* Plenum Press, New York (1980).

[70] H. Wiedemann: *Synchrotron Radiation.* Springer, Berlin (2003).

[71] D. H. Tomboulian and P. L. Hartman: *Spectral and Angular Distribution of Ultraviolet Radiation from the 300-MeV Cornell Synchrotron.* Phys. Rev. **102**, 1423 (1956).

[72] S. Sasaki: *Analyses for a planar variably-polarizing undulator.* Nucl. Instrum. Meth. A **347**, 83 (1994).

[73] A. Rogalev, V. Gotte, J. Goulon, C. Gauthier, J. Chavanne, and P. Elleaume: *XAFS and X-MCD spectroscopies with undulator gap scan.* J. Synchrotron Rad. **5**, 989 (1998).

[74] BESSY - Berliner Elektronenspeicherring-Gesellschaft für Synchrotronstrahlung m. b. H., URL: *http://www.bessy.de* (2005).

[75] N. Haack: *NEXAFS-Untersuchungen an adsorbierten Molekülen und dünnen Nickel-Filmen.* Ph. D. thesis, Freie Universität Berlin, unpublished, (1999).

[76] M. Ritter, M. Stindtmann, M. Farle, and K. Baberschke: *Nanostructuring of the Cu(001) surface by ion bombardment: a STM study.* Surf. Sci. **348**, 243 (1996).

[77] R. Nünthel: *Wachstum und Magnetismus dünner 3d Metalle auf Cu-Substraten, Einfluß von O als Surfactant.* Ph. D. thesis, Freie Universität Berlin, Dissertation.de-Verlag im Internet GmbH, Berlin, ISBN 3-89825-826-2 (2004).

[78] M. Bernien: *Spinfluktuationen in gekoppelten, magnetischen Schichten: eine temperaturabhängige Röntgenzirkulardichroismus-Studie.* Diplom thesis, unpublished, Freie Universität Berlin (2004).

[79] K. J. S. Sawhney, F. Senf, M. Scheer, F. Schäfers, J. Bahrdt, A. Gaupp, and W. Gudat: *A novel undulator-based PGM beamline for circularly polarised synchrotron radiation at BESSY II.* Nucl. Instrum. Meth. A **390**, 395 (1997).

[80] R. Follath and F. Senf: *New plane-grating monochromators for third generation synchrotron radiation light sources.* Nucl. Instrum. Meth. A **390**, 388 (1997).

[81] M. R. Weiss, R. Follath, K. J. S. Sawhney, F. Senf, J. Bahrdt, W. Frentrup, A. Gaupp, S. Sasaki, M. Scheer, H.-C. Mertins, D. Abramsohn, F. Schäfers, W. Kuch, and W. Mahler: *The Elliptically Polarised Undulator Beamlines at BESSY II.* Nucl. Instrum. Meth. A **467**, 449 (2001).

[82] A. Scherz: *Magnetischer Röntgenzirkulardichroismus an ultrdünnen magnetischen Filmen der* 3*d Übergangsmetalle Kobalt und Nickel: Temperaturabhängige Messungen an Ein- und Dreischichtsystemen.* Diplom thesis, unpublished, Freie Universität Berlin (2000).

[83] MAX-lab D1011, URL: *http://maxsun5.maxlab.lu.se/beamlines/bld1011/* (2005).

[84] Swagelok company, URL: *http://www.swagelok.com* (corporate office, US), *http://www.swagelok.de* (Germany), (2005).

[85] ESRF - The European Synchtrotron Radiation Facility, URL: *http://www.esrf.fr* (2005).

[86] J. Goulon, A. Rogalev, C. Gauthier, C. Goulon-Ginet, S. Paste, R. Signorato, C. Neumann, L. Varga, and C. Malgrange: *Instrumentation Developments for X-ray Linear and Circular Dichroism at the ESRF Beamline ID12A.* J. Synchrotron Rad. **5**, 232 (1998).

[87] J. Goulon, A. Rogalev, F. Wilhelm, N. Jaouen, C. Goulon-Ginet, and C. Brouder: *Optical activity probed with x-rays.* J. Phys: Cond. Matter **15**, S633 (2003).

[88] J. Chavanne, P. Elleaume, and P. Van Vaerenbergh: *A novel fast switching linear/helical undulator.* in: Proc. 6th EPAC, p. 317 (1998).

[89] C. Gauthier, G. Goujon, S. Feite, E. Moguiline, L. Braicovich, N. B. Brookes, and J. Goulon: *Modulated detection of multibeam dichroism using photodiodes.* Physica B **208&209**, 232 (1995).

[90] O. Hjortstam, K. Baberschke, J. M. Wills, B. Johansson, and O. Eriksson: *Magnetic anisotropy and magnetostriction in tetragonal and cubic Ni.* Phys. Rev. B **55**, 15026 (1997).

[91] L. Li, A. Kida, M. Ohnishi, and M. Matsui: *Surfactant effect of oxygen in epitaxial* γ*-Fe/Cu(001)-O*$\left(2\sqrt{2} \times \sqrt{2}R45°\right)$. Surf. Sci. **493**, 120 (2001).

[92] W. F. Egelhoff, P. J. Chen, C. J. Powell, M. D. Stiles, R. D. McMichael, J. H. Judy, K. Takano, and A. E. Berkowitz: *Oxygen as a surfactant in the growth of giant magnetoresistance spin valves.* J. Appl. Phys. **82**, 6142 (1997).

[93] M. Copel, M. C. Reuter, E. Kaxiras, and R. M. Tromp: *Surfactants in Epitaxial Growth.* Phys. Rev. Lett. **63**, 632 (1989).

[94] J. Camarero, T. Graf, J. J. de Miguel, R. Miranda, W. Kuch, M. Zharnikov, A. Dittschar, C. M. Schneider, and J. Kirschner: *Surfactant-Mediated Modification of the Magnetic Properties of Co/Cu(111) Thin Films and Superlattices.* Phys. Rev. Lett. **76**, 4428 (1996).

[95] L. Duò, R. Bertacco, G. Isella, F. Ciccacci, and M. Richter: *Electronic and magnetic properties of the Co/Fe(001) interface and the role of oxygen.* Phys. Rev. B **61**, 15294 (2000).

[96] F. Bisio, R. Moroni, M. Canepa, L. Mattera, R. Bertacco, and F. Ciccacci: *Structural versus Magnetic Properties at the Surface of Fe Films during Oxygen-Assisted Homoepitaxial Growth.* Phys. Rev. Lett. **83**, 4868 (1999).

[97] M. Nývlt, F. Bisio, J. Franta, C. L. Gao, H. Petek, and J. Kirschner: *Surface Magnetism during Oxygen-Aided Fe Homoepitaxy.* Phys. Rev. Lett. **95**, 127201 (2005).

[98] R. Nünthel, J. Lindner, P. Poulopoulos, and K. Baberschke: *The influence of substrate preoxidation on the growth of Ni on Cu(110).* Surf. Sci. **566-568**, 100 (2004).

[99] C. Sorg, N. Ponpandian, A. Scherz, H. Wende, R. Nünthel, T. Gleitsmann, and K. Baberschke: *The magnetism of ultrathin Ni films grown with O surfactant.* Surf. Sci. **565**, 197 (2004).

[100] M. Farle: *Ferromagnetic Ni monolayers grown with an O surfactant.* Surf. Sci. **575**, 1 (2005).

[101] T. Nakagawa, H. Watanabe, and T. Yokoyama: *Opposite spin reorientation transitions driven by a magnetic orbital moment: Ultrathin Ni films on Cu surfaces.* Phys. Rev. B **71**, 235403 (2005).

[102] K. Baberschke: *The magnetism of nickel monolayers.* Appl. Phys. A **62**, 417 (1996).

[103] W. Platow, U. Bovensiepen, P. Poulopoulos, M. Farle, K. Baberschke, L. Hammer, S. Walter, S. Müller, and K. Heinz: *Structure of ultrathin Ni/Cu(001) films as a function of film thickness, temperature, and magnetic order.* Phys. Rev. B **59**, 12641 (1999).

[104] K. Heinz, S. Müller, and L. Hammer: *Crystallography of ultrathin iron, cobalt and nickel films grown epitaxially on copper.* J. Phys: Cond. Matter **11**, 9437 (1999).

[105] J. Shen, J. Giergiel, and J. Kirschner: *Growth and morphology of Ni/Cu(100) ultrathin films: An in situ study using scanning tunneling microscopy.* Phys. Rev. B **52**, 8454 (1995).

[106] C. Tölkes, R. Struck, R. David, P. Zeppenfeld, and G. Comsa: *Surfactant-Induced Layer-by-Layer Growth on a Highly Anisotropic Substrate: Co/Cu(110).* Phys. Rev. Lett. **80**, 2877 (1998).

[107] C. Tölkes, R. Struck, R. David, P. Zeppenfeld, and G. Comsa: *Preparation of atomically flat Co(110) films on Cu(110).* Appl. Phys. Lett. **73**, 1059 (1998).

[108] J. J. de Miguel, A. Cebollada, J. M. Gallego, S. Ferrer, R. Miranda, C. M. Schneider, P. Bressler, J. Garbe, K. Bethke, and J. Kirschner: *Characterization of the growth processes and magnetic properties of thin ferromagnetic cobalt films on Cu(100).* Surf. Sci. **211-212**, 732 (1989).

[109] J. Thomassen, F. May, B. Feldmann, M. Wuttig, and H. Ibach: *Magnetic live surface layers in Fe/Cu(100).* Phys. Rev. Lett. **69**, 3831 (1992).

[110] S. Müller, P. Bayer, C. Reischl, K. Heinz, B. Feldmann, H. Zillgen, and M. Wuttig: *Structural Instability of Ferromagnetic fcc Fe Films on Cu(100).* Phys. Rev. Lett. **74**, 765 (1995).

[111] B. Schulz and K. Baberschke: *Crossover from in-plane to perpendicular magnetization in ultrathin Ni/Cu(001) films.* Phys. Rev. B **50**, 13467 (1994).

[112] F. Huang, M. T. Kief, G. J. Mankey, and R. F. Willis: *Magnetism in the few-monolayers limit: A surface magneto-optic Kerr-effect study of the magnetic behavior of ultrathin films of Co, Ni, and Co-Ni alloys on Cu(100) and Cu(111).* Phys. Rev. B **49**, 3962 (1994).

[113] M. Sacchi, A. Mirone, and S. Iacobucci: *Soft X-ray resonant magnetic scattering from thin Ni layers on Cu(110).* Surf. Sci. **442**, 349 (1999).

[114] M. Wahl, Th. Herrmann, N. Esser, and W. Richter: *Structure and magneto optical properties of ferromagnetic Ni films grown on Cu(110).* phys. stat. sol. (c) **0**, 3002 (2003).

[115] C. M. Schneider, P. Bressler, P. Schuster, J. Kirschner, J. J. de Miguel, and R. Miranda: *Curie temperature of ultrathin films of fcc-cobalt epitaxially grown on atomically flat Cu(100) surfaces.* Phys. Rev. Lett. **64**, 1059 (1990).

[116] P. Krams, F. Lauks, R. L. Stamps, B. Hillebrands, and G. Güntherodt: *Magnetic anisotropies of ultrathin Co(001) films on Cu(001).* Phys. Rev. Lett. **69**, 3674 (1992).

[117] W. L. Ling, Z. Q. Qiu, O. Takeuchi, D. F. Ogletree, and M. Salmeron: *Effect of oxygen surfactant on the magnetic and structural properties of Co films grown on Cu(110).* Phys. Rev. B **63**, 24408 (2001).

[118] D. Li, M. Freitag, J. Pearson, Z. Q. Qiu, and S. D. Bader: *Magnetic phases of ultrathin Fe grown on Cu(100) as epitaxial wedges.* Phys. Rev. Lett. **72**, 3112 (1994).

[119] T. Kraft, P. M. Marcus, and M. Scheffler: *Atomic and magnetic structure of fcc Fe/Cu(100).* Phys. Rev. B **49**, 11511 (1994).

[120] A. Scherz, H. Wende, and K. Baberschke: *Fine structure of X-ray magnetic circular dichroism for early* 3*d transition metals.* Appl. Phys. A **78**, 843 (2004).

[121] K. Amemiya, T. Yokoyama, Y. Yonamoto, D. Matsumura, and T. Ohta: *O K-edge x-ray magnetic circular dichroism of atomic O adsorbed on an ultrathin Co/Cu(100) film: Comparison with molecular CO on Co/Cu(100).* Phys. Rev. B **64**, 132405 (2001).

[122] T. Yokoyama, K. Amemiya, M. Miyachi, Y. Yonamoto, D. Matsumura, and T. Ohta: *K-edge magnetic circular dichroism of O in CO/Ni/Cu(001): Dependence on substrate magnetic anisotropy and its interpretation.* Phys. Rev. B **62**, 14191 (2000).

[123] K. Amemiya, T. Yokoyama, Y. Yonamoto, M. Miyachi, Y. Kitajima, and T. Ohta: *Observation of O K-Edge X-Ray Magnetic Circular Dichroism of CO Adsorbed on an Ultrathin Co/Cu(001) Film.* Jpn. J. Appl. Phys. **39**, L63 (2000).

[124] H.-Ch. Mertins, S. Valencia, W. Gudat, P. M. Oppeneer, O. Zaharko, and H. Grimmer: *Direct observation of local ferromagnetism on carbon in C/Fe multilayers.* Europhys. Lett. **66**, 743 (2004).

[125] C. Sorg, N. Ponpandian, M. Bernien, K. Baberschke, H. Wende, and R. Q. Wu: *Induced Magnetism of Oxygen in Surfactant Grown Fe, Co, and Ni Monolayers.* Phys. Rev. B submitted (2005).

[126] A. Kirilyuk, J. Giergiel, J. Shen, and J. Kirschner: *Unusual surfactant effect and the stability of pseudomorphic γ-Fe films.* Phys. Rev. B **52**, R11672 (1995).

[127] A. Kirilyuk, J. Giergiel, J. Shen, M. Straub, and J. Kirschner: *Growth of stabilized γ-Fe films and their magnetic properties.* Phys. Rev. B **54**, 1050 (1996).

[128] T. Bernhard, M. Baron, M. Gruyters, and H. Winter: *Surface Structure of Ultrathin Fe Films on Cu(001) Revisited.* Phys. Rev. Lett. **95**, 087601 (2005).

[129] M. Newville, B. Ravel, D. Haskel, J. J. Rehr, E. A. Stern, and Y. Yacoby: *Analysis of multiple-scattering XAFS data using theoretical standards.* Physica B: Condensed Matter **208-209**, 154 (1995).

[130] A. L. Ankudinov, B. Ravel, J. J. Rehr, and S. D. Conradson: *Real-space multiple-scattering calculation and interpretation of x-ray-absorption near-edge structure.* Phys. Rev. B **58**, 7565 (1998).

[131] E. O. F. Zdansky, A. Nilsson, H. Tillborg, O. Björneholm, N. Mårtensson, J. N. Andersen, and R. Nyholm: *Electronic structure of atomic adsorbates from x-ray-absorption spectroscopy: Threshold effects and higher excited states.* Phys. Rev. B **48**, 2632 (1993).

[132] H. Tillborg, A. Nilsson, T. Wiell, N. Wassdahl, N. Mårtensson, and J. Nordgren: *Electronic structure of atomic oxygen adsorbed on Ni(100) and Cu(100) studied by soft-x-ray emission and photoelectron spectroscopies.* Phys. Rev. B **47**, 16464 (1993).

[133] R. W. Godby, G. A. Benesh, R. Haydock, and V. Heine: *Local-orbital analysis of the oxygen-nickel(001) bond from self-consistent electronic structure.* Phys. Rev. B **32**, 655 (1985).

[134] F. May, M. Tischer, D. Arvanitis, M. Russo, J. Hunter-Dunn, H. Henneken, H. Wende, R. Chauvistré, N. Mårtensson, and K. Baberschke: *Modifications of the electronic and magnetic properties of ultrathin Ni/Cu(100) films induced by stepwise oxidation.* Phys. Rev. B **53**, 1076 (1996).

[135] P. Srivastava, N. Haack, H. Wende, R. Chauvistré, and K. Baberschke: *Modifications of the electronic structure of Ni/Cu(001) as a function of the film thickness.* Phys. Rev. B **56**, R4398 (1997).

[136] C.-R. Chang and Y. F. Chiang: *Magnetic surface anisotropy of a spin array.* Phys. Rev. B **48**, 12783 (1993).

[137] J. W. Freeland, K. Bussmann, P. Lubitz, Y. U. Idzerda, and C.-C. Kao: *Probing interfacial and bulk magnetic hysteresis in roughened CoFe thin films.* Appl. Phys. Lett. **73**, 2206 (1998).

[138] E. E. Fullerton, D. M. Kelly, J. Guimpel, I. K. Schuller, and Y. Bruynseraede: *Roughness and giant magnetoresistance in Fe/Cr superlattices.* Phys. Rev. Lett. **68**, 859 (1992).

[139] P. Poulopoulos, J. Lindner, M. Farle, and K. Baberschke: *Changes of magnetic anisotropy due to roughness: a quantitative scanning tunneling microscopy study on Ni/Cu(001).* Surf. Sci. **437**, 277 (1999).

[140] E. Wimmer, H. Krakauer, M. Weinert, and A. J. Freeman: *Full-potential self-consistent linearized-augmented-plane-wave method for calculating the electronic structure of molecules and surfaces: O_2 molecule.* Phys. Rev. B **24**, 864 (1981).

[141] M. Weinert, E. Wimmer, and A. J. Freeman: *Total-energy all-electron density functional method for bulk solids and surfaces.* Phys. Rev. B **26**, 4571 (1982).

[142] L. Hedin and B. I. Lundqvist: *Explicit local exchange-correlation potentials.* J. Phys. C: Solid State Phys. **4**, 2064 (1971).

[143] J. P. Perdew, K. Burke, and M. Ernzerhof: *Generalized Gradient Approximation Made Simple*. Phys. Rev. Lett. **77**, 3865 (1996).

[144] J. P. Perdew, K. Burke, and Y. Wang: *Generalized gradient approximation for the exchange-correlation hole of a many-electron system*. Phys. Rev. B **54**, 16533 (1996).

[145] S. Doniach and M. Sunjic: *Many-electron singularity in X-ray photoemission and X-ray line spectra from metals*. Journal of Physics C: Solid State Physics **3**, 285 (1970).

[146] R. Q. Wu: *Mn Distribution and Spin Polarization in* $Ga_{1-x}Mn_xAs$. Phys. Rev. Lett. **94**, 207201 (2005).

[147] B. Heinrich and J. A. C. Bland: *Ultrathin Magnetic Structures IV*. Springer, Berlin (2005).

[148] H. Wende, C. Sorg, M. Bernien, A. Scherz, P. J. Jensen, N. Ponpandian, and K. Baberschke: *Spin fluctuations in coupled two-dimensional magnetic trilayers*. phys. stat. sol. (c) in press (2005).

[149] U. Bovensiepen, P. Poulopoulos, M. Farle, and K. Baberschke: *The Curie temperature in ultrathin Ni/Cu(001) films determined by ac susceptibility and MOKE*. Surf. Sci. **402-404**, 396 (1998).

[150] P. Bruno: *Theory of interlayer magnetic coupling*. Phys. Rev. B **52**, 411 (1995).

[151] P. Bruno: *Interlayer exchange coupling: Preasymptotic corrections*. Eur. Phys. J. B **11**, 83 (1999).

[152] R. Hammerling, J. Zabloudil, P. Weinberger, J. Lindner, E. Kosubek, R. Nünthel, and K. Baberschke: *Interlayer exchange coupling and magnetic anisotropy in prototype trilayers: Ab initio theory versus experiment*. Phys. Rev. B **68**, 92406 (2003).

[153] A. Ney, F. Wilhelm, M. Farle, P. Poulopoulos, P. Srivastava, and K. Baberschke: *Oscillations of the Curie temperature and interlayer exchange coupling in magnetic trilayers*. Phys. Rev. B **59**, R3938 (1999).

[154] G. Bayreuther, F. Bensch, and V. Kottler: *Quantum oscillations of properties in magnetic multilayers*. J. Appl. Phys. **79**, 4509 (1996).

[155] P. Grünberg, R. Schreiber, Y. Pang, M. B. Brodsky, and H. Sowers: *Layered Magnetic Structures: Evidence for Antiferromagnetic Coupling of Fe Layers across Cr Interlayers*. Phys. Rev. Lett. **57**, 2442 (1986).

[156] S. S. P. Parkin: *Systematic Variation of the Strength and Oscillation Period of Indirect Magnetic Exchange Coupling through the* 3d*,* 4d*, and* 5d *Transition Metals*. Phys. Rev. Lett. **67**, 3598 (1991).

[157] V. Leiner, K. Westerholt, A. M. Blixt, H. Zabel, and B. Hjörvarsson: *Magnetic Superlattices with Variable Interlayer Exchange Coupling: A New Approach for the Investigation of Low-Dimensional Magnetism*. Phys. Rev. Lett. **91**, 37202 (2003).

[158] J. Lindner, E. Kosubek, P. Poulopoulos, K. Baberschke, and B. Heinrich: *Interlayer exchange coupling: an in situ investigation via ferromagnetic resonance*. J. Magn. Magn. Mat. **240**, 220 (2002).

[159] J. Lindner, Z. Kollonitsch, E. Kosubek, M. Farle, and K. Baberschke: *In situ detection of two ferromagnetic resonance modes in coupled Ni/Cu/Co/Cu(001) trilayer structures*. Phys. Rev. B **63**, 94413 (2001).

[160] J. Lindner and K. Baberschke: *In situ ferromagnetic resonance: an ultimate tool to investigate the coupling in ultrathin magnetic films*. J. Phys: Cond. Matter **15**, R193 (2003).

[161] Z. Zhang, L. Zhou, P. E. Wigen, and K. Ounadjela: *Using Ferromagnetic Resonance as a Sensitive Method to Study Temperature Dependence of Interlayer Exchange Coupling*. Phys. Rev. Lett. **73**, 336 (1994).

[162] J. Lindner, C. Rüdt, E. Kosubek, P. Poulopoulos, K. Baberschke, P. Blomquist, R. Wäppling, and D. L. Mills: $T^{3/2}$ *Dependence of the Interlayer Exchange Coupling in Ferromagnetic Multilayers*. Phys. Rev. Lett. **88**, 167206 (2002).

[163] S. Schwieger and W. Nolting: *Origin of the temperature dependence of interlayer exchange coupling in metallic trilayers*. Phys. Rev. B **69**, 224413 (2004).

[164] S. Schwieger, J. Kienert, and W. Nolting: *Temperature dependence of interlayer exchange coupling: Spin waves versus spacer effects*. Phys. Rev. B **71**, 174441 (2005).

[165] K. Lenz, T. Toliński, J. Lindner, E. Kosubek, and K. Baberschke: *Evidence of spin-pumping effect in the ferromagnetic resonance of coupled trilayers*. Phys. Rev. B **69**, 144422 (2004).

[166] T. Toliński, K. Lenz, J. Lindner, E. Kosubek, C. Sorg, M. Bernien, A. Scherz, H. Wende, and K. Baberschke: *Interlayer exchange coupling and damping processes in coupled trilayer systems*. **40**, 164 (2004).

[167] W. Weber, R. Allenspach, and A. Bischof: *Exchange Coupling across Cu(100): A High-Precision Study*. Europhys. Lett. **31**, 491 (1995).

[168] J. Unguris, R. J. Celotta, and D. T. Pierce: *Oscillatory exchange coupling in Fe/Au/Fe(100)*. J. Appl. Phys. **75**, 6437 (1994).

[169] J. Unguris, R. J. Celotta, and D. T. Pierce: *Determination of the Exchange Coupling Strengths for Fe/Au/Fe*. Phys. Rev. Lett. **79**, 2734 (1997).

[170] W. Kuch, X. Gao, and J. Kirschner: *Competition between in-plane and out-of-plane magnetization in exchange-coupled magnetic films.* Phys. Rev. B **65**, 64406 (2002).

[171] W. Kuch: *Layer-resolved microscopy of magnetic domains in multi-layered systems.* Appl. Phys. A **76**, 665 (2003).

[172] K. Lenz, E. Kosubek, T. Toliński, J. Lindner, and K. Baberschke: *In situ ferromagnetic resonance in coupled ultrathin trilayers with perpendicularly oriented easy axes.* J. Phys: Cond. Matter **15**, 7175 (2003).

[173] K. Lenz, T. Toliński, E. Kosubek, J. Lindner, and K. Baberschke: *Oscillations of the interlayer exchange coupling in trilayers with non-collinear easy axes.* phys. stat. sol. (c) **1**, 3260 (2004).

[174] J. Wu, G. S. Dong, and X. Jin: *Temperature-dependent magnetization in a ferromagnetic bilayer consisting of two materials with different Curie temperatures.* Phys. Rev. B **70**, 212406 (2004).

[175] P. Srivastava, F. Wilhelm, A. Ney, M. Farle, H. Wende, N. Haack, G. Ceballos, and K. Baberschke: *Magnetic moments and Curie temperatures of Ni and Co thin films and coupled trilayers.* Phys. Rev. B **58**, 5701 (1998).

[176] F. May, T. Tischer, D. Arvanitis, J. Hunter Dunn, H. Henneken, H. Wende, R. Chauvistré, and K. Baberschke: *Magnetic Coupling of Ni, Cu and Co Bi- and Trilayers Probed by Magnetic Circular X-ray Dichroism.* J. Phys. IV France **7**, C2-389 (1997).

[177] F. Wilhelm, P. Srivastava, A. Ney, N. Haack, G. Ceballos, M. Farle, and K. Baberschke: *Influence of exchange coupling on the Ni magnetization in Co/Cu/Ni trilayers.* J. Magn. Magn. Mat. **198-199**, 458 (1999).

[178] F. May, P. Srivastava, M. Farle, U. Bovensiepen, H. Wende, R. Chauvistré, and K. Baberschke: *Element-specific Curie temperatures of Ni/Cu/Co trilayers.* J. Magn. Magn. Mat. **177-181**, 1220 (1998).

[179] C. Sorg, A. Scherz, H. Wende, T. Gleitsmann, Z. Li, S. Rüttinger, Ch. Litwinski, and K. Baberschke: *Co/Cu/Ni trilayers near their Curie temperature studied by XMCD.* Phys. Scripta **T115**, 638 (2005).

[180] P. J. Jensen, C. Sorg, A. Scherz, M. Bernien, K. Baberschke, and H. Wende: *Comment on "‘Magnetic Phase Transition in Co/Cu/Ni/Cu(100) and Co/Fe/Ni/Cu(100)’".* Phys. Rev. Lett. **94**, 039703 (2005).

[181] A. Scherz, F. Wilhelm, U. Bovensiepen, P. Poulopoulos, H. Wende, and K. Baberschke: *Separate Curie temperatures in magnetic trilayers and the effect of spin fluctuations.* J. Magn. Magn. Mat. **236**, 1 (2001).

[182] A. Scherz, F. Wilhelm, P. Poulopoulos, H. Wende, and K. Baberschke: *Element-specific magnetization curves and crossover in Co/Cu/Ni/Cu(001) trilayers studied by XMCD.* J. Synchrotron Rad. **8**, 472 (2001).

[183] C. Won, Y. Z. Wu, A. Scholl, A. Doran, N. Kurahashi, H. W. Zhao, and Z. Q. Qiu: *Magnetic Phase Transition in Co/Cu/Ni/Cu(100) and Co/Fe/Ni/Cu(100).* Phys. Rev. Lett. **91**, 147202 (2003).

[184] P. Poulopoulos, U. Bovensiepen, M. Farle, and K. Baberschke: *AC susceptibility: a sensitive probe of interlayer coupling.* J. Magn. Magn. Mat. **212**, 17 (2000).

[185] U. Bovensiepen, F. Wilhelm, P. Srivastava, P. Poulopoulos, M. Farle, and K. Baberschke: *Do Exchange Coupled Ferromagnetic Monolayers Show Different Curie Temperatures?.* phys. stat. sol. (a) **173**, 153 (1999).

[186] L. Bergqvist and O. Eriksson, private communication.

[187] R. W. Wang and D. L. Mills: *Onset of long-range order in superlattices: Mean-field theory.* Phys. Rev. B **46**, 11681 (1992).

[188] R. B. Griffiths: *Rigorous Results and Theorems.* in: Phase Transition and Critical Phenomena, edited by C. Domb and M. S. Green, Academic Press (1972).

[189] R. Allenspach: *Ultrathin films: magnetism on the microscopic scale.* J. Magn. Magn. Mat. **129**, 160 (1994).

[190] R. Ramchal, A. K. Schmid, M. Farle, and H. Poppa: *Magnetic domain-wall structure in Ni/Cu(001) films imaged by spin-polarized low-energy electron microscopy.* Phys. Rev. B **68**, 54418 (2003).

[191] D. Kerkmann, D. Pescia, and R. Allenspach: *Two-Dimensional Magnet at Curie Temperature: Epitaxial Layers of Co on Cu(100).* Phys. Rev. Lett. **68**, 686 (1992).

[192] E. I. Isaev, L. V. Pourovskii, A. M. N. Niklasson, Yu. Kh. Vekilov, Johansson. B., and I. A. Abrikosov: *Magnetic properties of a Co/Cu/Ni trilayer on the Cu(100) surface.* Phys. Rev. B **65**, 024435 (2001).

[193] C. H. Back, Ch. Würsch, A. Vaterlaus, U. Ramsperger, U. Maier, and D. Pescia: *Experimental confirmation of universality for a phase transition in two dimensions.* Nature **378**, 597 (1995).

[194] C. Won, Y.Z. Wu, N. Kurahashi, H. W. Zhao, and Z. Q. Qiu: *Won et al. Reply.* Phys. Rev. Lett. **94**, 039704 (2005).

[195] P. Poulopoulos, M. Farle, U. Bovensiepen, and K. Baberschke: *Evidence for domain formation near the Curie temperature in ultrathin Ni/Cu(001) films with perpendicular anisotropy.* Phys. Rev. B **55**, R11961 (1997).

[196] H. E. Stanley: *Introduction to Phase Transitions and Critical Phenomena.* Oxford Clarendon Press, (1971).

[197] F. Wilhelm, U. Bovensiepen, A. Scherz, P. Poulopoulos, A. Ney, H. Wende, G. Ceballos, and K. Baberschke: *Manipulation of the Curie temperature and the magnetic moments of ultrathin Ni and Co films by Cu-capping.* J. Magn. Magn. Mat. **222**, 163 (2000).

[198] M. Donath, D. Scholl, H. C. Siegmann, and E. Kay: *Quasi-two-dimensional ferromagnetism in polycrystalline Fe.* Phys. Rev. B **43**, 3164 (1991).

[199] P. J. H. Bloemen, M. T. Johnson, M. T. H. van de Vorst, R. Coehoorn, J. J. de Vries, R. Jungblut, J. Aan de Stegge, A. Reinders, and W. J. M. de Jonge: *Magnetic layer thickness dependence of the interlayer exchange coupling in (001) Co/Cu/Co.* Phys. Rev. Lett. **72**, 764 (1994).

[200] J. Kudrnovský, V. Drchal, I. Turek, M. Šob, and P. Weinberger: *Interlayer magnetic coupling: Effect of interface roughness.* Phys. Rev. B **53**, 5125 (1996).

[201] M. Pajda, J. Kudrnovský, I. Turek, V. Drchal, and P. Bruno: *Oscillatory Curie Temperature of Two-Dimensional Ferromagnets.* Phys. Rev. Lett. **85**, 5424 (2000).

[202] C. Rüdt, A. Scherz, and K. Baberschke: *Oscillatory Curie temperature in ultrathin ferromagnets: experimental evidence.* J. Magn. Magn. Mat. **285**, 95 (2005).

[203] P. Henelius, P. Fröbrich, P. J. Kuntz, C. Timm, and P. J. Jensen: *Quantum Monte Carlo simulation of thin magnetic films.* Phys. Rev. B **66**, 094407 (2002).

[204] B. N. Harmon and A. J. Freeman: *Spin-polarized energy-band structure, conduction-electron polarization, spin densities, and the neutron magnetic form factor of ferromagnetic gadolinium.* Phys. Rev. B **10**, 1979 (1974).

[205] G. Schütz, M. Knülle, R. Wienke, W. Wilhelm, W. Wagner, P. Kienle, and R. Frahm: *Spin-dependent photoabsorption at the L-edges of ferromagnetic Gd and Tb metal.* Z. Phys. B **73**, 67 (1988).

[206] R. M. Galéra and A. Rogalev: *Hard x-ray magnetic circular dichroism in* $GdNi_5$ *and* $TbNi_5$ *single crystals.* J. Appl. Phys. **85**, 4889 (1999).

[207] F. Garcia, L. C. Sampaio, A. Y. Takeuchi, H. Tolentino, and A. Fontaine: *X-ray magnetic circular dichroism temperature dependent study of* RCo_2 *compounds.* J. Appl. Phys. **87**, 5881 (2000).

[208] J. B. Goedkoop, J. C. Fuggle, B. T. Thole, G. van der Laan, and G. A. Sawatzky: *Magnetic x-ray dichroism of rare-earth materials.* J. Appl. Phys. **64**, 5595 (1988).

[209] D. E. Hegland, S. Legvold, and F. H. Spedding: *Magnetization and Electrical Resistivity of Terbium Single Crystals.* Phys. Rev. **131**, 158 (1963).

[210] D. R. Lide: *CRC Handbook of Chemistry and Physics.* CRC Press, Boca Raton (1995).

[211] W. E. Corner and B. K. Tanner: *The easy direction of magnetization in gadolinium.* J. Phys. C: Solid State Phys. **9**, 627 (1975).

[212] H. Wende: *Extended X-ray Absorption Fine Structure Spectroscopy of Surfaces and Thin Films: Local Structure, Dynamic and Magnetic Properties.* Ph. D. thesis, Freie Universität Berlin, Verlag Dr. Köster, Berlin, ISBN ISBN 3-89574-341-0 (1999).

[213] H. Wende: *Recent advances in x-ray absorption spectroscopy.* Rep. Prog. Phys. **67**, 2105 (2004).

[214] L. W. Roeland, G. J. Cock, F. A. Muller, A. C. Moleman, K. A. McEwen, R. G. Jordan, and D. W. Jones: *Conduction electron polarization of gadolinium metal.* J. Phys. F: Met. Phys. **5**, L233 (1975).

[215] D. R. Behrendt, S. Legvold, and F. H. Spedding: *Magnetic Properties of Dysprosium Single Crystals.* Phys. Rev. **109**, 1544 (1958).

[216] A. L. Ankudinov, J. J. Rehr, H. Wende, A. Scherz, and K. Baberschke: *Spin-dependent sum rules for X-ray absorption spectra.* Europhys. Lett. **66**, 441 (2004).

[217] X. Wang, T. C. Leung, B. N. Harmon, and P. Carra: *Circular magnetic x-ray dichroism in the heavy rare-earth metals.* Phys. Rev. B **47**, 9087 (1993).

[218] P. Carra, B. N. Harmon, B. T. Thole, M. Altarelli, and G. A. Sawatzky: *Magnetic x-ray dichroism in gadolinium metal.* Phys. Rev. Lett. **66**, 2495 (1991).

[219] Landolt-Börnstein: *Numerical data and functional relationships in science and technology.* Vol. III/19d1, Springer, Berlin (1991).

[220] H. E. Nigh, S. Legvold, and F. H. Spedding: *Magnetization and Electrical Resistivity of Gadolinium Single Crystals.* Phys. Rev. **132**, 1092 (1963).

[221] Landolt-Börnstein: *Numerical data and functional relationships in science and technology.* Vol. III/6, Springer, Berlin (1991).

[222] F. J. Darnell: *Temperature Dependence of Lattice Parameters for Gd, Dy, and Ho.* Phys. Rev. **130**, 1825 (1963).

[223] F. J. Darnell: *Lattice Parameters of Terbium and Erbium at Low Temperatures.* Phys. Rev. **132**, 1098 (1963).

List of Acronyms and Symbols

2D	two-dimensional
ΔA_2, ΔA_3	integrated area of the XMCD at the L_2, L_3 edge
μ	absorption coefficient
φ	angle between photon wave vector and surface of the sample
ϑ	angle between photon wave vector and magnetization of the sample
A_2, A_3	integrated area of the isotropic XAS at the L_2, L_3 edge
AES	Auger electron spectroscopy
AFM	antiferromagnet
AXAFS	atomic extended X-ray absorption fine structure
BESSY	Berliner Elektronenspeicherring-Gesellschaft für Synchrotronstrahlung m. b. H.
bcc	body centered cubic
CMA	cylindrical mirror analyzer
d	thickness
d_{Co}, d_{Cu}, d_{Ni}	thickness of the Co, Cu, Ni layer in a Co/Cu/Ni trilayer
DOS	density of states
E	photon energy
E_F	Fermi energy
ESRF	European Synchrotron Radiation Facility
EXAFS	extended X-ray absorption fine structure
fcc	face centered cubic
fct	face centered tetragonal
FM	ferromagnet
FMR	ferromagnetic resonance
FY	fluorescence yield
GFT	Green's functions theory
GGA	generalized gradient approximation
hcp	hexagonal closed packed
IEC	interlayer exchange coupling
J_{inter}	strength of the IEC

J_{Co}	intra-layer coupling of Co
$J_{\mathrm{Ni}}^{\mathrm{interface}}$	intra-layer coupling of the Ni interface layer
$J_{\mathrm{Ni}}^{\mathrm{interior}}$	intra-layer coupling of the inner Ni layers
LDA	local density approximation
LEED	low energy electron diffraction
M	magnetization
m_L	orbital magnetic moment
m_S	spin magnetic moment
m_S^{eff}	effective spin moment including $\langle T_z \rangle$-term
M_{Ni}	magnetization of the Ni in a Co/Cu/Ni trilayer
MAE	magnetic anisotropy energy
MEXAFS	magnetic EXAFS
MF(T)	mean field (theory)
ML	monolayer(s)
MEED	medium energy electron diffraction
MOKE	magneto-optic Kerr-effect
n_h	number of holes
NEXAFS	near edge X-ray absorption fine structure
NM	nonmagnet
P_c	degree of circular polarization
PGM	plane grating monochromator
PM	paramagnet
RPA	random phase approximation
SEXAFS	surface EXAFS
SQUID	superconducting quantum interference device
STM	scanning tunneling microscope
T	temperature
T_{C}	Curie temperature
$T_{\mathrm{C,Co}}$, $T_{\mathrm{C,Ni}}$	Curie temperature of a single Co, Ni film
$T_{\mathrm{C,Co}}^{*}$, $T_{\mathrm{C,Ni}}^{*}$	quasi-critical temperature of Co, Ni in a Co/Cu/Ni trilayer
TEY	total electron yield
UHV	ultra high vacuum
VSM	vibrating sample magnetometer
XAS	X-ray absorption spectroscopy
XMCD	X-ray magnetic circular dichroism

List of Publications and Contributions to Conferences

I. Refereed Publications

1. H. Wende, Ch. Litwinski, A. Scherz, T. Gleitsmann, Z. Li, C. Sorg, K. Baberschke, A. Ankudinov, J. J. Rehr, and Ch. Jung
   A systematic study of embedded atom EXAFS: The (2×1)O/Cu(110) reconstruction as an ideal prototype system
   J. Phys.: Condens. Matter **15**, 5197 (2003).

2. A. Scherz, H. Wende, C. Sorg, K. Baberschke, J. Minàr, D. Benea, and H. Ebert
   Limitations of intergral XMCD sum-rules for the early 3d elements
   Conference Proceedings XAFS XII, Malmö Sweden, June 2003,
   Physica Scripta **T115**, 586 (2005).

3. C. Sorg, A. Scherz, H. Wende, T. Gleitsmann, Ch. Litwinski, S. Rüttinger, Z. Li, and K. Baberschke
   Co/Cu/Ni trilayers near their Curie temperature studied by XMCD
   Conference Proceedings XAFS XII, Malmö Sweden, June 2003,
   Physica Scripta **T115**, 638 (2005).

4. H. Wende, A. Scherz, C. Sorg, Z. Li, P. Poulopoulos, K. Baberschke, A. Ankudinov, J. J. Rehr, F. Wilhelm, N. Jaouen, A. Rogalev, D. L. Schlagel, and T. A. Lograsso
   Temperature dependence of magnetic EXAFS for rare earth elements
   Conference Proceedings XAFS XII, Malmö Sweden, June 2003,
   Physica Scripta **T115**, 600 (2005).

5. W. D. Brewer, A. Scherz, C. Sorg, H. Wende, K. Baberschke, P. Bencok, and S. Frota-Pessóa

Direct Observation of Orbital Magnetism in Cubic Solids
Phys. Rev. Lett. **93**, 077205 (2004).

6. C. Sorg, N. Ponpandian, A. Scherz, H. Wende, R. Nünthel, T. Gleitsmann, and K. Baberschke
The magnetism of ultrathin Ni films grown with O surfactant
Surf. Sci. **565**, 197 (2004).

7. T. Toliński, K. Lenz, J. Lindner, E. Kosubek, C. Sorg, M. Bernien, A. Scherz, H. Wende, and K. Baberschke
Interlayer exchange coupling and damping processes in coupled trilayer systems
School on nanostructured systems, Będlewo Poland, September 2003,
Molecular Physics Reports **40**, 164 (2004).

8. P. J. Jensen, C. Sorg, A. Scherz, M. Bernien, K. Baberschke, and H. Wende
Comment on "Magnetic phase transition in Co/Cu/Ni/Cu(100) and Co/Fe/Ni/Cu(100)" February 26, 2004
Phys. Rev. Lett. **94**, 039703 (2005).

9. A. Scherz, C. Sorg, M. Bernien, N. Ponpandian, K. Baberschke, H. Wende, and P. J. Jensen
Importance of giant spin fluctuations in coupled magnetic trilayers
Phys. Rev. B **72**, 054447 (2005).

10. H. Wende, C. Sorg, M. Bernien, A. Scherz, P. J. Jensen, N. Ponpandian, and K. Baberschke
Spin fluctuations in coupled two-dimensional magnetic trilayers
Conference Proceedings Physics of Magnetism, Poznań Poland, June 2005
Phys. Stat. Sol. (b) **243**, 165 (2006).

11. A. Scherz, E. K. U. Gross, H. Appel, C. Sorg, K. Baberschke, H. Wende, and K. Burke
Measuring the kernel of time-dependent density functional theory with X-ray absorption spectroscopy of 3d *transition metals*
Phys. Rev. Lett. **95**, 253006 (2005).

12. C. Sorg, N. Ponpandian, M. Bernien, K. Baberschke, H. Wende, and R. Q. Wu
Induced Magnetism of Oxygen in Surfactant Grown Fe, Co, and Ni Monolayers
Phys. Rev. B **73**, 064409 (2006).

II. Highlights and Annual Reports of Synchrotron Facilities

1. A. Scherz, H. Wende, C. Sorg, K. Baberschke, J. Minár, D. Benea, and H. Ebert
   New concept to study magnetic behavior of early 3d elements
   BESSY – Highlights, p. 8 (2002).

2. H. Wende, A. Scherz, G. Ceballos, C. Sorg, K. Baberschke, A. Ankudinov, J.J. Rehr, F. Wilhelm, A. Rogalev, D.L. Schlagel, and T.A. Lograsso
   Quadrupolar and Dipolar Contributions to XMCD at the Tb $L_{3,2}$*-edges: Experiment versus Theory*
   ESRF – Highlights, p. 84 (2003).

3. W. D. Brewer, A. Scherz, C. Sorg, H. Wende, K. Baberschke, P. Bencok, and S. Frota-Pessóa
   Direct Observation of Orbital Magnetism in Cubic Solids
   ESRF - Highlights, p. 96 (2004).

4. T. Gleitsmann, A. Scherz, Ch. Litwinski, C. Sorg, Z. Li, H. Wende, and K. Baberschke
   NEXAFS investigation of ultrathin Ni films grown on oxygen induced reconstructed $\left(\sqrt{2}\times 2\sqrt{2}\right) R45^\circ$ *O/Cu(001)*
   Annual report BESSY (2002).

5. C. Sorg, A. Scherz, H. Wende, M. Bernien, T. Gleitsmann, Z. Li, S. Rüttinger, Ch. Litwinski, and K. Baberschke
   Co/Cu/Ni trilayers close to their Curie temperature: An XMCD study
   Annual report BESSY (2003).

6. H. Wende, Ch. Litwinski, A. Scherz, T. Gleitsman, Z. Li, C. Sorg, K. Baberschke, A. Ankudinov, J. J. Rehr, and Ch. Jung
   A systematic study of embedded atom EXAFS: the (2×1)*O/Cu(110) reconstruction as an ideal prototype system*
   Annual report BESSY (2003).

7. C. Sorg, N. Ponpandian, A. Scherz, M. Bernien, R. Nünthel, T. Gleitsmann, K. Baberschke, and H. Wende
   NEXAFS and XMCD of ultrathin Ni films grown with O surfactant
   Annual report BESSY (2004).

III. Contributions to Conferences and Workshops

1. Poster, 12th International Conference on X-ray Absorption Fine Structure, (XAFS XII) *Co/Cu/Ni trilayers near their Curie temperature studied by XMCD* Malmö, Sweden (June 2003).

2. Poster, International Workshop on X-Ray Spectroscopies of Magnetic Solids (XRMS-2003)
   Co/Cu/Ni trilayers close their Curie temperatures: An XMCD study
   Berlin, Germany (December 2003).

3. Talk, Frühjahrstagung des Arbeitskreises Festkörperphysik (AKF) der DPG
   Co/Cu/Ni-Dreilagen nahe ihrer Curie-Temperaturen: Untersuchungen mittels magnetischem Röntgenzirkulardichroismus
   Regensburg, Germany (March 2004).

4. Poster, 338th Wilhelm and Else Heraeus Seminar "'Nanomagnetism: New Insights with Synchrotron Radiation"'
   The influence of O surfactant growth on the magnetism of ultrathin Ni films
   Physikzentrum Bad Honnef, Germany (January 2005).

5. Talk, 69. Jahrestagung der Deutschen Physikalischen Gesellschaft
   Ultrathin Ni films grown with O surfactant: Structure and Magnetism
   Berlin, Germany (March 2005).

6. Talk, 23rd European Conference on Surface Science (ECOSS 23)
   Spin fluctuations in two-dimensional coupled ferromagnetic films
   Berlin, Germany (September 2005).

Curriculum Vitae

I. Personal Data

Name:	Claudia Sorg
Nationality:	German
Place and Date of Birth:	Bad Vilbel, Germany, January 12th, 1977
Permanent Address:	Freie Universität Berlin Institut für Experimentalphysik Arnimallee 14 D-14195 Berlin Germany phone: ++49-30-838 56144 fax: ++49-30-838 53646 email: csorg@zedat.fu-berlin.de

II. Educational Qualifications and Research Experience

1983 to 1989	Ernst-Reuter-Schule, Bad Vilbel
1989 to 1996	Georg-Büchner-Gymnasium, Bad Vilbel
October 1993 to December 1993	Lycée Banville, Moulins, France
June 1996	Abitur
October 1996 to December 2001	Studies of physics at the Johann Wolfgang Goethe-Universität, Frankfurt (Main)

August 1998	Diplom-Vorprüfung in physics
August 1998 to August 2001	User support at the computer center of the J. W. Goethe-Universität
September 1999 to July 2001	Diploma thesis *Ladungsträgerdynamik in dem magnetischen Perowskit* $La_{0,67}Ca_{0,33}MnO_3$ at the Physikalisches Institut, Johann Wolfgang Goethe-Universität, Frankfurt (Main); advisor: Prof. Dr. H. Roskos
December 2001	Diplom in physics
since April 2002	Ph. D. work in Prof. Dr. K. Baberschke's group
October 2002 to July 2003	Tutor of an exercise course for students of the 3^{rd} semester

Zusammenfassung

Im Rahmen dieser Arbeit wurden Röntgenabsorptionsspektroskopie (XAS) und magnetischer Röntgenzirkulardichroismus (XMCD) an ultradünnen, ferromagnetischen Fe-, Co- und Ni-Filmen und an Einkristallen der Seltenen Erd-Elemente Gd, Tb und Dy untersucht. Die experimentellen Ergebnisse wurden jeweils mit theoretischen Rechnungen verglichen.

Es ist bekannt, dass das Wachstum von $3d$-Ferromagneten mit Hilfe von Sauerstoff als Surfactant verbessert werden kann. Dazu wird zunächst Sauerstoff auf der gereinigten Substratoberfläche adsorbiert und erst danach der ferromagnetische (FM) Film aufgewachsen. In der vorliegenden Arbeit wurde dieser Effekt genutzt, um den Magnetismus ultradünner FM Filme zu beeinflussen. Fe-, Co- und Ni-Filme wurden mit und ohne Sauerstoff als Surfactant auf einkristallinen Cu-Substraten präpariert. Röntgenabsorptionsspektren im Nahkantenbereich (NEXAFS) erlauben Rückschlüsse auf die elektronische Struktur der untersuchten Filme. Die NEXAFS-Spektren zeigen eine für die jeweilige chemische Bindung charakteristische Linienform. Aus der Linienform von NEXAFS-Spektren der mit Sauerstoff-Surfactant gewachsenen Filme konnte geschlossen werden, dass keine volumenartigen Oxide mit dem jeweiligen Ferromagneten entstehen. Die Winkelabhängigkeit der NEXAFS-Spektren an der O-K-Kante zeigt hier, dass die Sauerstoff-Atome, die zuvor auf die saubere Cu-Oberfläche aufgebracht worden sind, während des Filmwachstums stets an der Oberfläche des Films bleiben. Am Beispiel von Ni wurde aus den NEXAFS-Spektren an den Ni-$L_{2,3}$-Kanten ein Ladungstransfer von $3d$-Zuständen des Ferromagneten zu den $2p$-Zuständen des Sauerstoffs bestimmt. Aufgrund der Elementspezifität des XMCD kann sowohl der Einfluss des Sauerstoffs auf den Magnetismus der ferromagnetischen Filme selbst als auch der induzierte Magnetismus am Sauerstoff untersucht werden. XMCD an der O-K-Kante weist den induzierten Magnetismus des Sauerstoffs nach. Da keine Spin-Bahn-Aufspaltung des $1s$ Anfangszustands vorliegt, ist die magnetische Information, die aus XMCD-Spektren an K-Kanten gewonnen werden kann, auf das Bahnmoment beschränkt. Deshalb wurden zusätzlich Rechnungen im Rahmen einer *ab initio* Theorie durchgeführt. Die berechneten Spektren stimmen sehr gut mit den experimentellen Beobachtungen überein. Darüber hinaus

liefern die Rechnungen neben der spin-aufgelösten Zustandsdichte, auch die Spin- und die Bahnmomente. Um zudem den Einfluss des Sauerstoffs auf die ferromagnetischen Schichten selbst im Detail zu untersuchen, wurden am Beispiel von Ni dickenabhängige Messungen durchgeführt. Ni-Filme verschiedener Dicken oberhalb des Spinreorientierungsübergangs, d. h. Filme mit einer leichten Magnetisierungsrichtung senkrecht zur Filmebene, wurden auf Cu(100) und Cu(110) präpariert. Die Gesamtmagnetisierung verhält sich auf den beiden Oberflächen unterschiedlich: Ni-Filme, die mit Sauerstoff als Surfactant auf Cu(100) aufgewachsen worden sind, zeigen für geringere Dicken eine Magnetisierung, deren Betrag unterhalb dessen von volumenartigem Ni liegt. Auf der offeneren Cu(110)-Oberfläche wird jedoch eine erhöhte Magnetisierung in den dünneren Filmen beobachtet. Dieser Unterschied im magnetischen Verhalten wird der unterschiedlichen Oberflächenrauigkeit zugeschrieben. Eine detaillierte Analyse mit Hilfe der integralen Summenregeln zeigt, dass die Erhöhung der Ni-Magnetisierung auf Cu(110) vornehmlich von einer Erhöhung des Bahnmoments herrührt. Auf der raueren Oberfläche ist aufgrund der reduzierten effektiven Koordination das Bahnmoment der Oberflächenatome weniger stark ausgelöscht.

Im zweiten Teil der Arbeit wurden Co/Cu/Ni-Dreifachlagen untersucht. Sie dienen als Prototypsystem für Vielfachschichten, in denen eine Interlagenaustauschkopplung J_{inter} auftritt. Diese koppelt die beiden ferromagnetischen (FM) Schichten aus Co und Ni über die nicht magnetische Cu-Zwischenschicht. Mittels XMCD wurden der Einfluss von J_{inter} und die Bedeutung der erhöhten Spinfluktuationen in zweidimensionalen Systemen untersucht. Für die beiden FM Schichten wurden unterschiedliche Elemente benutzt, um von der Elementspezifität der XMCD-Methode profitieren zu können. Diese ermöglicht es, das magnetische Verhalten der beiden FM Schichten individuell und unabhängig voneinander zu studieren. Die Interlagenaustauschkopplung bewirkt eine deutliche Veränderung der elementspezifischen, temperaturabhängigen Magnetisierungskurve $M(T)$ in der Dreifachlage gegenüber den Einzelfilmen. Bei der Untersuchung des Einflusses von J_{inter} auf $M(T)$ kommt der *in-situ*-Präparation und -Messung der Proben eine besondere Bedeutung zu. Zuerst wurde die Magnetisierung eines mit Cu bedeckten Ni-Films gemessen. Danach wurde die Interlagenaustauschkopplung zugeschaltet, indem der Co-Film auf die identische Cu/Ni/Cu(100)-Probe aufgewachsen wurde. Damit konnte sichergestellt werden, dass jede Veränderung der elementspezifischen Ni-Magnetisierung auf den Einfluss von J_{inter} zurückzuführen ist. Bei einer derartigen Vorgehensweise zeigt sich, dass die quasi-kritische Temperatur der Ni-Schicht $T^{*}_{\mathrm{C,Ni}}$ in der Dreifachlage um $\Delta T_{\mathrm{C,Ni}}$ über der Curie-Temperatur $T_{\mathrm{C,Ni}}$ des einfachen Ni-Films liegt. In der vorliegenden Arbeit wurde die Ni-Dicke auf bis zu ~ 2 Monolagen (ML) reduziert, was noch deutlich unterhalb der in früheren Arbeiten verwendeten Dicken ist. Bei diesen extrem dünnen Ni-Lagen ist die Temperaturverschiebung $\Delta T_{\mathrm{C,Ni}}/T_{\mathrm{C,Ni}}$ am deutlichsten ausgeprägt. Sie kann für $d_{\mathrm{Ni}} \approx 2$ ML über 200 % betragen. Solch eine enorme Verschiebung einer kritischen Temperatur ist in Volumenmaterialien undenkbar. Es ist seit einiger Zeit bekannt, dass eine theoretische Beschreibung dieses magnetischen Verhaltens ultradünner Filme nur gelingt, wenn Spin-Spin-Korrelationen (Spin-Fluktuationen) in der Theorie enthalten sind. Eine Beschreibung in einer statischen Molekularfeldnäherung ist daher unzureichend. Mit Hilfe eines theoretischen Modells, das die Spin-Fluktuationen berücksichtigt, ist es im Rahmen einer Kollaboration mit P. Jensen gelungen, für die Interpretation der Ergebnisse der vorliegenden Arbeit eine Relation zwischen $\Delta T_{\mathrm{C,Ni}}/T_{\mathrm{C,Ni}}$ und J_{inter} herzustellen. Im Unterschied zu früheren Resultaten in Molekularfeldnäherung zeigte sich, dass die beiden Größen $\Delta T_{\mathrm{C,Ni}}/T_{\mathrm{C,Ni}}$ und J_{inter} nicht linear voneinander abhängen. Damit wurde es erstmals möglich, die beiden Abhängigkeiten $\Delta T_{\mathrm{C,Ni}}/T_{\mathrm{C,Ni}}\,(d_{\mathrm{Ni}})$ und $J_{\mathrm{inter}}\,(d_{\mathrm{Cu}})$ zu kombinieren und gemeinsam zu betrachten. In der Vergangenheit wurden beide Abhängigkeiten unabhängig voneinander diskutiert. Als Ergebnis wird in dieser Arbeit eine dreidimensionale Grafik präsentiert, die die gewölbte Fläche als Resultat der Theorie und die experimentellen Ergebnisse enthält. Die theoretische Kurve ist in guter Übereinstimmung mit den experimentellen Beobachtungen.

Im Zusammenhang mit den Untersuchungen der Dreifachlagen wurden im Rahmen dieser Arbeit Messungen der Elektronenausbeute im angelegten Magnetfeld in der vorhandenen UHV-Apparatur etabliert. Dafür wurde ein wassergekühltes Spulensystem entwickelt und erfolgreich in Betrieb genommen. Mit dem neuen Spulensystem sind nun auch Messungen im statischen Magnetfeld H mit bis zu $\mu_0 H \approx 50$ mT möglich.

Im letzten Teil der Arbeit wurde die Schalenspezifität der XMCD-Methode genutzt, um das Zusammenwirken des Magnetismus der $5d$-Leitungselektronen und der lokalisierten $4f$-Zustände in den Selten-Erd-Elementen Gd, Tb und Dy zu studieren. In diesen Materialien wird der größte Anteil an der Magnetisierung von den stark lokalisierten $4f$-Momenten getragen. Die ferromagnetische Ordnung dieser $4f$-Momente untereinander wird durch die delokalisierten $5d$-Leitungselektronen vermittelt, die selbst ein induziertes magnetisches Moment tragen. Neben den Dipolübergängen (E1: $2p \rightarrow 5d$) tragen Quadrupolübergänge (E2: $2p \rightarrow 4f$) entscheidend zu dichroischen Signal an den $L_{2,3}$-Kanten dieser Elemente bei. Aufgrund der am Übergang beteiligten Anfangs- und Endzustände liefern XMCD-Messungen an den $L_{2,3}$-Kanten Informationen sowohl über die Beiträge der $5d$-Zustände als auch derjenigen der $4f$-

Zustände. Im Gegensatz zu vielen existierenden XMCD-Daten komplexer Verbindungen wurde die Systematik des XMCD Seltener Erden in der vorliegenden Arbeit an Einkristallen studiert. In den zahlreichen Verbindungen der Seltenen Erden treten zusätzliche komplexe Wechselwirkungen zwischen den verschiedenen beteiligten Elementen auf, die in den einelementigen Einkristallen nicht vorkommen. Für die Reihe Gd, Tb und Dy wurden die gemessenen temperaturabhängigen XMCD-Spektren gezeigt und diskutiert. Diese Spektren beinhalten eine Vielzahl von Feinstrukturen. Anders als bei den $3d$ Ferromagneten ändert sich die relative Intensität der verschiedenen spektroskopischen Beiträge und damit die Linienform der XMCD-Spektren in Abhängigkeit von der Temperatur. Die bei tiefen Temperaturen gemessenen Spektren wurden mit *ab initio* Rechnungen verglichen, die mittels des FEFF-Codes im Rahmen dieser Arbeit durchgeführt wurden. Damit können die Beiträge aus dipolaren und quadrupolaren Übergängen zum XMCD bei tiefen Temperaturen systematisch identifiziert und analysiert werden. Es bleibt jedoch eine Herausforderung für die Theorie, die Temperaturabhängigkeit der Spektren zu berechnen.

In dieser Arbeit wurde gezeigt, wie aus spin-gemittelten und spin-abhängigen Röntgenabsorptionsspektren die verschiedenen magnetischen Beiträge eines Systems identifiziert und getrennt werden können. Die experimentellen Daten decken sich mit Ergebnissen theoretischer Untersuchnungen. Man gelangt dadurch zu einem deutlich besseren Verständnis der magnetischen Eigenschaften der untersuchten Systeme.

Acknowledgment

Last but not least, I wish to allocate some space to say "Thank you" to everybody who contributed in her or his way to the success of my thesis.

First of all, I thank *Prof. Dr. Klaus Baberschke* for the initial phone call when he offered me a position in the babgroup. This opened me the opportunity to spend a fruitful PhD time. By his guidance he has made me learn how to work successfully on the edge of modern research in physics.

I also thank *Prof. William Brewer, PhD* for co-assessing this thesis, his steady interest in the progress of the work and his helpful suggestions for improvement.

In the "BESSY-crew", we struggled together to keep the chamber running. I say thank you for innumerable sputtering cycles, many thin films, discussions about physics and the rest of the life during endless days and nights not only at BESSY. *Dr. Andreas Scherz* introduced me to many secrets of UHV, beamlines, XAS, XMCD, and avoiding water fountains in the experimental hall. He reminded us all of not to forget the coffee. I am grateful to *PD Dr. Heiko Wende* for sharing his experience, for explaining basic physics and discussing the latest results, for accomplishing lots of administrative work, and finally for organizing money to pay new equipment and my position. *Matthias Bernien* contributed to the trilayer business during his diploma studies also by his complex questions even at 5 a.m. after a long night shift. Thanks to his skills to handle all the integrals and to correctly feed Mathematica we successfully optimized the design of the new coil system. *Dr. N. Ponpandian* exercised a lot of patience and finally made the shrink tube do what it was supposed to do: shrinking.

Dr. Kilian Lenz knows useful answers to so many questions. He handled the painful job of system administration and user support. Thank you for disinfecting the BESSY-PC when it returned "sick" from Adlershof. *Ela Kosubek* as the "good soul" provided many small technical tricks of all kinds – too many to mention them here. *Dr. Panos Poulopoulos* contributed to the measurements at the ESRF. I thank everyone in the (ex-)babgroup and the new "kuchgroup", *Dr. Jürgen Lindner*, *Dr.*

Christoph Rüdt, *Dr. Ramona Nünthel*, *Dr. Tomasz Toliński*, *Radu Abrudan*, *Dr. Keiki Fukumoto*, and *Prof. Dr. Wolfgang Kuch* for challenging questions, a helping hand or two, and contributing to the pleasant working atmosphere.

I acknowledge *Dr. Peter Jensen*, *Prof. Dr. Ruqian Wu*, and *Dr. Alex Ankudinov* for their collaboration and contributions from the theoretical point of view.

Successful beamtimes are only possible with the valuable help by the beamline scientists and technical staff at the synchrotron facilities. I wish to mention in particular *Birgitt Zada*, *Dr. Friedmar Senf*, and *Helmut Pfau* from BESSY and the ID12 Team at the ESRF *Dr. Fabrice Wilhelm*, *Dr. Andrej Rogalev*, and *Dr. Nicolas Jaouen*.

Also the work by the "shipping company" *Herr Böttcher*, *Herr Christiansen*, and *Herr Aufrecht* was of great value, because the local public transportation company does not accept UHV chambers for luggage.

Herr Müller and his team in the mechanical workshop always made a good job.

Uwe Lipowski as the current technician of the group helped as well as his predecessor *Wolfgang Wisny* who, although retired and very busy, was always willing to set the pulse-electronics back into proper operation.

Dr. Jonathan Hunter-Dunn explained and discussed the coil system installed in the XMCD chamber at MAXlab. His ideas helped tremendously in designing the new water-cooled coil system for our chamber. At this point I should not forget to add my thankfulness to the strong men of the babgroup for mounting and unmounting the heavyweight before it finally had proven its UHV compliance.

The German Federal Ministry of Education and Research (Bundesministerium für Bildung und Forschung) financially supported this work (05 KS1 KEB/4 and 05 KS4 KEB/5).

Finally, I am very happy to have people outside the world of physics to add here: my parents *Annerose* and *Theo* who always have a tea ready when I return home, my "little" brother *Jens* who knows best how to pack vans, my friend *Sabine* who stays up late at night for phone calls even if she has a meeting early next morning, and *Torben* who made me follow him to Berlin, encourages me to see the dark side of life less dark and turns the bright side of life even brighter.

Thank you all!

Index